UNIVERSITÀ
DEGLI STUDI
FIRENZE

Università degli Studi di Firenze

Dipartimento di Ingegneria dell'Informazione (DINFO)

Corso di Dottorato in Ingegneria dell'Informazione

Curriculum: Automatica, Ottimizzazione e Sistemi Complessi

Settore Scientifico Disciplinare: ING-INF/04

Model-based estimation techniques for oil and gas rotating equipment

Candidate

Matteo Galanti

Supervisors

Prof. Michele Basso

Dr. Lorenzo Giovanardi

Prof. Giacomo Innocenti

PhD Coordinator

Prof. Luigi Chisci

ciclo XXXI, 2015-2018

Università degli Studi di Firenze, Dipartimento di Ingegneria dell'Informazione (DINFO).

PhD thesis evaluators

Prof. Emrah Biyik, *Yaşar University (Izmir, TR)*

Prof. Mauro Venturini, *Università di Ferrara (Ferrara, IT)*

Ma io sono fiero del mio sognare,
di questo eterno mio incespicare
e rido in faccia a quello che cerchi e che mai avrai!
(Quattro stracci, Francesco Guccini)

How long is forever?
Sometimes, just one second.
(Alice and White Rabbit, Alice in Wonderland)

Acknowledgements

Coming towards the end of such a challenging and satisfying journey, I feel that there are a lot of people that really helped me to get here.

First of all, I would like to acknowledge the efforts and inputs of my supervisors Prof. Michele Basso, Dr. Lorenzo Giovanardi and Prof. Giacomo Innocenti who were of great help during my research. Furthermore, my acknowledgement goes to all the Academic figures which, with different roles, allowed me to successfully conclude my PhD.

I would like to thank for their kind support and hospitality Dr. Gianni Bagni, Dr. Luca Pretini and all the other people from "Nuovo Pignone - Baker Hughes, a GE Company" I worked with during my PhD. I will not name all of you, with the goal of really thank everyone, since you made me feel part of a great team.

A very thankful acknowledgement is deserved to my research colleagues Luca Alessandrini and Davide Piro, who collaborated on many parts of my research work. I am grateful to them for being with me during this period, it has been a pleasure to share with them this adventure.

Finally, the last but most appreciated thank goes to my family that, I am sure, will be proud of me.

Abstract

Model-based techniques can often help to unlock the full potential of a dynamical system in terms of performance, robustness and effectiveness. This dissertation, developed in collaboration with *Nuovo Pignone - Baker Hughes, a GE Company*, focuses in particular on turbomachinery equipment for oil and gas applications. The main purpose is to show the benefits that specific model-based techniques can bring to the current system without modifying the existing plant. The methods introduced in this thesis do not suggest any physical change on installed system, indeed they are aimed to improve some operative aspect by exploiting the already available equipment.

As a matter of fact, the detailed knowledge of mathematical models allows both the estimation of quantities that can not be directly measured and the prediction of the future behaviour of the system. Moreover, the increasing computational capability of modern CPUs makes these techniques even more interesting, allowing a potential real time implementation without an excessive computational burden. In practice, this thesis work addresses the issue of improving the reliability, the performance and the effectiveness of the control systems of some specific oil and gas applications by studying and exploiting the physical laws on which the system is based on.

In particular, this work focuses on specific rotating equipment, i.e. centrifugal compressors, gas turbines and turbo-generators, which consist of an electric generator driven by a gas/steam turbine. Usually the power required to drive a centrifugal compressor is not directly measured; therefore, three power estimation methods based on the thermodynamic and mechan-

ical knowledge of the system and the least squares theory are proposed and compared between each other. Then, after a deep analysis of a typical electric generation plant composed of several turbo-generators, a control logic to prevent the system from experiencing torsional instability is proposed. Finally, an accurate mathematical model of a particular gas turbine based on Kalman filter theory is proposed as well as a comprehensive discussion about the main fundamental modelling features introduced to cover all the aspects of interest.

Contents

Nomenclature

List of acronyms

AC	Axial Compressor
AFR	Air-to-Fuel Ratio
AWGN	Additive White Gaussian Noise
CC	Centrifugal Compressor
CP	Corrective Parameter
CPU	Central Processing Unit
DC	Direct Component
DLE	Dry Low Emission
EG	Electric Generator
EKF	Extended Kalman Filter
FF	Forgetting Factor
HPT	High Pressure Turbine
HVDC	High Voltage Direct Current
G	Generator
GG	Gas Generator
GT	Gas Turbine

IGV	Inlet Guide Vane
KF	Kalman Filter
LCI	Load Commutated Inverter
LNG	Liquefied Natural Gas
LS	Least Squares
LHV	Lower Heating Value
LPT	Low Pressure Turbine
MPC	Model Predictive Control
MSE	Mean Square Error
NASA	National Aeronautics and Space Administration
NPSS	Numerical Propulsion System Simulation
PF	Power Factor
PID	Proportional-Integral-Derivative
ppm	Parts Per Million
pu	Per Unit
RLS	Recursive Least Squares
RMS	Root Mean Square
SAC	Single Annular Chamber
SSTI	Sub-Synchronous Torsional Interaction
TG	Turbo-Generator
THD	Total Harmonic Distortion
TNF	Torsional Natural Frequency
WAR	Water-to-Air Ratio
VFD	Variable Frequency Drive
VSV	Variable Stator Vanes

List of symbols

Latin symbol	Unit	Description
a	$[m \cdot s^{-1}]$	Sound speed
c_p	$[J \cdot (kg \cdot K)^{-1}]$	Isobaric heat capacity
c_v	$[J \cdot (kg \cdot K)^{-1}]$	Isochor heat capacity
Δh	$[J \cdot kg^{-1}]$	Specific head
$\dot{m}$	$[kg \cdot s^{-1}]$	Mass flow
M	$[m \cdot s^{-1}]$	Mach number
M_w	$[kg \cdot mol^{-1}]$	Molar mass
n	[ ]	Polytropic exponent
p	$[kPa]$	Pressure
Q	$[m^3 \cdot s^{-1}]$	Volumetric flow
R	$[J \cdot (K \cdot mol)^{-1}]$	Gas constant
T	$[K]$	Temperature
v	$[m^3 \cdot kg^{-1}]$	Specific volume
Z	[ ]	Gas compressibility

Greek symbol	Unit	Description
α	$[rad \cdot s^{-2}]$	Angular acceleration
γ	[ ]	Isobaric/Isochor heat capacity ratio
η	[ ]	Efficiency
ρ	$[kg \cdot m^{-3}]$	Density
ω	$[rad \cdot s^{-1}]$	Angular speed

Introduction

In the last centuries the strong economic growth has boosted the rise of the global energy demand, and oil and gas industry has met most of this increase. As is always the case, human needs have driven the technological progress and many applications have been developed to meet these needs and increase global wellness. As a matter of fact, power and energy industry have always played a key role in scientific and technological development.

Oil and gas industry includes processes of exploration, extraction, refining, transporting through pipelines and marketing of oil and gas products. Over many decades the scientific and industrial research has been focused on the development of typical turbomachinery equipments such as gas and steam turbines, compressors and auxiliary systems. This dissertation will concentrate on *Gas Turbines* (GTs), *Electric Generators* (EGs) and *Centrifugal Compressors* (CCs).

Gas turbines are a particular type of prime mover introduced at the beginning of twentieth century, and their popularity is mainly due to their reliability and availability, to the capacity of fulfilling rapid peak load demand, and to their low operating and maintenance costs. To say it briefly, flexibility and the capability of meeting several practical needs are the features that make GTs so appreciated in many technical fields. Gas turbines engines are widely used all over the world for aircraft propulsion, electricity generation and many other industrial applications, indeed they can be used as mechanical drivers both for pumps and compressors ([24], [87], [16],[61] and [73]).

Generally speaking, compressors are fluid-flow dynamic machines for the compression of gases; centrifugal compressors are rotating machines characterised by a flow with radial direction. CCs are heavily employed in many industrial applications, in particular in oil and gas field they are used for pipeline, gas lift and gas liquefaction applications.

Electric generators are rotating machines that convert mechanical energy into electric energy: from a theoretical point of view they are analogous to electric synchronous motors, indeed they are based on the same operating principles.

CCs and EGs are driven machines, i.e. they need an external source of energy to operate: usually the prime mover is a gas turbine. Gas turbine and driven machine are generally coupled directly or by means of a gear unit, depending on the application. This work is aimed to the study of mathematical models for these rotating equipments, i.e. gas turbines, centrifugal compressor and electric generators; in particular, the main purposes are the development of a mathematical model for a specific GT and the analysis of CCs or EGs driven by GTs.

For many years these items have been enhanced from a physical point of view, thanks to a constant development concerning materials, manufacturing procedures, mechanical and aerodynamical efficiency and more effective control systems based on improved sensors and actuators. Nowadays it is clear that the real challenge is to improve the performance of the whole system without introducing deep modifications to physical equipment. Plant designers have to face multiple and sometimes conflicting objectives, e.g. global optimisation of the system, maximisation of each component lifespan and reduction of harmful emissions such as NO_x.

Model-based techniques, i.e. methods based on mathematical models of the specific system under analysis, can provide a great help to achieve these particular goals, indeed they are able to overcome system lacks or limitations without introducing expensive or overkill solutions. These models turn out to be very useful in many practical issues, such as fault detection, prediction of system response to certain inputs and validation of different

control logics. Besides that, many quantities (e.g. the firing temperature of a GT or the power request of a CC) are not directly measured by usually installed commercial sensors; specific models can be used as soft sensors to estimate these quantities and provide virtual measurements. Therefore, these models can enhance the awareness about the whole plant and they can be exploited to design a more effective control system or to predict the future behaviour of the system.

As mentioned before, the main purpose of this dissertation developed in collaboration with *Nuovo Pignone - Baker Hughes, a GE Company*, is to show the benefits that specific model-based techniques can bring to the current system without modifying the existing plant. The methods introduced in this thesis do not suggest any physical change on installed systems, indeed they are aimed to improve some operative aspects by exploiting the already available equipment.

Finally, it is worth noticing that these model-based techniques become even more interesting considering the increasing computational capability of modern CPUs that allows a potential real time implementation without an excessive computational burden.

Thesis outline and contributions

Specifically, the following macro-themes will be addressed in detail within the thesis:

1. **Chapter 1: Centrifugal Compressor Modelling and Robust Power Estimation**
   In this chapter the attention is focused on centrifugal compressors and in particular we will address the issue of estimating the power request of a CC. Usually CCs are driven by synchronous electric motors or GTs. In the former case a realistic model of the motor and accurate electric measurements are available, thus it is trivial to figure out the power absorbed by the CC. In the latter case on the contrary it is very

complex to measure or estimate the GT delivered power, therefore the idea is to exploit other CC available measurements and models to estimate the power requested to drive the compressor.

In the first part some guidelines about centrifugal compressors technology are provided. Then, three different power estimation methods based on CC models are introduced and compared with each other. Finally, two techniques that rely on the least squares theory to enhance the robustness with respect to measurements unavailability are proposed and analysed.

Contributions:

The main contribution of this chapter is the application of well-known theories and techniques to a specific problem, i.e. the estimation of the CC power request. In turn, the innovative aspects are related to the comparison between different methods based on real field data and to the introduction of techniques aimed to improve the robustness of each method. In that sense, the thesis enhances the current state of the art.

2. **Chapter 2: Sub-Synchronous Torsional Interactions in Electrical Networks**

   In this chapter the typical configuration of an isolated electric grid fed by turbo-generators (TGs) is analysed. Typical TGs usually consist of an electric generator driven by a turbine, and they are massively employed in many power generation plants worldwide.

   In particular this chapter deals with an unstable coupling phenomenon between the mechanical and the electric parts which is usually referred to as SSTI (*Sub-Synchronous Torsional Interaction*). SSTI can lead to very critical situations in which the mechanical train composed of a GT coupled with an EG can experience self-sustained or even increasing torsional oscillations.

   SSTI vibrations can cause mechanical damage and they heavily affect the operability of the system, indeed when dedicated vibration sensors

(e.g. seismic sensors) detect too large mechanical oscillations the system is automatically shut down in order to protect itself and preserve the surrounding workers' safety.

In the first part of this chapter the physical causes of this phenomenon are explored in depth and mathematical models of the mechanical and electrical part are introduced. Then, an electric damping system aimed to attenuate torsional oscillations is proposed and some simulations results are examined.
Contributions:
The first contribution of this chapter is the analysis of the main causes that may trigger SSTI phenomenon in an isolated electrical grid. Then, it introduces and it validates through several simulations an effective damping system that is aimed to reduce the torsional oscillations of the turbo-generator system.

3. **Chapter 3: Gas Turbine Modelling and Model-Based Estimation**
   Many different types of GTs have been developed in the past years and they can be broadly classified as single-shaft GT, mainly employed for generator drive application, or two-shaft GT, mainly employed for mechanical drive application. In this chapter the characterization and the modelling of a particular two-shaft GT will be addressed: the GT under analysis is the GE LM2500+G4 DLE, an aero-derivative twin-shaft GT produced by General Electric.

   In particular, an iterative double-step method is proposed for the modelling of gas generator (GG, that is high power turbine, or main shaft) in this aero-derivative GT. The first step is based on a combination of generalised maps describing the nominal GT behaviour and thermodynamic laws that allow an a-priori estimation of flows, temperatures and pressures of each GG section. The second step is based on a Kalman Filter (KF) that corrects these a priori estimations exploiting all available measurements.

The model has been trained and validated on a massive dataset created through a full high-fidelity modelling tool based on NPSS (*Numerical Propulsion System Simulation*), which contains the turbine geometrical and mechanical data. Finally, the quality of the model has been evaluated also by exploiting field data and conclusions have been drawn.
Contributions:
The main contribution of this chapter is the introduction of a novel iterative double-step method to estimate the main quantities of a specific gas turbine. This innovative modelling approach is likely to have a strong impact both in industrial and research field, indeed it represents a suitable solution to improve equipment performance avoiding expensive hardware enhancement.

For the sake of clarity, the notations and the symbols used in each chapter are introduced before being adopted. However, the lists of acronyms and most used symbols is reported at the beginning of the thesis.

Chapter 1

Centrifugal Compressor Modelling and Robust Power Estimation

After a brief description of centrifugal compressor technology, the first part of this chapter introduces some mathematical models to estimate the power request of these fluid-flow machines. In the second part some methods to increase the robustness of such models are presented.

1.1 General description

Compressors are heavily used in a wide variety of industrial processes. Fluid-flow machines are usually categorised in axial and radial designs by means of the main direction of flow; the mass flow is basically axial in axial machines and basically radial in centrifugal machines, with the flow from the inside to the outward direction. Axial compressors (ACs) are usually preferred in high power gas turbine applications, indeed they can achieve higher mass flow rate, even if the high pressure rise is achieved using a large number of stages. On the other hand centrifugal compressor (CC) has wider operating margins and generates a higher pressure ratio per stage, but they are not suitable for high flow rate applications. Nevertheless, centrifugal and axial

compressors have the same operating principle, so it is worth to refer to the more general class of turbocompressors that covers all continuous flow compressors. Figure 1.1 shows a typical AC (1.1a) and a CC casing (1.1b), which is needed to contain the rotor and the impellers of the CC.

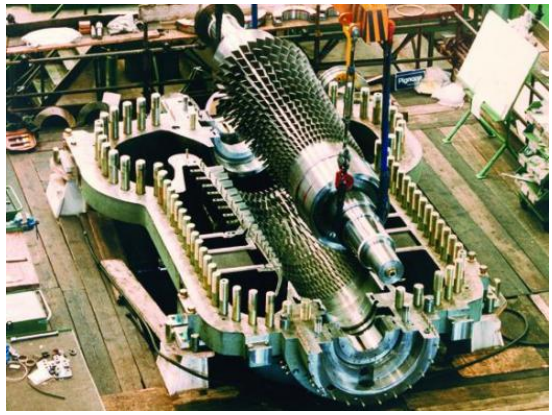

(a) *Axial compressor*

(b) *Centrifugal compressor casing*

Figure 1.1: Example of axial compressor (a) and centrifugal compressor casing (b). Courtesy of BHGE, source `www.bhge.com`

Centrifugal compressors are fluid-flow dynamic machines for the compression of gases. A schematic sketch of a centrifugal compressor is shown

in figure 1.2.

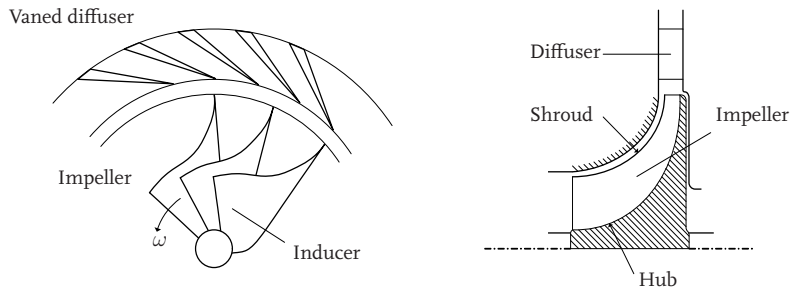

Figure 1.2: Centrifugal compressor with vaned diffuser.

It essentially consists of a stationary casing containing a rotating impeller which imparts a high velocity to the air, and a number of fixed diverging passages in which the air is decelerated with a consequent rise in static pressure. The bladed impeller, with its continuous fluid flow, transfers the mechanical shaft energy into enthalpy, i.e. gas energy. Thus, pressure, temperature and velocity of the gas leaving the impeller are higher than at the impeller inlet. The annular diffuser downstream of the impeller delays the gas velocity, thus it provides a further pressure and temperature increase. In practice, centrifugal compressors convert the kinetic energy into pressure. This energy conversion can be explained by the Bernoulli equation that states that the sum of kinetic energy, potential energy and pressure head is constant. Note that the momentum transfer from the impeller blades to the fluid can be described by using so-called velocity triangles (figure 1.3)

Centrifugal and axial flow compressors are very complex and they are characterised by high non-linearities; moreover, they are subject to two distinct aerodynamic instabilities, rotating stall and surge, which can severely limit the compressor performance. Surge is an unstable operating mode of a compression system that occurs at low mass flows. It is a dynamic instability that develops into a limit cycle[1] that finally results in large amplitude

[1] A limit cycle is a closed and periodic orbit in phase space [89].

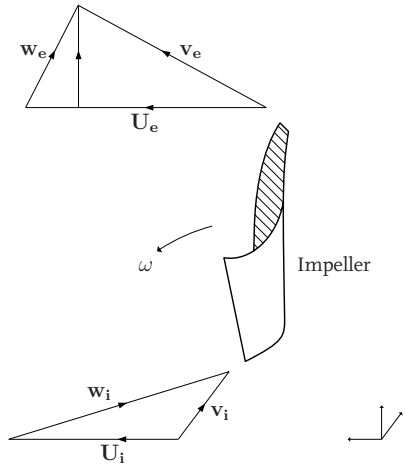

Figure 1.3: Impeller inlet and discharge velocity triangles.

fluctuations of pressure and flow rate. Surge not only limits compressor performance and efficiency but it can also damage the compressor. Furthermore, the vibrations associated with surge can result in unacceptable noise levels (for more details see [61], [24], [36] and [43]). During the past years many antisurge systems have been proposed, see e.g. [6], [68], [38], [78], [103] and [94].

Rotating stall is characterised by a distortion of the compressor flow that occurs in specific regions usually called *stall-cells*. In these regions the flow is highly reduced and sometimes completely blocked; obviously this instability leads to a very large drop in performance and efficiency, and it results in a very high mechanical stress for the machine. An other typical operating region of compressor is choking, that is the condition which occurs when a compressor operates at very high mass flow rate and flow through the compressor can not be further increased. In this condition Mach number at some part of the compressor reaches the unity, i.e. gas speed has reached the sonic velocity. A typical performance map of a turbocompressor is depicted in figure 1.4, which features several lines at constant speed that represent

steady-state operating points at the same speed and two critical lines, surge line (low flow rate) and choke line (high flow rate). These two curves are obtained by joining respectively the surge and choke points at different constant speeds, and the operating point is supposed to stay within the region delimited by these curves.

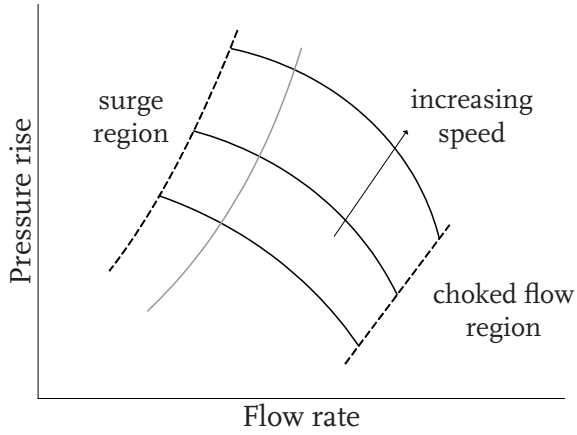

Figure 1.4: Typical turbocompressor performance map (black lines) and a realistic load characteristic (grey line).

In order to quantify the distance between the current operating point and the surge/choke line, the following margins M^{surge} and M^{choke} can be introduced

$$M^{surge} = 100\,\frac{\dot{m}_0 - \dot{m}_s}{\dot{m}_0};$$

$$M^{choke} = 100\,\frac{\dot{m}_0 - \dot{m}_c}{\dot{m}_0}.$$

Where $\dot{m}_0$ is the actual mass flow, $\dot{m}_s$ is the mass flow rate at surge line at the same constant speed and $\dot{m}_c$ is the mass flow rate at choke line at the same constant speed. In practice, M^{surge} and M^{choke} represent the percentage horizontal distances between the current operating point and the surge/choke line.

The most famous model for approximating dynamics of deviations of flow and pressure variables in a compressor from their nominal steady-state values is the *Moore-Greitzer* model ([66], [67] and [84]): many different approaches have been proposed in order to estimate the parameters on which this method is based on ([70], [96]). Furthermore, many variations of *Moore-Greitzer* model have been introduced to adapt this model to the requirements of particular applications ([28] and [97]). In addition, other kind of compressor models and parameters identification have been addressed in the past years, as shown in [105] and [71].

1.2 Mathematical model for power estimation

As shown in [21], an accurate model is important to design and optimise the control of centrifugal compressors. A typical turbo-compression train may consist of a gas turbine (GT), which incorporates an axial compressor used to provide high-pressure and high-density air to subsequent combustion and expansion stages, coupled to a centrifugal compressor used to perform mechanical work on a process gas to be compressed. This process gas has not to be confused with the gas fueling the GT, indeed they are different and separated gases and they never mix each other.

The work presented in this section aims to provide a reliable algorithm to estimate the power absorbed by a CC driven by a GT. This algorithm would provide an alternative way to estimate the GT power which is not based on a GT model that exploits the measurements provided by the sensors all over the GT (for instance pressure, temperature and speed transducers).

The main idea is that the power of the gas turbine is equal to the sum of the power absorbed by the driven system and the power losses. When the GT drives an electric generator the power can be easily estimated, indeed the voltage and current measurements on the electric generator allow an extremely accurate estimation of the electric power and the losses are negligible. When the GT drives a mechanical system as a centrifugal compressor the same idea can be exploited; thus, an alternative estimation of the

GT power can be achieved considering the measurements on the centrifugal compressor. However, for the time being the accuracy of sensors installed on centrifugal compressor is not comparable to the one achievable in the generator-drive case, which can also rely on a very realistic mathematical model.

First of all it is necessary to introduce an high level mathematical description of the compressor, possibly irrespective of the compressor under consideration: thus the modelling approach has to be based on a generic centrifugal compressor structure, as the one showed in figure 1.5. Note that the subscripts "s" and "d" simply state that the quantity refers respectively to compressor suction (inlet) or discharge (outlet).

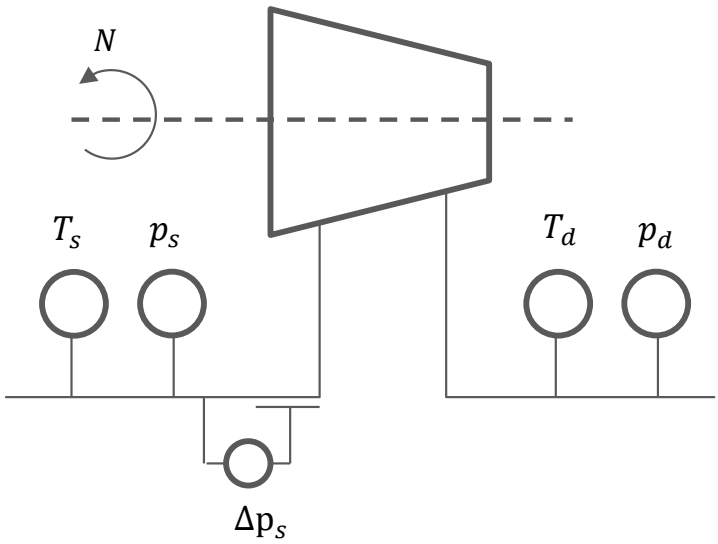

Figure 1.5: Centrifugal compressor schematic.

Table 1.1 summarises the characteristic quantities needed to describe the compressor and the nomenclature that will be used hereafter to refer to them.

Symbol	Unit	Definition
D	$[m]$	Impeller diameter
h_p	$[J \cdot kg^{-1}]$	Polytropic specific head
η_p	[ ]	Polytropic efficiency
Δh	$[J \cdot kg^{-1}]$	Compressor specific head
N	$[rpm]$	Compressor speed
u	$[m \cdot s^{-1}]$	Impeller tip speed
Z	[ ]	Gas compressibility
p	$[kPa]$	Gas pressure
T	$[K]$	Gas temperature
M_w	$[kg \cdot mol^{-1}]$	Molar mass
R	$[J \cdot (K \cdot mol)^{-1}]$	Gas constant
ρ	$[kg \cdot m^{-3}]$	Gas density
$\dot{m}$	$[kg \cdot s^{-1}]$	Mass flow
n	[ ]	Polytropic exponent
k_v	[ ]	Isentropic volume exponent
k_{FE}	[ ]	Flow coefficient
a	$[m \cdot s^{-1}]$	Sound speed
Q	$[m^3 \cdot s^{-1}]$	Volumetric flow
v	$[m^3 \cdot kg^{-1}]$	Specific volume

Table 1.1: Centrifugal compressor quantities nomenclature

The schematic shown in figure 1.5 is based on the measurements provided by six sensors:

1. T_s and T_d are respectively the suction and the discharge temperature

of the compressor;

2. p_s and p_d are respectively the suction and the discharge pressure of the compressor;

3. N is the compressor shaft speed, typically measured by one or more toothed wheels;

4. Δp is the differential pressure across a calibrated orifice (more information about this kind of flowmeters can be retrieved from [83] and [60]). It can be taken at suction or at discharge and thanks to equation 1.1 it allows the evaluation of the mass flow $\dot{m}$ throughout the compressor.

$$\dot{m} = k_{FE} \cdot \sqrt{\Delta p \cdot \rho}. \tag{1.1}$$

Where ρ is the density of the gas and k_{FE} is the coefficient of the flow element. The density ρ is equal to

$$\rho = \frac{M_w \cdot p}{Z \cdot R \cdot T}. \tag{1.2}$$

Actually, the measurements listed above are necessary but not sufficient to estimate the CC power: in addition gas composition has to be known and it is assumed to be constant during the operation. Once that gas composition is known and the measurements previously described are available, three methods can be introduced to estimate the power requested by the compressor, and they will be described in detail in the next paragraphs.

A - Method based on property libraries that allow the calculation of thermodynamic properties of the mixture;

B - method based on the non-dimensional curves that describe the performance of the compressor and a gas properties calculator;

C - method based on the polytropic efficiency of the compression and a gas properties calculator.

Note that methods [A], [B] and [C] are different approaches that allow the calculation of the specific gas enthalpy variation between suction and discharge (Δh). Once that Δh is known, they all use equation 1.3 to compute the ideal CC power.

$$P_{CC} = \dot{m} \cdot \Delta h + P^{loss}. \tag{1.3}$$

Where P^{loss} is needed to consider the mechanical losses of the system. Usually P^{loss} is set equal to a constant value or equal to a simple function of the rotating speed N, for instance

$$P^{loss} = f(N) = k_{loss} \cdot \left(\frac{N}{N_{nominal}} \right)^2.$$

In this work P^{loss} will be set equal to an average value $\bar{P}^{loss}$ computed during the design phase.

Moreover, all these methods are based on the assumption that the composition of the processed gas is known (e.g. it is measured by a gas chromatograph) and not variable during the operation.

1.2.1 Method [A]: calculation of thermodynamic properties of mixture

Thanks to the mentioned libraries, it is possible to find out all the main properties of the gas, both at suction and discharge of the compressor. Starting from the knowledge of the gas composition, the library exploits all the measurements provided by the six sensors described above and it implements the real-gas equations of state in order to calculate the gas enthalpy increase. In the past many different equations have been proposed in order to figure out the real-gas behaviour, the library provides the possibility of choosing the equations to be solved, even if the BWRS equations (*Benedict-Webb-Rubin-Starling*, introduced in 1973) are the most used. BWRS equations and other empirical approaches to describe real gas thermodynamics are described in appendix A. Thermodynamic equations allow the evaluation of all the thermodynamic properties of the gas both at suction and discharge, thus it is

possible to evaluate the specific gas enthalpy increase between suction and discharge (specific compressor head)

$$\Delta h = h_d - h_s. \tag{1.4}$$

Beyond the accuracy of this method with respect to real power (this topic will be discussed in section 1.2.4), it is necessary to analyse some statistical features of this method. Considering that this method takes as inputs some measurements provided by real sensors, it is necessary to take into account the fact that these measurements are not ideal. This is the reason why it is necessary to test the sensitivity of every estimation method with respect to its own inputs. This sensitivity test quantifies the robustness of the estimation method with respect to the inputs variability. The real measurements can be statistically described by a Gaussian distribution with mean value μ equal to the value provided by the sensor and standard deviation σ connected with the sensor precision (retrievable from specific sensors datasheets). The 95% confidence interval of this measurement is equal to $\mu \pm 2\sigma$, while the 99% confidence interval will be equal to $\mu \pm 3\sigma$. Detailed description about Gaussian distribution can be found in [92]. The sensitivity test can be performed adding a noise-vector (in this work 1000 elements) with proper statistical features to every single input. After that the estimation method has to be applied to each single case and the results can be compared with the ideal estimation relative to zero-noise case. The *Additive White Gaussian Noises* (AWGN) relative to each input have been defined as follows.

- To define the mean value of each measurements a real trend has been taken into consideration;
- concerning pressure sensors, the standard deviation is set equal to $\sigma =$ 0.125% of the measurement range (95% confidence interval, i.e. $[\mu - 2\sigma; \mu + 2\sigma]$, corresponds to 0.25% of the measurement range);
- flow-meters are based on the measurements of pressure across an orifice. Their standard deviation is set equal to 0.5% of the measurement

range (95% confidence interval, i.e. $[\mu-2\sigma;\mu+2\sigma]$, corresponds to 1% of the measurement range);

- thermocouples datasheets usually provide a rectangular distribution to statistically describe the measurements. If the rectangular distribution has amplitude $2B$ it is possible to prove that the standard deviation of the correspondent Gaussian distribution is $\sigma = \frac{B}{\sqrt{3}}$.

Figure 1.6 shows an histogram of the percentage difference between noised inputs power estimation based on method [A] and the CC power computed with no-noise inputs.

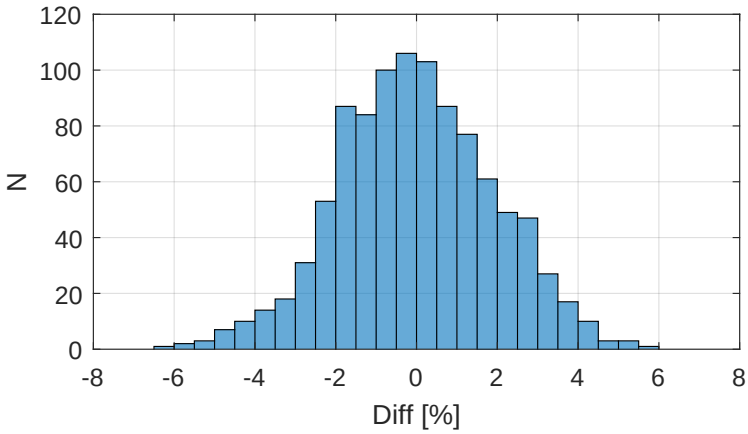

Figure 1.6: Deviation with respect to case without noise using method [A] ($\mu = -0.02\%$, $\sigma = 1.92\%$).

1.2.2 Method [B]: non-dimensional curves

As described in [61] and [24], the behaviour of a centrifugal compressor can be characterised using non-dimensional quantities φ and τ, i.e. adimensional

variables defined as follows

$$\tau = \frac{\Delta h}{u^2}; \tag{1.5}$$

$$\varphi = \frac{4Q_s}{\pi D^2 u} = \frac{4k_{FE}\sqrt{\frac{\Delta p}{\rho}}}{\pi D^2 u}. \tag{1.6}$$

Where Q_s is the volumetric flow at suction defined as

$$Q_s = \frac{\dot{m}}{\rho} = \frac{k_{FE}\sqrt{\Delta p \cdot \rho}}{\rho} = k_{FE}\sqrt{\frac{\Delta p}{\rho}}.$$

The impeller tip speed u can be computed starting from the rotating speed N and the impeller diameter D as

$$u = \frac{\pi N D}{60}.$$

These are experimental maps that describe the operating points where the compressor is able to work, and they are defined at first during the design phase (*Expected maps*) and then they are corrected to match the particular behaviour of each single machine with proper tests (*As-Tested maps*). Each map is defined as a family of curves obtained with different value of Mach number M, defined as the ratio between the impeller tip speed u and the sound speed in that thermodynamic conditions a

$$M = \frac{u}{a} = \frac{u}{\sqrt{\frac{k_v Z R T}{M_w}}}. \tag{1.7}$$

Figure 1.7 shows an example of non-dimensional map: note that usually these representations include a map relative to τ and a map relative to the polytropic efficiency η_P, even if in this method [B] only the τ map is required.

Equation (1.7) relies on the knowledge of some gas properties, such as gas compressibility Z (real gas behaviour is described by the equation $pvM_w = ZRT$, see appendix A), isentropic volume exponent k_v and molecular weight M_w. This means that such method needs a suitable algorithm for the definition of these quantities (e.g. the libraries introduced with method

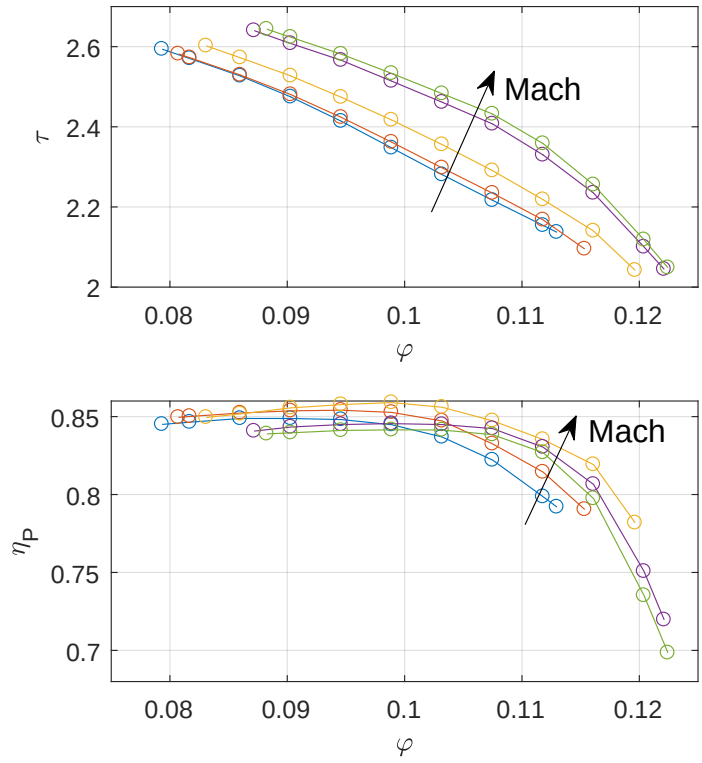

Figure 1.7: Example of non-dimensional map of a centrifugal compressor.

[A] can be partially exploited to find out only these properties). Thus, through direct measurements and some calculations it is possible to compute the flow coefficient φ and the Mach number M, then the value of τ can be extrapolated from non-dimensional map ($\tau = Map(\varphi, M)$) and Δh can be computed by reversing equation (1.5).

As done in paragraph 1.2.1, figure 1.8 shows the percentage deviation in CC power calculation introduced by the same additive white Gaussian noises on each measurement.

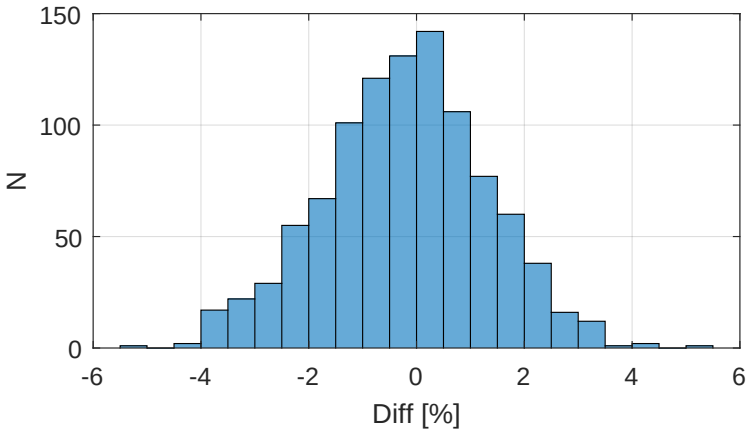

Figure 1.8: Deviation with respect to case without noise using method [B] ($\mu = -0.23\%$, $\sigma = 1.51\%$).

1.2.3 Method [C]: compressor polytropic efficiency

This method is based on the polytropic efficiency of the centrifugal compressor $\eta_P \in (0; 1)$, defined as the ratio between the ideal polytropic specific head Δh_P required to compress the gas and the real one Δh

$$\eta_P = \frac{\Delta h_P}{\Delta h}. \tag{1.8}$$

It is possible to demonstrate[2] that the polytropic head is equal to

$$\Delta h_P = \frac{Z_s \cdot R \cdot T_s}{M_w} \cdot \frac{\left(\frac{p_d}{p_s}\right)^{\sigma} - 1}{\sigma}. \tag{1.9}$$

Method [C] follows these steps to compute Δh:

i. A gas properties calculator (e.g. the one described in paragraph 1.2.1) provides the value of X, Y and k_v, both at suction and discharge (respectively subscript "s" and "d")

$$X = \left(\frac{\partial Z}{\partial T}\right)_p \frac{T}{Z},$$

$$Y = 1 - \frac{p}{Z}\left(\frac{\partial Z}{\partial p}\right)_T,$$

$$k_v = isentropic\, volume\, exponent;$$

ii. polytropic efficiency η_P can be retrieved by interpolation of the η_P non-dimensional curves (similar to the map represented in figure 1.7)

$$\eta_P = Map(\varphi, M);$$

iii. the coefficient σ has to be computed both at suction and discharge, thanks to the relationship

$$\sigma = \frac{n-1}{n} = \frac{k_v - 1}{k_v} \cdot \frac{X + \frac{1}{\eta_P}}{1+X} + \frac{1-Y}{1+X} \cdot \left(1 - \frac{1}{\eta_P}\right); \tag{1.10}$$

[2] A polytropic process follows the relation $pv^n = C$, where n is the polytropic exponent([61]). Thus, it is possible to write these relationships

$$pv^n = p_s v_s^n; \quad \Longrightarrow \quad v = v_s \left(\frac{p_s}{p}\right)^{\frac{1}{n}};$$

Since $\Delta h_P = \int_s^d v dp$, it follows that

$$\Delta h_P = \int_s^d v dp = v_s p_s^{\frac{1}{n}} \int_{p_s}^{p_d} p^{-\frac{1}{n}} dp = p_s v_s \frac{n}{n-1}\left[\left(\frac{p_d}{p_s}\right)^{\frac{n-1}{n}} - 1\right].$$

Considering that $pvM_w = Z_s R T_s$, and defining $\sigma = \frac{n-1}{n}$ we obtain

$$\Delta h_P = \frac{Z_s R T_s}{M_w} \frac{1}{\sigma}\left[\left(\frac{p_d}{p_s}\right)^{\sigma} - 1\right].$$

Equation (1.10) clearly states that σ is a function of η_P. Then, the average coefficient $\bar{\sigma}$ is equal to

$$\bar{\sigma} = \frac{\sigma_s + \sigma_d}{2}. \tag{1.11}$$

Finally, merging equations 1.8 and 1.9 it is possible to find out Δh.

$$\Delta h = \frac{1}{\eta_P} \frac{Z_s \cdot R \cdot T_s}{M_w} \cdot \frac{\left(\frac{p_d}{p_s}\right)^{\bar{\sigma}} - 1}{\bar{\sigma}}. \tag{1.12}$$

As done in paragraph 1.2.1 and 1.2.2, figure 1.9 shows the percentage deviation in CC power calculation introduced by the same additive white Gaussian noises on each measurement.

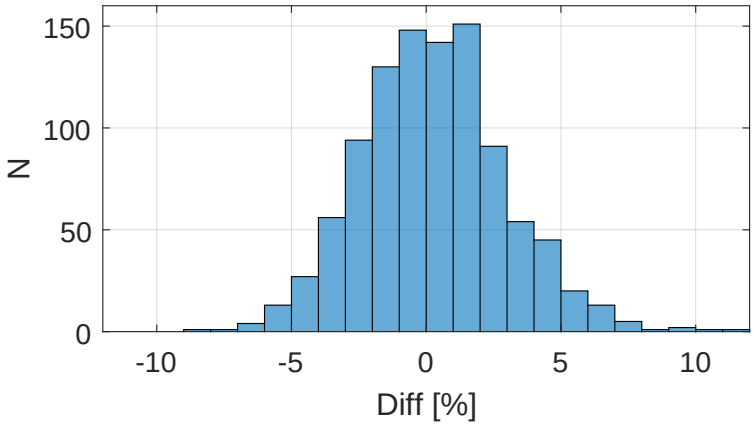

Figure 1.9: Deviation with respect to case without noise using method [C] ($\mu = -0.28\%$, $\sigma = 2.71\%$).

1.2.4 CC power estimation: results

Sensitivity analysis

As shown in figure 1.6, 1.8 and 1.9 all the three methods preserve the Gaussian shape, with a mean value μ very close to 0. Nevertheless, the same de-

viations on the inputs do not lead to similar deviations on power estimations and this is due to the fact that different methods have different sensitivity with respect to the same inputs. Table 1.2 summarises the results of the sensitivity analysis. Table 1.2 states that method [C] is statistically more sensitive with respect to input noises, thus the centrifugal compressor power estimation provided by this method is the most affected by the inaccuracy of input measurement.

	μ	σ
method [A]	-0.02%	1.92%
method [B]	-0.23%	1.51%
method [C]	-0.28%	2.71%

Table 1.2: Outcomes of sensitivity analysis of methods [A], [B] and [C].

Estimation error

Sensitivity analysis describes how the results are conditioned by inputs variations, but it is not enough to evaluate the quality of the estimation method. In order to assess the accuracy of the three methods it is necessary to feed each method with real field data and compare the results with the power measurement provided by a suitable field device. In turbo-compression industrial applications, like the one under investigation, a direct power measurement system is not usually needed; nevertheless, when it is strictly required[3], torque-meters are commonly used (to retrieve more details about torque-meters please refer to [93]). It is worth noticing that this transducer is affected by great inaccuracies (up to 10% in case of wrong calibration), thus the errors defined with respect to this measurement have to be weighted under the light of accuracy of each particular transducer. This is due to the

[3] In some country LNG plants (*Liquefied Natural Gas*) are obliged by law to measure and declare the absorbed power for tax purposes.

nature of torque-meters, indeed the quality of the measurements is strictly connected with a correct calibration phase. As shown in figure 1.10, the torque measurement is indirectly achieved by evaluating the angular displacement $\Delta\vartheta$ between the extremities of the torque-meter; indeed, considering that the instrument has an equivalent torsional stiffness equal to K, when the torque-meter is excited with a torque T then $\Delta\vartheta$ should be equal to T/K. Coefficient K obviously is not constant and varies with different factors (for instance a temperature compensation is usually needed), and this is the reason why calibration procedures are so important.

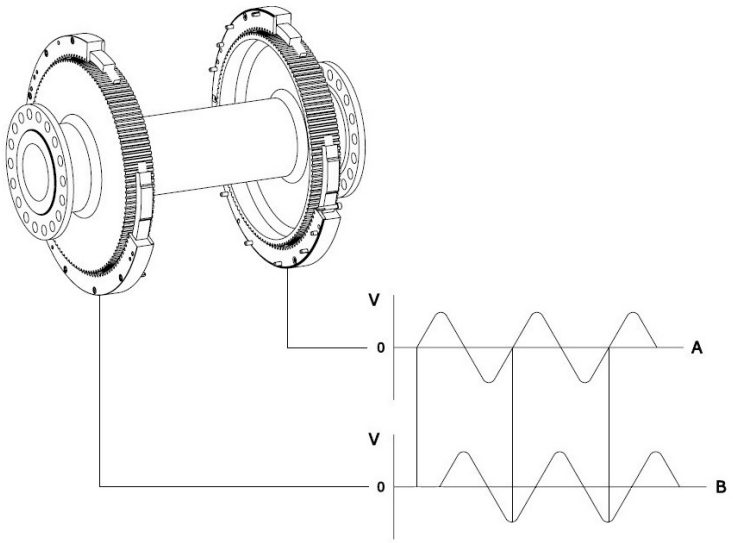

Figure 1.10: Generic schematic of a torque-meter.

Figure 1.11 shows some results obtained by exploiting four different datasets taken from real sites ($T_{scan} = 1280\,ms$). These plots represent the percentage difference between the power value provided by torque-meter and the power estimation based respectively on method [A] (blue line), method [B] (orange line) and method [C] (yellow line).

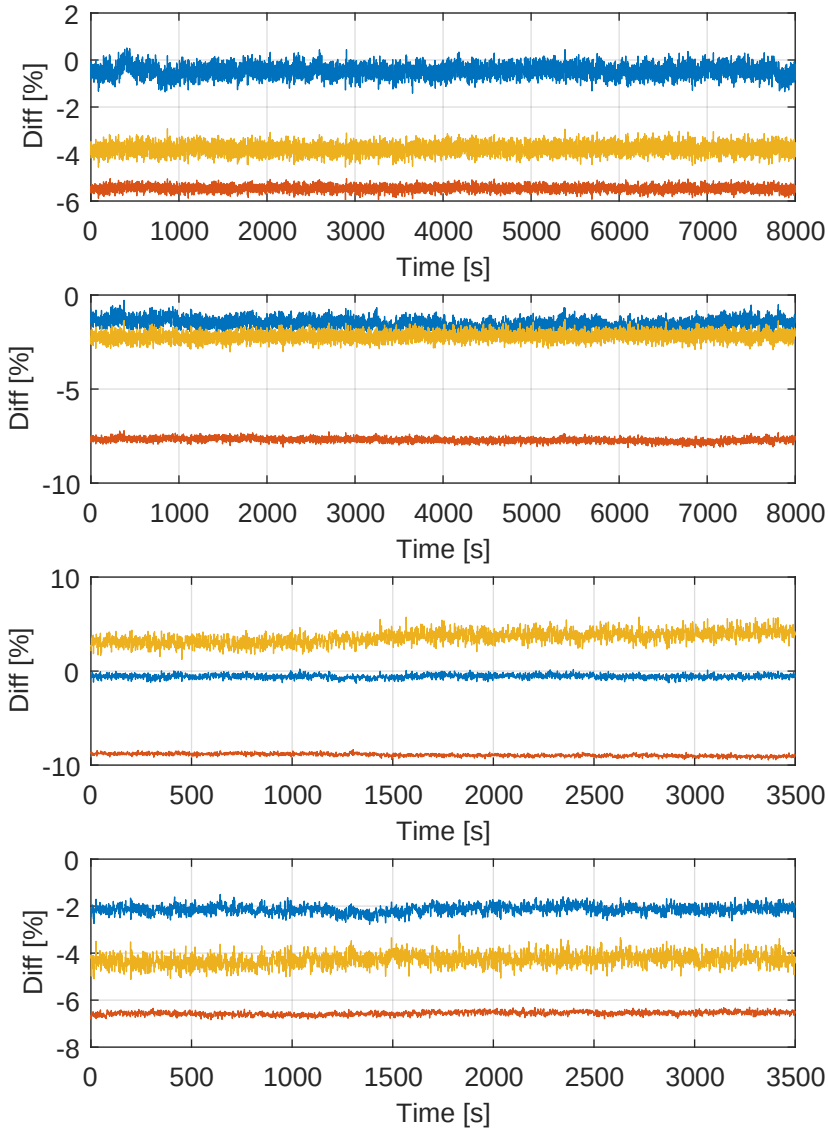

Figure 1.11: Percentage errors of centrifugal compressor power estimation based on method [A] (blue line), method [B] (orange line) and method [C] (yellow line).

Results of figure 1.11 have been confirmed repeating the estimation with other trends, and they can be summarised as follows:

i. Different tests lead to different errors, therefore the errors are not only due to the methods but they are in some way connected to the characteristics and non-idealities of the particular site setup.

ii. Despite the absolute value of the errors, all the three methods are characterised by a nearly constant percentage error. Considering that the measured power undergoes significant variation within the estimation interval, this means that each estimation method features a constant bias with respect to the reference. Standing from the inaccuracy that might affect the torque-meter this is a very appreciable feature;

iii. Method [A], which is based only on gas properties and transformations, seems to guarantee better results. However, it is worth noticing that methods [B] and [C] rely on non-dimensional map, and these results are based on *Expected Maps*, thus they do not take into account the peculiarities of each machine as *As-Tested maps* do. As already mentioned, *Expected maps* are ideal compressor maps computed during the design phase of the CC, while *As-Tested maps* are real compressor maps confirmed by tests and measurements taken on CC in real operating conditions and various operating points.

1.2.5 Method [C2]: compressor polytropic efficiency with model-based correction

This additional method is very similar to method [C], but it introduces a correction based on the analytical prediction of discharge temperature $\hat{T}_d$ based on the theory of polytropic compression

$$\hat{T}_d = T_s \cdot \left(\frac{p_d}{p_s} \right)^{\sigma(\eta_P)} . \tag{1.13}$$

Equation (1.13) can be easily retrieved starting from the definition of σ

$$\sigma = \frac{\ln\left(\frac{T_d}{T_s}\right)}{\ln\left(\frac{p_d}{p_s}\right)}, \tag{1.14}$$

that directly derives from the thermodynamic theory of a polytropic expansion or compression[4].

The main idea behind this method [C2], as shown in figure 1.12, is to find out the value of polytropic efficiency $\hat{\eta}_P$ that makes the predicted value of discharge pressure to coincide with the measured one, i.e.

$$\hat{T}_d(\hat{\eta}_P) = T_d^{meas}.$$

This method [C2] could also be based on the prediction of p_d; indeed, an equation similar to (1.13) can be derived concerning $\hat{p}_d$. However, by construction, the value $\hat{\eta}_P$ that would make $\hat{p}_d$ to match with the measured value p_d is exactly the same value obtained exploiting the prediction of the discharge temperature.

[4] A polytropic expansion follows this pressure-temperature relationship (for a complete proof see [61])

$$\frac{p^{n-1}}{T^n} = C,$$

where n is the polytropic exponent and C a constant. This means that for an arbitrary compression the following equation is satisfied

$$\frac{p_d^{\frac{n-1}{n}}}{T_d} = \frac{p_s^{\frac{n-1}{n}}}{T_s}.$$

It is possible to demonstrate that the quantity $\sigma = \frac{n-1}{n}$ is a function of the polytropic efficiency η_P, thus

$$\sigma(\eta_P) = \frac{n-1}{n} = \frac{\gamma - 1}{\gamma \eta_P},$$

where $\gamma = \frac{c_p}{c_v}$. Finally, we obtain the desired relationship

$$\frac{T_d}{T_s} = \left(\frac{p_d}{p_s}\right)^{\sigma(\eta_P)}.$$

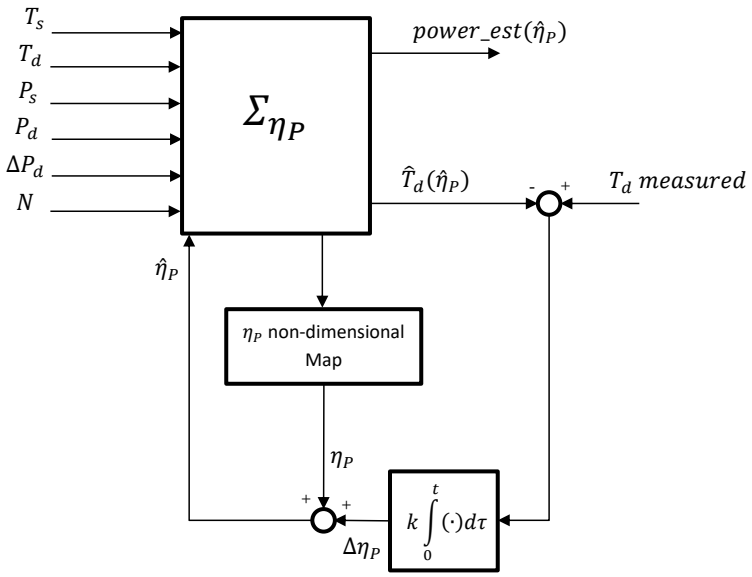

Figure 1.12: Schematic of method [C2].

Method [C2]: results

Figure 1.13 features the results of method [C2] (orange line) and method [C] (blue line). Note that the method has been applied to the same four datasets relative to figure 1.11.

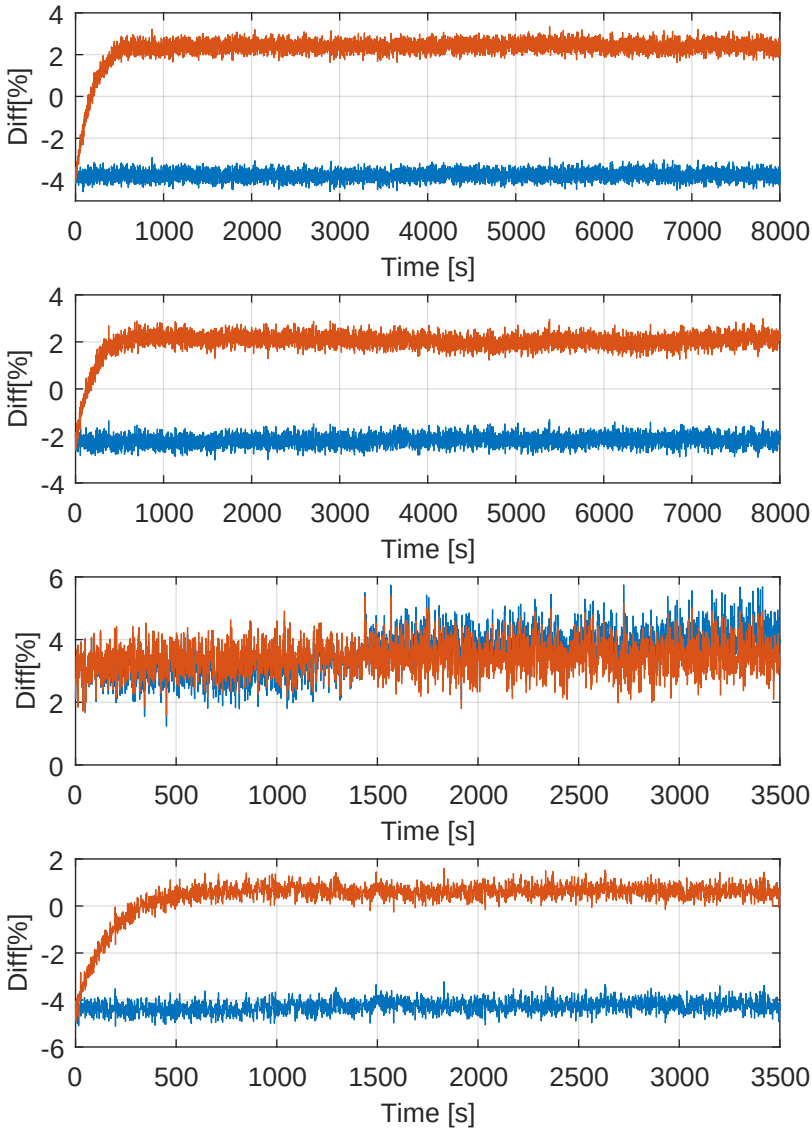

Figure 1.13: Percentage errors of centrifugal compressor power estimation based on method [C] (blue line) and method [C2] (orange line).

Even in this case it does not seem possible to define a general behaviour pattern of this method, however method [C2] generally guarantee better results with respect to method [C]. Furthermore, figure 1.13 clearly shows that the percentage errors relative to method [C2] are usually characterised by an initial transient phase due to the time needed by $\Delta\eta_P$ to converge to a nearly constant value.

The reason of the improvement introduced with method [C2] is the fact that the polytropic efficiency is not retrieved only from a scheduled map, indeed it is corrected thanks to direct measurement of discharge temperature T_d.

1.3 Robustness with respect to measurements

All the power estimation methods presented in section 1.2 rely on some of the six sensors represented in figure 1.5; obviously not all the methods exploit all the six measurements, but the point now is that every method needs to be fed by inputs provided by some kind of sensors.

Thus, the question is: how is it possible to improve the robustness of a generic estimation method with respect to one or more of these six measurements? Let's suppose that one of the six measurements suddenly becomes unavailable; is it possible to compensate this information leakage by using the remaining five, or all the measurements are strictly required? These questions do not have specific answers, indeed some measurements are strictly necessary to keep the system working. For instance, rotating speed measurements are very important, thus a typical industry setup includes two or three transducers to guarantee the redundancy of this basic measurement. Rotating speed awareness is so important that it does not make any sense to suppose the unavailability of this measurement, indeed in that case the system would automatically shut down.

On the other hand, sometimes there are other sensors that are very useful even if they are not essential. Concerning the proposed methods introduced to estimate the power needed to drive a centrifugal compressor, it would be

very appreciable to find out some techniques to make the system able to turn around the temporary unavailability of a sensor. To reach this aim two main techniques have been investigated:

- A technique exclusively based on *Recursive Least Squares* theory (RLS, see section B.2 in appendix B);
- A technique based both on thermodynamic formulae and RLS theory.

1.3.1 Absolute least squares estimation

The six measurements provided by the sensors of the centrifugal compressor are not independent, thus the system seems to be overdetermined. The main idea of this method is to identify the model that takes as input five measurements and returns as output the estimation of the sixth one. Without loss of generality, let's suppose that the unavailable measurement that must be estimated is T_d. Obviously, the model structure is unknown and the first step is its definition.

The simplest model is the parametric linear one: this model is completely defined once that the N-dimensional parameters vector $\boldsymbol{\vartheta} = [\vartheta^1, \vartheta^2, \ldots, \vartheta^N]$ is known. This model can take as input also non-linear combinations of the measurements, but it must be linear with respect to the parameters ϑ^i, $i = 1, \ldots, N$. Let's define the N-dimensional input vector $\boldsymbol{\varphi} = \boldsymbol{f}(p_s, T_s, p_d, \Delta p, N) \in \mathbb{R}^N$, the parametric linear model can be written as

$$\Sigma(\boldsymbol{\vartheta}) : \; T_d = \boldsymbol{\varphi}^T \boldsymbol{\vartheta}. \tag{1.15}$$

The parameters vector $\boldsymbol{\vartheta}$ can be estimated exploiting the least squares method. As shown in appendix B, least squares can be applied in two different ways: classic or recursive least squares.

In the past years, least squares method has already been employed in turbomachinery applications. For instance, it has been applied to balance rotating machineries ([33], [109] and [59]) and to perform parameters and

coefficients identification in centrifugual compressors ([76]) or in turbine engines ([65] and [12]). In this framework least squares are applied in a different way, indeed the main purpose is to find out how different CC measurements are connected between each other.

Hereafter recursive least squares (RLS) will be used, indeed such method updates the estimation step by step and it converges exactly to the same result of classic least squares. Since the model is linear, an analytical solution can be defined. Obviously, to perform the least squares method, the measurement of the variable that has to be estimated at least in a first phase must be available. Once that the parameters vector has been estimated, if the measurement becomes unavailable it can be estimated introducing $\hat{\boldsymbol{\vartheta}}$ in the parametric linear model.

This simple idea is represented in figure 1.14: clearly the loop is closed only when T_d is available, otherwise the system works in open-loop and the estimation $\hat{T}_d$ is based on the last estimation of $\boldsymbol{\vartheta}$.

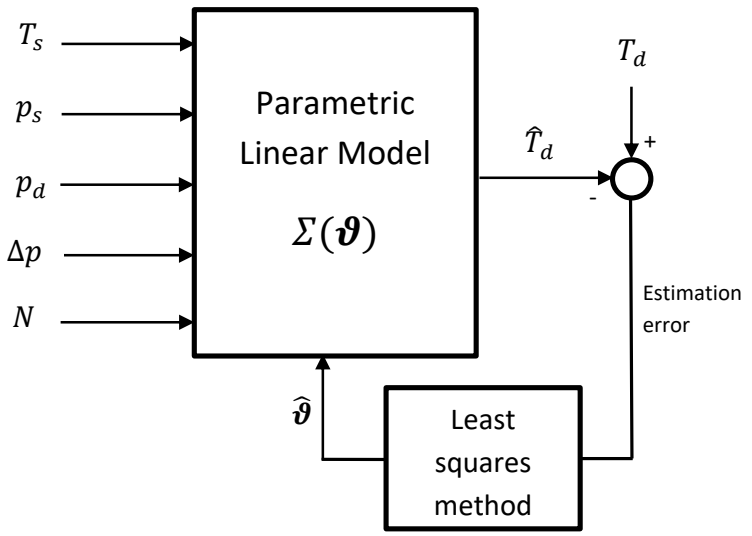

Figure 1.14: Schematic of T_d absolute estimation based on least squares theory.

In order to simulate this scenario a real dataset has been split in two separated phases. In the former part (10% of total data) all the measurements are considered available, thus within this interval it is possible to compute vector $\hat{\boldsymbol{\vartheta}}$. In the latter interval (last 90% of data) T_d is considered unknown and it is estimated using the least squares theory.

Obviously this procedure can be repeated for each measurement, thus each quantity will have its own coefficient vector.

Figure 1.15 is composed of five subplots relative to these tests:

1. $y = T_s$, $\boldsymbol{\varphi} = [p_s \quad T_d \quad p_d \quad \Delta p \quad N]$;
2. $y = p_s$, $\boldsymbol{\varphi} = [T_s \quad T_d \quad p_d \quad \Delta p \quad N]$;
3. $y = T_d$, $\boldsymbol{\varphi} = [T_s \quad p_s \quad p_d \quad \Delta p \quad N]$;
4. $y = p_d$, $\boldsymbol{\varphi} = [T_s \quad p_d \quad T_d \quad \Delta p \quad N]$;
5. $y = \Delta p$, $\boldsymbol{\varphi} = [T_s \quad p_s \quad T_d \quad p_d \quad N]$;

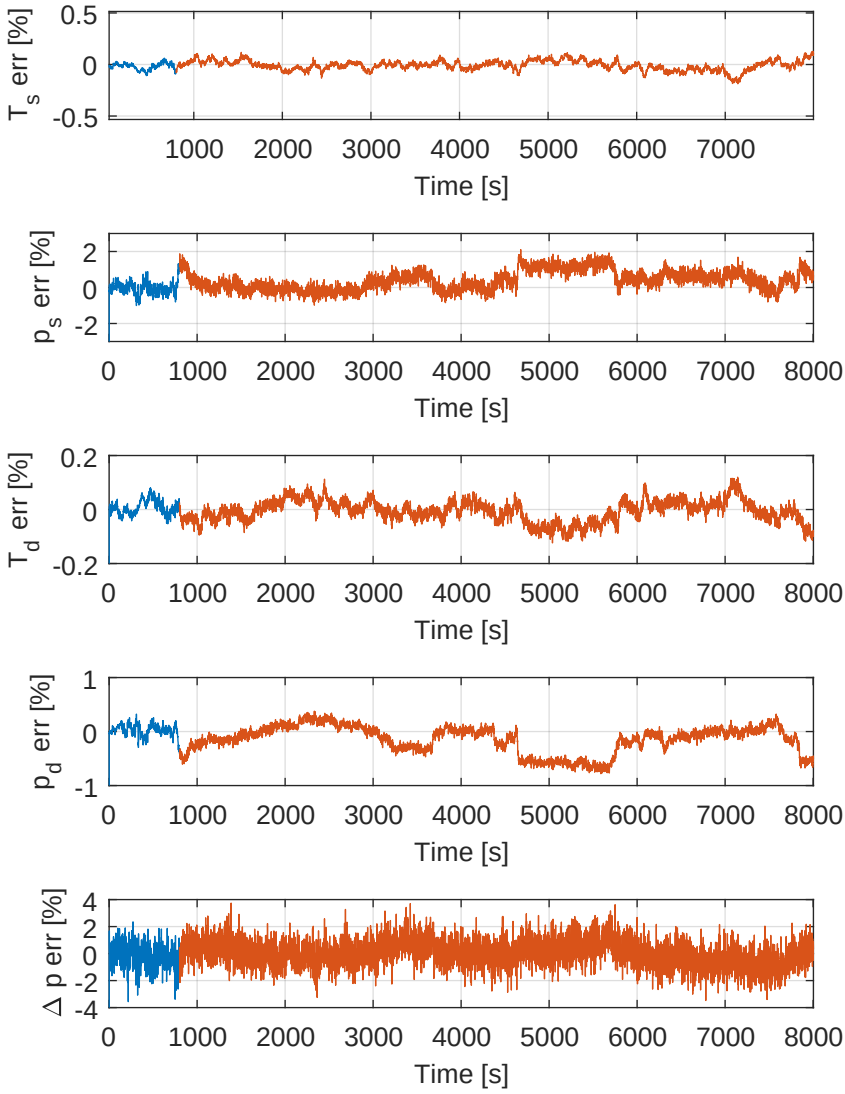

Figure 1.15: Percentage errors of absolute estimations based on least squares theory. Blue line (10% of total data) refers to calibration phase, while orange line (last 90% of data) refers to validation interval.

1.3.2 Thermodynamic prediction and RLS estimation

Gas compression can be completely described from a physical point of view. Equation (1.14) is valid for a polytropic process and by the inversion of this equation it is easy to achieve an analytic formulation for the thermodynamic prediction of T_s, p_s, T_d and p_d.

$$\hat{T}_s = T_d \cdot \left(\frac{p_s}{p_d}\right)^{\sigma}; \tag{1.16}$$

$$\hat{p}_s = p_d \cdot \left(\frac{T_s}{T_d}\right)^{\frac{1}{\sigma}}; \tag{1.17}$$

$$\hat{T}_d = T_s \cdot \left(\frac{p_d}{p_s}\right)^{\sigma}; \tag{1.18}$$

$$\hat{p}_d = p_s \cdot \left(\frac{T_d}{T_s}\right)^{\frac{1}{\sigma}}. \tag{1.19}$$

Using these prediction formulae it is possible to achieve an estimation of these variables. Figure 1.16 represents the results of these thermodynamic predictions. Note that the differential pressure across the orifice can not be estimated in this way, indeed this quantity is not involved in equation (1.14).

Figure 1.16 clearly shows that the thermodynamic predictions provide a first approximation, but the error can be significant (up to 10%). This is due to the non-idealities that move the real CC behaviour far away from ideal polytropic compression. This means that the performance of this estimation method is strictly connected with the particular features of the compressor and its operating conditions. The more the compressor is far from the ideal one, the larger the prediction errors will be. A great advantage of this method is that it never relies on the measurement of the possibly unavailable quantity, indeed it does not require any calibration phase and it achieves an estimation exploiting only physical relationships. Even if this method does not guarantee a great accuracy it gives however a first information, indeed the error is nearly constant. This means that the prediction somehow follows

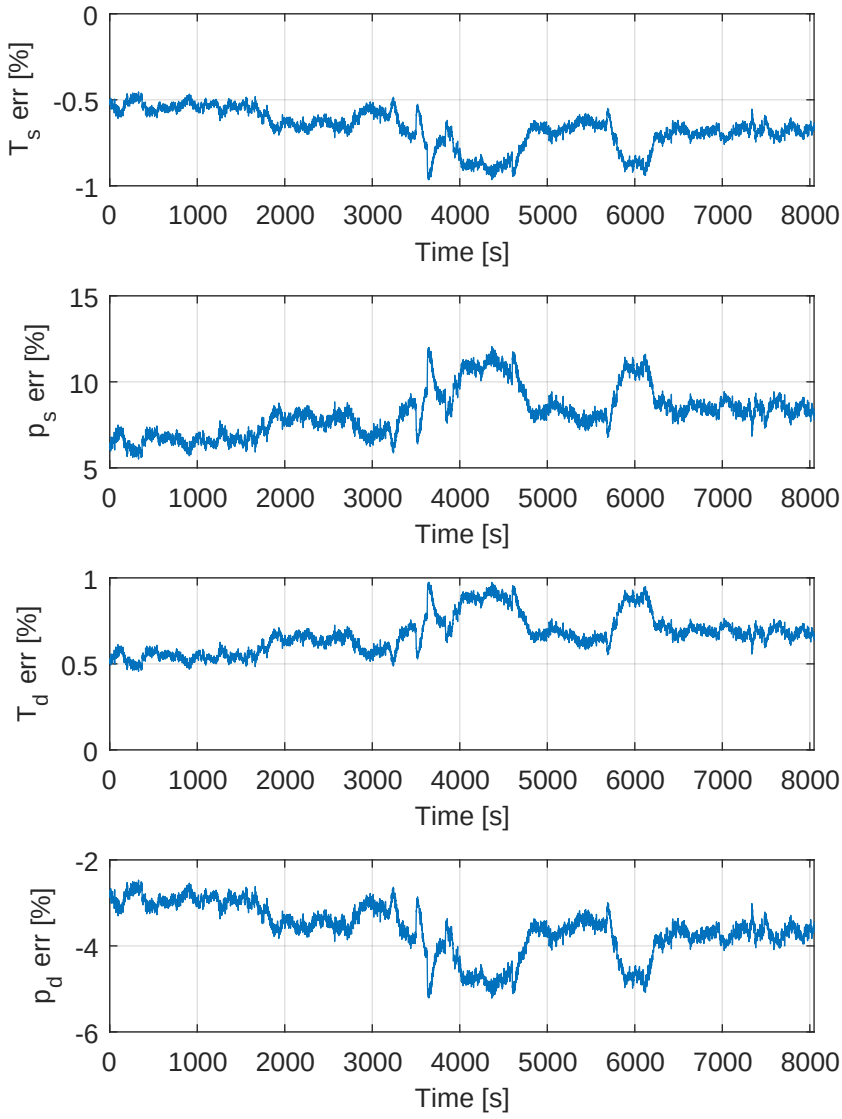

Figure 1.16: Percentage errors of thermodynamic predictions.

the changing of the unknown variable, therefore the natural improvement is to start from this result and try to compensate in some way the prediction error. This can be made exploiting again RLS, as shown in figure 1.17. In this case, the purpose of RLS is not the absolute estimation of one measurement, but it aims to estimate the difference between the thermodynamic prediction and the measured value.

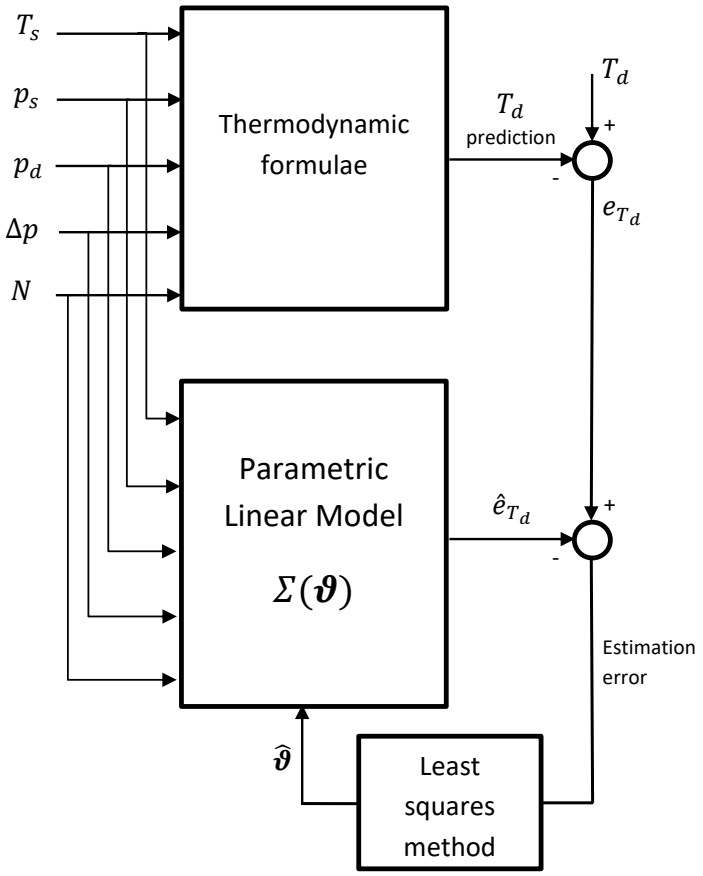

Figure 1.17: Schematic of T_d prediction error estimation based on RLS theory.

In practice, the idea is to estimate ε_{T_s}, ε_{p_s}, ε_{T_d} and ε_{p_d}, defined as

$$\begin{aligned}
\varepsilon_{T_s} &= T_s^{meas} - \hat{T}_s; \\
\varepsilon_{p_s} &= p_s^{meas} - \hat{p}_s; \\
\varepsilon_{T_d} &= T_d^{meas} - \hat{T}_d; \\
\varepsilon_{p_d} &= p_d^{meas} - \hat{p}_d.
\end{aligned}$$

Figure 1.18 shows that this second method leads to significantly lower errors with respect to simple predictions. Moreover, even if the magnitudes of the estimation errors are similar to the ones obtained with absolute RLS estimation, this method deserves to be preferred because it is not only a "blind" estimation but it starts from a reasonable results based on compression theory.

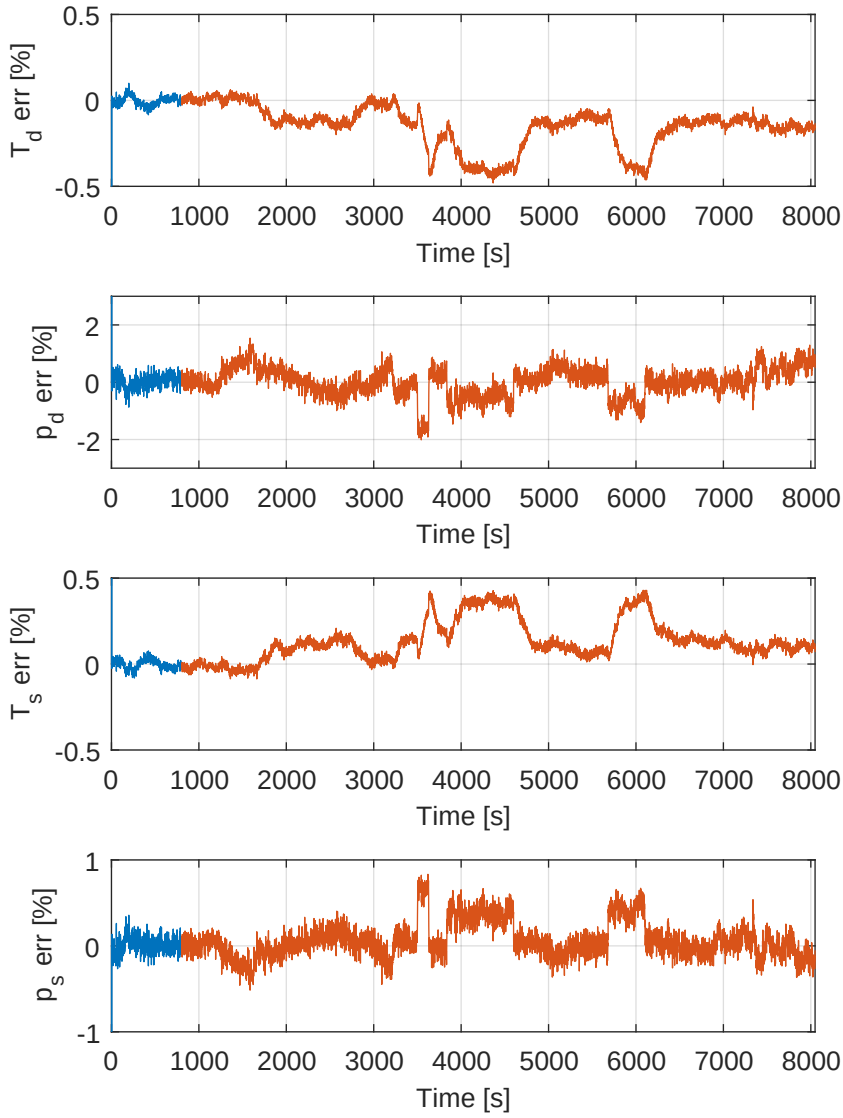

Figure 1.18: Percentage errors obtained estimating the thermodynamic prediction error with RLS. Blue line (10% of total data) refers to calibration phase, while orange line (last 90% of data) refers to validation interval.

1.4 Results analysis and conclusions

The methods proposed in this chapter have been developed to meet practical and technological needs. Concerning typical CC applications power measurement is not strictly required. On the other hand, the knowledge about GT power is fundamental to figure out the GT operating point. Thus, considering that CCs are usually driven by GTs, the information about the absorbed power can be exploited as GT delivered power estimator.

The power absorbed by the CC can be directly measured by torquemeters, but such sensors have many drawbacks, indeed they are expensive, bulky and they need to be frequently calibrated in order to guarantee acceptable accuracy. The proposed techniques provide an estimation of the absorbed power avoiding torque-meter installation, and this is the reason why they are so appreciable.

This chapter can be broadly split in two different parts:

i. in the first part some suitable model-based methods to estimate the power needed to drive a centrifugal compressor have been proposed. As mentioned in paragraph 1.2.4, methods [A], [B] and [C] lead to nearly constant percentage error, even if different tests are characterised by different errors. However, method [A] seems to guarantee better results, while the performances of methods [B] and [C] are strictly connected to the goodness of the empirical maps that try to describe the CC behaviour. In this framework the importance of introducing *As-Tested maps* instead of *Expected maps* is crucial, and it can bring many benefits. Moreover, an additional method [C2] is proposed: this method tries to enhance method [C] by introducing a model-based correction of the polytropic efficiency. Even in this case it is hard to define a general pattern, indeed different datasets lead to different results. Nevertheless, method [C2] generally guarantees better results with respect to method [C];

ii. in the second part some methods to compensate the potential unavailability of some sensors are investigated. The main idea is that CC

measurements taken from suction and discharge are not independent, indeed they are linked with each other by thermodynamic relationships that describe gas compression. The proposed methods exploit RLS theory and thermodynamic relationships in order to achieve a suitable estimation of the potentially unavailable measurement. Empirical results based on real trend data show that the minimum estimation error can be achieved exploiting at the same time both the thermodynamic predictions and RLS theory.

Chapter 2

Sub-Synchronous Torsional Interactions in Electrical Networks

Turbo-generators (TGs) interact with electrical network and significant torsional vibrations at shaft natural frequencies can be produced. The first part of this chapter introduces sub-synchronous torsional interactions, with a brief survey of the main causes and effects of this phenomenon. The second part suggests a possible solution to mitigate this issue and some theoretical results are presented.

2.1 General description

SSTI (*Sub-Synchronous Torsional Interaction*) is an instability phenomenon mainly associated with synchronous machines and various power electronic devices that are widely used in oil and gas industry, such as HVDC converters (*High Voltage Direct Current*) or large industrial motor drives that create and sustain the oscillations ([90], [81], [11] and [41]). The presence of these devices has grown exponentially in the last decade, particularly for *Variable Frequency Drive* application (VFD); these equipments are mainly used in electro-mechanical systems to control AC motor speed and torque by varying

motor input frequency and voltage. VFDs can produce a massive current and voltage harmonic distortion, and this is the first step to trigger SSTI oscillations.

SSTI as a non-linear phenomenon has been widely studied in the past decades ([45]), and it can not be understood by considering the electrical and mechanical parts as separated worlds: looking at these two systems one by one the mechanical/electrical fluctuations can not be explained, they seem to be self-generated and self-sustained oscillations. The causes and the reasons behind this very critical behaviour of electric generation plants have to be searched considering a single system where the electric part (electric network and electronic devices) and the mechanical part (gas turbines and generators) transfer energy to each other. Figure 2.1 depicts a very schematic electric grid powered by turbo-generators (even if the grid is a three-phase network, for the sake of simplicity the schematic is represented as a single-line diagram).

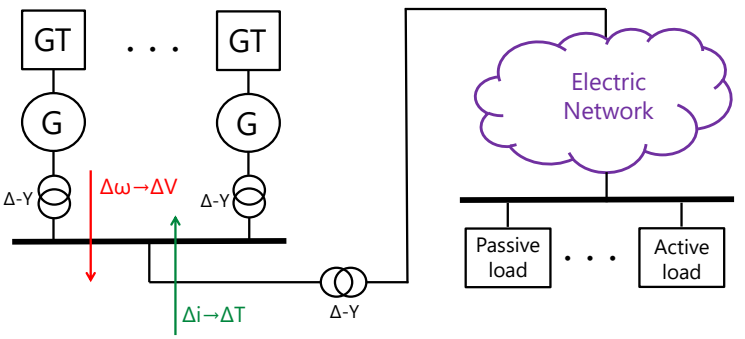

Figure 2.1: Schematic explanation of SSTI phenomenon.

As any other rotating mechanical component, TGs have their own *Torsional Natural Frequencies* (TNFs). Usually, the first torsional mode is dominant, and in correspondence of this frequency the behaviour of the mechanical system becomes very unstable. If an external source of energy feeds a TGs in correspondence of the first TNF (1TNF) the system will begin to

oscillate with undamped vibrations. The oscillation $\Delta\omega$ of the shaft line, i.e. variations in rotational speed with respect to the reference speed, is defined as

$$\Delta\omega = \omega^{act} - \omega^{ref},$$

where ω^{act} is the actual angular speed of the shaft line, while ω^{ref} is the reference angular speed which is directly connected to the reference frequency of the network (50 or $60\,Hz$). $\Delta\omega$ creates voltage oscillation ΔV. Electric network sees these voltage variations as disturbances, thus it injects in the grid significant current oscillations Δi. On the contrary, TGs see the current oscillations as electric torque oscillations (ΔT_e), and this is the external source of energy that excites the mechanical system exactly where it is more sensitive, i.e. in correspondence of 1TNF. This is a very intuitive explanation of how the SSTI phenomenon can be produced and self sustained: obviously each single plant has its own peculiarities, and they have to be considered in order to assess the actual SSTI risk and, possibly, its mitigation.

SSTI vibrations can cause cumulative fatigue damage and result in reduced component life of parts such as shafts, buckets (blades), retaining rings, and rotors. However, in addition to physical damages on the plant, this phenomenon heavily affects the operability of the system, indeed when seismic sensors detect too large oscillations the system is automatically shut down in order to protect itself and preserve the surrounding workers' safety. In order to avoid this critical situation SSTI causes have to be studied and some mitigation techniques need to be introduced (e.g. see [90], [79], [52], [85] and [91]).

2.2 SSTI electro-mechanical causes

TGs shafts have to transmit driving torque to the load (i.e. electric network) and they have also to absorb the transient torque that characterises step events or faults. As mentioned in the previous paragraph, under certain conditions they can experience self-sustained or growing oscillations due to SSTI. In order to find out SSTI main causes first of all it is necessary to

introduce a mechanical model of TG to better understand why the system tends to oscillate in correspondence of specific frequencies. Then, it is necessary to analyse the electric grid in order to explain why certain devices in some configurations create disturbances that feed the torsional oscillations.

2.2.1 Turbo-generators mechanical model

The first step to explain this phenomenon is the introduction of a mathematical model of TG mechanics. The modal approach (see e.g. [44], [46] and [104]) allows the calculation of the characteristic TNFs of the train usually composed of a GT, a gear box and an EG.

As shown in figure 2.2, TG shaft can be seen as a sequence of N inertias J_i characterised by damping coefficients D_i, with $i = 1, \cdots, N$, and interconnected by equivalent stiffness coefficients k_j, $j = 1, \cdots, N-1$.

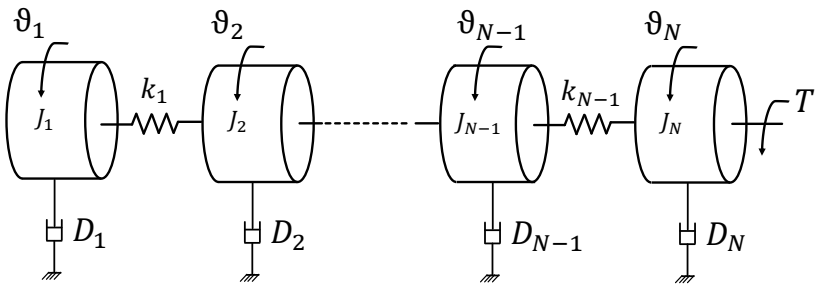

Figure 2.2: Physical model of TG shaft.

The shaft torsional dynamic behaviour is completely described by the following set of second order differential equations

$$\boldsymbol{J}\ddot{\boldsymbol{\vartheta}} + \boldsymbol{D}\dot{\boldsymbol{\vartheta}} + \boldsymbol{K}\boldsymbol{\vartheta} = \boldsymbol{T}. \tag{2.1}$$

Where:

$\boldsymbol{J}$ = diagonal matrix of physical inertias

$\boldsymbol{D}$ = diagonal matrix of physical damping coefficients

$\boldsymbol{K}$ = symmetric matrix of equivalent stiffness coefficients

$\boldsymbol{\vartheta}$ = vector of angular positions of each inertia

$\boldsymbol{T}$ = torques vector (both electric and mechanical)

In a power generation system, in addition to mechanical damping there is also an electrical damping which is acting on the generator shaft; this electrical damping is linked to the electrical torque which is due to the interaction between the network and the generator magnetic flux. In practice, considering small oscillations in correspondence of a certain frequency f_n, electrical torque and speed oscillations can be seen as rotating phasors, respectively $\boldsymbol{\Delta T}_e(f_n)$ and $\boldsymbol{\Delta\omega}(f_n)$.

Electrical damping acts on generator shaft windings, and it describes the amplification and the phase delay between speed oscillations and electrical torque. Mathematically, it is defined as

$$D_e(f_n) = -\frac{|\boldsymbol{\Delta T}_e(f_n)|}{|\boldsymbol{\Delta\omega}(f_n)|} cos\alpha, \tag{2.2}$$

where α is the phase delay between the phasors. D_e obviously depends on α and it can be either positive or negative. Since the total damping coefficient is a combination of the mechanical and electrical damper coefficients, it is clear that a negative D_e can lead the system towards instability.

The drawback of equation (2.1) is that it is very complex to figure out the numerical values of its coefficients. In order to overcome this issue it is possible to represent the same equation in the modal reference system through this coordinate transformation

$$\boldsymbol{\vartheta} = \boldsymbol{\Phi} \cdot \boldsymbol{q}. \tag{2.3}$$

Where:

$\boldsymbol{\Phi}$ = modal shapes matrix (calculated as the eigenvectors of $\boldsymbol{J}^{-1}\boldsymbol{K}$)

$\boldsymbol{q}$ = modal coordinates vector

Theory fundamentals about modal analysis can be found in many handbooks such as [5], [86] or [69].

By applying this transformation, equation (2.1) becomes

$$\boldsymbol{M}_{eq}\ddot{\boldsymbol{q}} + \boldsymbol{D}_{eq}\dot{\boldsymbol{q}} + \boldsymbol{K}_{eq}\boldsymbol{q} = \boldsymbol{T}_{eq}. \tag{2.4}$$

Where:
$\boldsymbol{M}_{eq} = \boldsymbol{\Phi}^T \boldsymbol{J} \boldsymbol{\Phi}$ is a diagonal matrix
$\boldsymbol{D}_{eq} = \boldsymbol{\Phi}^T \boldsymbol{D} \boldsymbol{\Phi}$ is a diagonal matrix
$\boldsymbol{K}_{eq} = \boldsymbol{\Phi}^T \boldsymbol{K} \boldsymbol{\Phi}$ is a diagonal matrix

Solving this new set of differential equations it is possible to figure out all torsional modes relative to each single TNF. The major criticality is related to the first mode, thus it is reasonable to focus the attention only on 1TNF, which considering common size and inertias in practical applications in the oil and gas industry usually is lower than $10\,Hz$. The normalised amplitude of this first torsional mode gives a first quantitative information on how the mechanical system amplifies the torque/speed oscillations at 1TNF. Torque and speed oscillations are linearly connected by equivalent stiffness, thus if one gets larger also the other one is amplified by the same factor.

Therefore, the higher is this amplification the lower will be the total equivalent damping coefficient; this is due to the fact that if the electric torque is more amplified in correspondence of generator windings then the electric damping coefficient has a greater weight in the calculation. In some cases the amplitude of the first torsional mode is particularly large, thus the total equivalent damping coefficient can be lower than 0, and this means that the system is not able to damp the oscillations with frequency equal to 1TNF, thus the stability is not guaranteed.

2.3 Harmonic distortion in the electric network

It is well-known that a three-phase electric power transmission and distribution system is theoretically characterised by a balanced and symmetric configuration, where each line carries an alternating current of the same frequency f and amplitude I; the reason why the system is perfectly balanced is that in the phase plane the three phase currents present a phase delay equal to $2\pi/3$, and this forces the sum of the three currents to zero. Obviously, also the three line voltages have the same amplitude V and the same frequency f, and they are delayed each other in the phase plane of $2\pi/3$. Indicating with "a", "b" and "c" each line, equations (2.5) and (2.6) describe the ideal currents and voltages of a symmetric three-phase system.

$$\begin{cases} v_a(t) = V sin(2\pi f t); \\ v_b(t) = V sin(2\pi f t - \frac{2}{3}\pi); \\ v_c(t) = V sin(2\pi f t - \frac{4}{3}\pi). \end{cases} \tag{2.5}$$

$$\begin{cases} i_a(t) = I sin(2\pi f t - \varphi); \\ i_b(t) = I sin(2\pi f t - \varphi - \frac{2}{3}\pi); \\ i_c(t) = I sin(2\pi f t - \varphi - \frac{4}{3}\pi). \end{cases} \tag{2.6}$$

Where the additional phase delay φ between each current and the corresponding voltage is due to the power factor (PF) that is lower than one, thus the real power delivered to the load is lower than the apparent power[1]. This would be the behaviour of a linear electric network with a perfectly balanced load.

Actually, as introduced in section 2.1, many modern industrial applications are based on non-linear electronic devices such as VFD, LCI (*Load Commutated Inverter*) and HVDC. These equipments usually rely on controlled micro-electronics components (e.g. diodes, transistors and thyristors)

[1]PF is defined as $PF = cos\varphi$ therefore it is equal to 1 only when $\varphi = 0$, i.e. when the load is completely resistive (for further details see [3]).

that are very useful to shape the current or voltage profiles in order to adapt them to the load needs. These devices bring many benefits, but one of the drawback is that they introduce a significant harmonic distortion within the electric network; this means that line currents and voltages consist of many other frequencies in addition to the standard frequency f (usually equal to 50 or $60\,Hz$). THD (*Total Harmonic Distortion*), as defined in equation (2.7), is an index that allow the quantification of the total distortion with respect to the first harmonic.

$$THD = \frac{\sqrt{A_2^2 + A_3^2 + A_4^2 + \cdots}}{A_1} \tag{2.7}$$

Where A_i with $i = 1, \cdots, N$ is the RMS (*Root Mean Square*) amplitude of the i-th harmonic. In practice, THD defines how significant are the higher harmonics with respect to the fundamental one.

Harmonic distortion can be one of the conditions that may cause SSTI phenomenon; as depicted on the left side of figure 2.3 when the amplitude of the line currents varies with frequency f_D (top), its spectrum is characterised by two side-bands in correspondence of $f - f_D$ and $f + f_D$ (bottom). On the right side of figure 2.3 the three-phase power (top) and its spectrum (bottom) are represented, and it is possible to see that if current line has two side-bands in correspondence of $f - f_D$ and $f + f_D$ then the power oscillates with frequency f_D, indeed its spectrum has a peak exactly at f_D. In this situation also the electric torque seen by the generator oscillates at the same frequency.

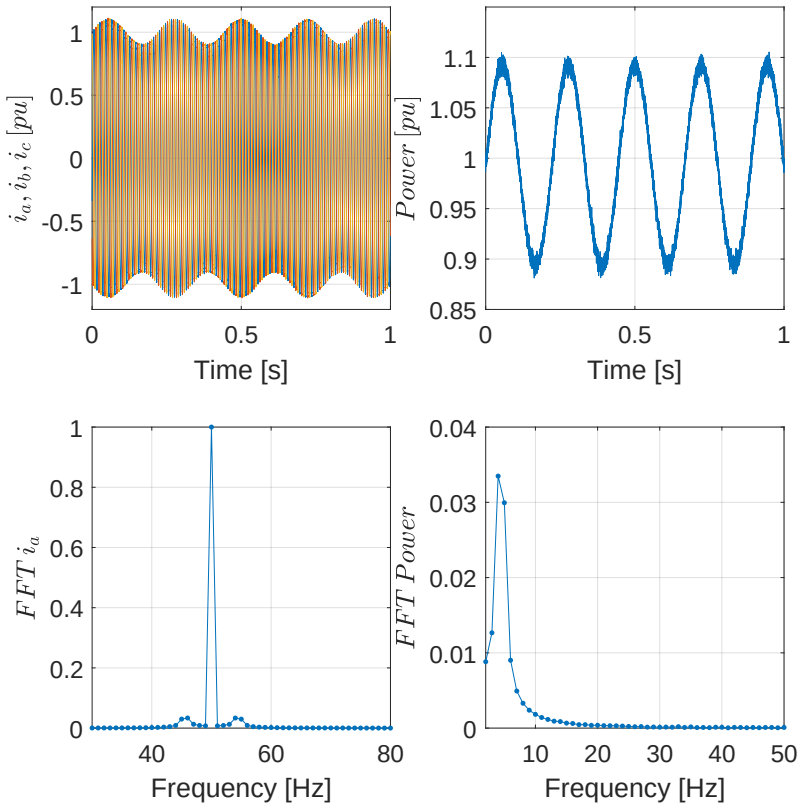

Figure 2.3: Frequency analysis of SSTI phenomenon (example). The figure is composed of two rows and two columns: first row is relative to time domain while the second is relative to frequency domain, first column is relative to current while the second is relative to power.

In the following, a few additional details and remarks about figure 2.3 are listed:

- This is only a simulated example built in MATLAB®, where all the quantities are normalised in per-unit (pu);

- the only purpose of this figure is to clarify some possible SSTI causes, the magnitude of the oscillations has been intentionally amplified to enhance the distortion;

- in order to achieve more realistic results the three line currents have been noised with an AWGN (*Additive White Gaussian Noise*);

- the reason why the peak of power spectrum is definitely lower than 1 pu is that the main component of the spectrum is the DC component, thus the y-axis has been scaled in order to highlight the peak at f_D.

From the previous simple example comes out that if f_D is equal to the first TNF of TG, then this particular load would excite the mechanical system in correspondence of its resonance frequency, therefore it should be able to activate and feed SSTI phenomenon. However, someone can note that in a real electric network it would be a very unlucky situation to have two perfect side-bands as the ones showed in this example, perfectly centered in $f - 1TNF$ and $f + 1TNF$. The fact is that the distortion introduced by non-linear load leads to disturbances in a wide range of frequencies that can include also the two side-bands, but the mechanical system is sensitive only to these specific frequencies and does not respond to the other ones. Therefore, it is clear that to trigger SSTI oscillations it is not strictly required to have a spectrum of line currents exactly equal to the one showed in figure 2.3, indeed it is just enough to have a continuous disturbance that insists within a frequency interval that contains the critical frequencies $f - 1TNF$ and $f + 1TNF$.

2.4 SSTI mitigation: damping system proposal

In section 2.2 the causes of Sub-Synchronous Torsional Interaction have been explained. The oscillations in the absorbed currents Δi lead to oscillation in the electric torque ΔT_e that finally leads to oscillations in the TG rotational speed $\Delta\omega$. In turn, mechanical oscillations $\Delta\omega$ produce oscillations ΔV and Δi within the electrical network, thus the loop is closed.

Figure 2.4 represents a schematic of a power generation unit with a SSTI damping system included.

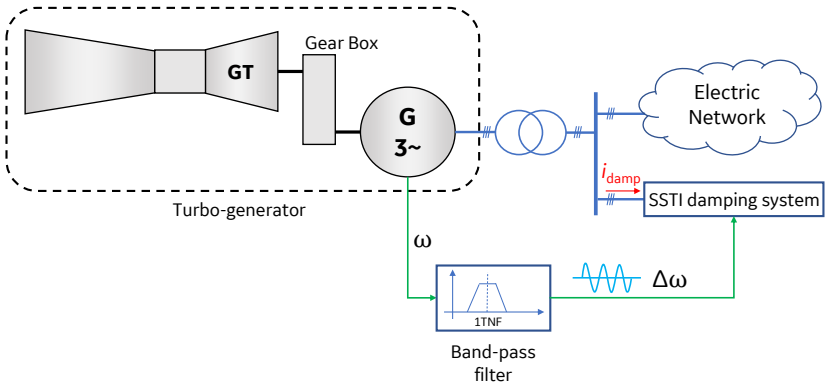

Figure 2.4: Schematic of SSTI mitigation system.

As shown in figure 2.4, the proposed SSTI damping system should be inserted within the electric network, indeed the main purpose is not a mechanical damping of the torsional vibrations but it aims to compensate the electric oscillations by introducing an active load. The active load is a controlled load that adapts its own request of power in function of the measured mechanical oscillations $\Delta\omega$. As described in [1] and [2], the measurement of the angular velocity of a rotating shaft is based on a cogwheel installed on the shaft itself. Once the angular velocity ω of the shaft is known, the harmonic at $1TNF$ can be isolated by introducing a simple band-pass filter centered in $1TNF$. Therefore, the main purpose of the damping system is to balance the fluctuations of electric power within the electric network. In this

way the power transfer at $1TNF$ between the electric grid and TG should be avoided, indeed the oscillations are bounded within the electric network. In practice, this damping system has the same function of a capacitor in an electric circuit or an accumulator in a hydraulic circuit, indeed it alternatively accumulates and releases energy in order to keep the power request as constant as possible. The only difference is that this damping system should behaves in this way only at $1TNF$, while it should be transparent to all the other frequencies.

The schematic of the proposed damping system and its control logic are represented in figure 2.5.

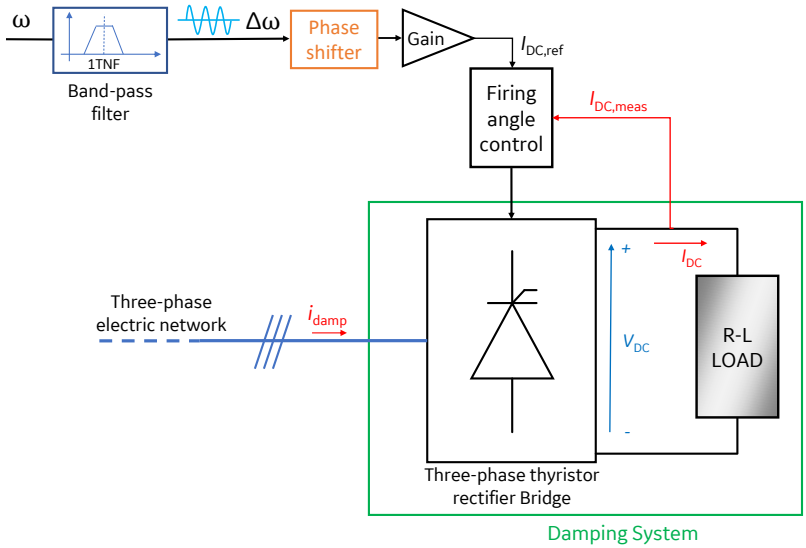

Figure 2.5: Schematic of SSTI damping system.

Note that the firing angle control usually is based on a classical PID controller (*Proportional-Integral-Derivative* controller), and it can be included inside the three-phase thyristor rectifier bridge. Practical guidelines to design and tune a PID controller can be found in many technical manuals or article, e.g. see [4], [48] or [98].

Some additional observations are needed to completely understand the

high level logical diagram in figure 2.5:

- As shown in section 2.2, the electric torque oscillations ΔT_e are strictly related to torsional oscillations $\Delta\omega$, thus ΔT_e and $\Delta\omega$ contain exactly the same information. Since angular speed ω is a measurement always available and quite accurate (see [1] and [2]), it is a reasonable choice to use a band-pass filter to isolate $\Delta\omega$ from ω, and use this information as input of the damper logic.

- the phase shifter and the gain are needed in order to maximise the reduction of electric torque oscillation at $1TNF$. $\Delta\omega$ has to be amplified and delayed in order to compensate the electric oscillations within the network. The gain and the delay can be constant values computed offline during design phase or they can be optimised with online calculations based on adaptive model. $\Delta\omega$ needs to be properly amplified and delayed in order to compensate the differences between the phasors $\boldsymbol{\Delta T}_e(f_n)$ and $\boldsymbol{\Delta\omega}(f_n)$ described in paragraph 2.2.1;

- R-L load should be characterised by a resistance as small as possible in order to minimise the power dissipation and a very large inductance ($L \simeq 1 \div 5mH$). The inductor should be able to accumulate and release energy, exactly as a spring does in a mechanical system. In this way the inductor should filter the fluctuations of energy with frequency nearby 1TNF, thus the mechanical trains, i.e. TGs, should not be excited in correspondence of their first torsional resonance peak;

- the average voltage V_{DC} produced by the three-phase thyristor rectifier bridge can be controlled by modifying the firing angle of the thyristors. In practice, the rectifier bridge does not directly impose the current, but it moves the firing angle modifying the voltage V_{DC} until the current is equal to the desired value. The rectifier bridge is able to follow the reference current $I_{DC,ref}$ only if the frequency of the reference current is definitely lower than the network frequency. Since the objective of this damper system is the mitigation of SSTI oscillations at $1TNF$

(that usually are lower than $10\,Hz$) and the standard electric network frequency is 50 or $60\,Hz$, the above condition is satisfied, therefore the rectifier bridge should be able to follow the reference.

2.5 Simulations and results

SSTI instability has been experienced for a long time and many studies have highlighted that this phenomenon is mainly influenced by the grid size and configuration, the number and the localization of the electrical generators and the features of the power electronic equipment used as input stage and/or to control the large electric loads connected to the grid (e.g. motors, pumps, fans and heaters). Many simulations have been performed exploiting dedicated toolbox available in MATLAB®and Simulink®; in particular the modelling and simulation of the electric grid has been performed in PLECS®[2].

Several configurations have been tested, but all of them can be summarised as shown in figure 2.6, where G_A and G_B are two separated electric generators, Z_A and Z_B are the two isochronous reactances, while $Z_{c,A}$, $Z_{c,B}$, Z_D and Z_L are the line impedances. It is worth noticing that when two or more TG units are running in an isolated system where frequency is not dictated by a prevalent network, isochronous/droop control is the traditional and simplest way to control each train. Only one TG train has to be controlled in isochronous mode, thus this unit is controlled to maintain a constant speed (due to 50 or $60\,Hz$), regardless of the load. The value of the active power supplied to the load can not be set and the machine faces to all load variations; i.e., if an increase in load power demand occurs, GT consequent response is a speed reduction, immediately corrected by the speed controller increasing the gas quantity supplied to the machine. If more TGs operate in parallel, the other units have to be controlled in

[2] PLECS®is a very interesting tool for high-speed simulations of power electronics and thermodynamics that can be easily integrated in MATLAB®and Simulink®environment. More details can be retrieved from the PLECS user manual, available at [75].

droop mode. In droop control mode the speed is not imposed, indeed the power supplied to the load follows the droop load control curve, i.e. a linear curve that describes the connection between the turbine speed variation and the corresponding variation in the load power request. Detailed description of isochronous/droop mode control can be retrieved in many manuals, see e.g. [9], [99], [74] and[44] .

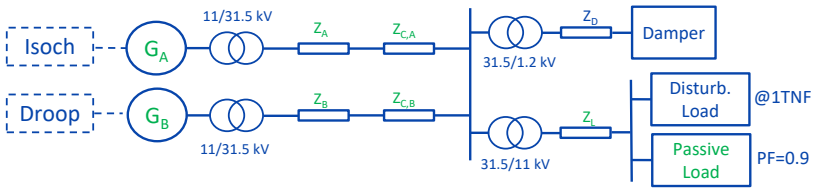

Figure 2.6: Schematic of electric power generation and distribution system.

Note that the SSTI oscillations are imposed by introducing a fake load that absorbs power at $1TNF$; in this way it is simple to activate/deactivate SSTI during the simulation.

As explained previously, different configuration of electrical grid can bring to different risk of incurring in SSTI phenomenon; this is the reason why several network configurations have been simulated and tested. In particular, the set of simulations has been studied aiming to consider different line impedances, critical events such as load steps and different torsional models of TGs. In the following some results that provide general features of SSTI are reported.

Figure 2.7 shows the torsional oscillations of the isochronous GT in three different cases (normalised in pu). In figure 2.7a, the disturbing load and the passive load are inserted at $t = 0\,s$, indeed there is an initial undershoot due to the electric passive load that makes the GT speed decrease. However, in a few seconds the GT governor brings the average speed towards $1\,pu$. Moreover the disturbing load at $1TNF$ induces larger and larger torsional oscillations, and when the damping system is activated ($t = 10\,s$) the oscil-

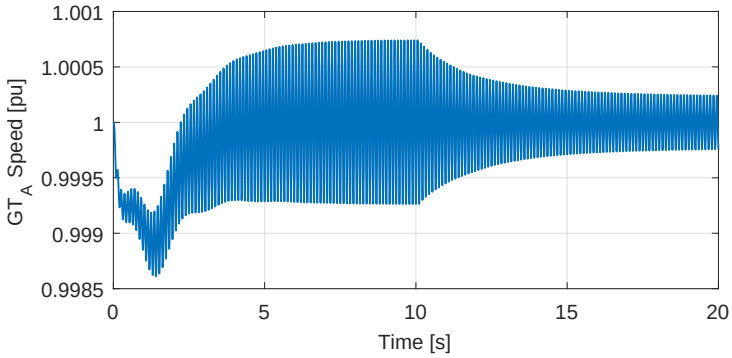

(a) *Damping of torsional oscillations.*

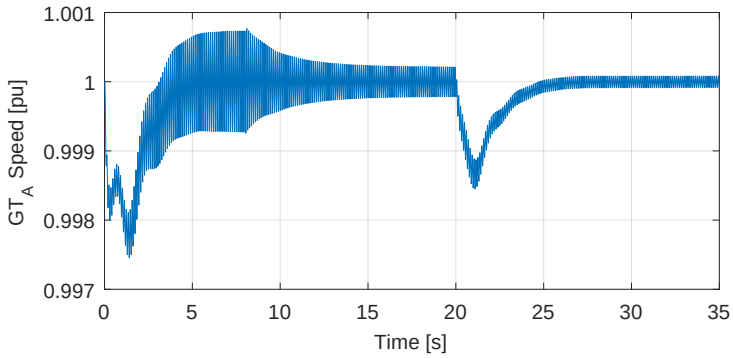

(b) *Damping of torsional oscillations with load step.*

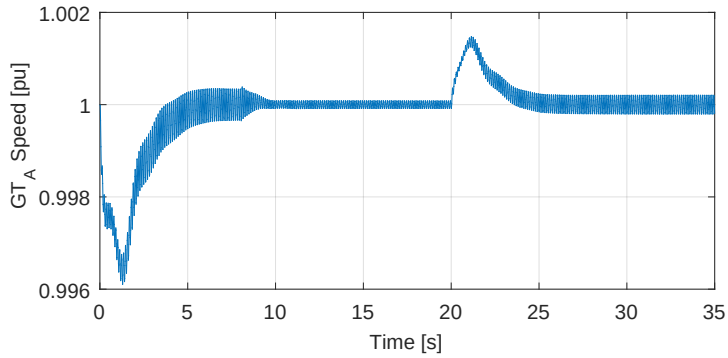

(c) *Damping of torsional oscillations with load rejection.*

Figure 2.7: Simulation results of three examples of torsional oscillations damping.

lation magnitude is $\simeq 7.5\,10^{-4}\,pu$. When the damping system is turned on the oscillation are reduced of $\simeq 60\%$ in about $5\,s$.

This behaviour is approximately equal to what happens in figures 2.7b and 2.7c: besides that, these tests simulate how the system responds to a load step (figure 2.7b) and to a load rejection (figure 2.7c), both of them at $t = 20\,s$. Note that load step indicates that the load gets increased, while load rejection indicates that the load decreases. In addition to the initial undershoot/overshoot due to load changes, it is worth noticing that when the system gets a greater load the oscillations are reduced, while when the system rejects a part of the load the oscillations are intensified. This is a general rule, indeed many researchers has experienced that unloaded electric generation plants are more sensitive to SSTI issues.

Moreover, it has been observed that in very large electric networks it is less frequent to have SSTI; this is due to the fact that in wider electric grids there are more dissipations, thus the disturbances at $1TNF$ (as all the other disturbances) are automatically reduced. Similar reasonings can justify also the fact that generation plants composed of several TGs in parallel (more than 3/4 TGs) are not interested by SSTI, indeed in this case the disturbances at $1TNF$ are distributed between several trains, thus each TG does not receive enough energy at $1TNF$ to trigger SSTI phenomenon, and dangerous torsional oscillations are avoided.

Figure 2.8 shows how the three-phase thyristor rectifier bridge works. As shown in figure 2.8a each phase current (briefly indicated as i_{damp} in figure 2.5) has several discontinuities when the relative thyristor is turned on/off. By controlling the firing angle it is possible to make the DC link current follow the reference current (figure 2.8b). Note that the DC link can only absorb a positive current, and this is the reason why it is necessary to add a constant offset to the reference current.

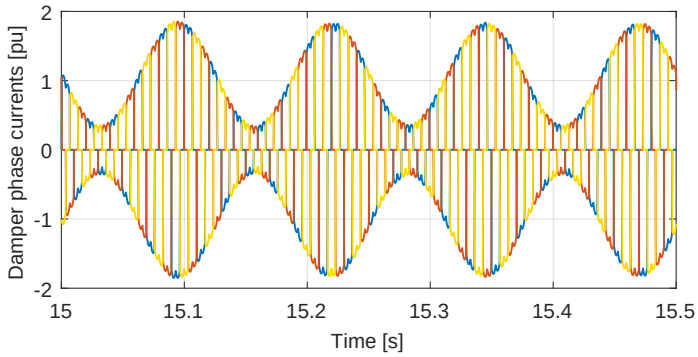

(a) *Damper current absorbed by each three-phase line.*

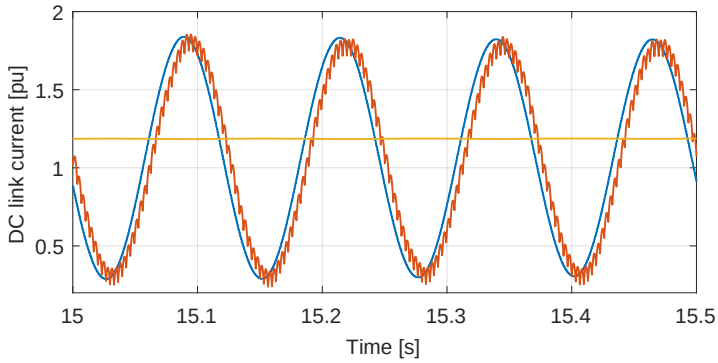

(b) *Current on damper DC link: blue line represents reference current, orange line is the actual current and the yellow one is the RMS value.*

Figure 2.8: Example of damper line currents and DC link current.

From a theoretical point of view thyristors are able to immediately open up or close off the current flow, in practice the switches will be always gradual; this is due to the fact that every electrical circuit is characterised by a certain inductance, thus it is not possible to have discontinuities on current, indeed this would require an infinite voltage peak. This highly non-linear behaviour has to be taken into account in a real power generation plant, indeed a deep analysis to evaluate the total distortion introduced in the network by the damper system should be carried on. In particular each country has

its own regulations (*grid code*) about the maximum THD allowed in a grid, thus the damper system has to be designed considering these legal limits.

The last observation is about the power that needs to be dissipated by the damper system. If the damper were composed of an ideal inductor it would exchange with the network only reactive power: this means that the absorbed power would be a zero-mean power, without any real transfer of energy. On the contrary, the real damper system is characterised by a certain resistance: it should be as small as possible but always greater than the ideal 0Ω.

Theory of electrical engineering (see e.g. [3]) states that the power associated to a current $i(t)$ that flows through an inductor L in series with resistance R is equal to

$$P_{RL}(t) = P_L(t) + P_R(t) = \underbrace{L \cdot \frac{\partial i(t)}{\partial t}}_{V_L} \cdot i(t) + R \cdot i(t)^2. \tag{2.8}$$

By consequence, the energy absorbed by the damper should be equal to

$$E_{RL}(t) = \int_0^t (P_L(t) + P_R(t))\, dt = \frac{1}{2} L i(t)^2 + \int_0^t (R \cdot i(t)^2) dt. \tag{2.9}$$

Equation (2.9) clearly states that the energy diverges in time, thus the system sizing and above all the cooling system has to be designed in order to be able to manage this quantity of energy. Indeed, the cooling system is supposed to be able to dissipate enough energy in order to prevent the damper system from overheating.

2.6 Results analysis and conclusions

As mentioned in the previous sections, SSTI phenomenon is deeply influenced by several features both of mechanical and electrical systems. As a consequence, it is quite hard to provide general rules to quantitatively compute SSTI risk. Each particular site would require a dedicated analysis in order to assess the risk of occurrence of this unstable phenomenon and,

if necessary, to quantify the goodness of a damping system introduced to mitigate the oscillations.

However, simulations have highlighted some SSTI general features and some guidelines that should be taken into consideration during design phase in order to minimise the occurrence of this events. They can be summarised in these points:

i. Larger electric networks (thus larger values of impedances $Z_{C,A}$ and $Z_{C,B}$ referring to figure 2.6) are less compatible with SSTI instability. In very wide electric grid, e.g. a prevalent network, the power of the disturbs that can lead to SSTI is negligible with respect to the network power capacity, and the physical sizes of the grid allow the dissipation or the temporary storage of all the harmonics different from the standard one;

ii. $\Delta\omega$ can be measured either from the isochronous GT or the droop mode controlled GT. Sometimes it can happen that the optimal values for the gain and the phase delay depend on the source of $\Delta\omega$. Nevertheless, the proposed damper logic is effective independently from where $\Delta\omega$ is taken. This means that in an electric generation plant composed of several TGs, the damper system can take the angular speed measurement from any TG, without restrictions. Obviously, the numerical calibration of the damper logic will be connected to the particular choice of the source of $\Delta\omega$;

iii. the most critical situation concerning SSTI phenomenon has been experienced when the electrical power request is very small. Once again, this behaviour can be explained considering the relative weight of disturbing load with respect to the total power request;

iv. in some simulations two different TGs (i.e. with different mechanical size and TNFs) have been considered. The results have highlighted that when the damping system mitigates the torsional oscillations induced in one TG, the other one is not affected by the damper action.

Since very different TNFs means that the two TGs are sensitive to very distant frequencies, this result is reasonable; however, it is very important to be sure that the damper system, in addition to mitigate SSTI, does not introduce any negative effect within the system;

v. load step and load rejection events do not represent critical events by themselves. However, as described in bullet (iii), it has to be considered that SSTI criticality changes with the total power request, thus during load rejection events the system moves towards a configuration characterised by a major SSTI risk.

Chapter 3

Gas Turbine Modelling and Model-Based Estimation

Many different types of GTs have been developed in the past years and they can be broadly classified as single-shaft GT, mainly generator drive application, or two-shaft GT, mainly mechanical drive application. In this chapter the characterisation and the modelling of a particular two-shaft GT will be addressed; first of all a static a-priori model has been proposed and it has been trained with a massive dataset, then all the measurements and equations have been merged within a Kalman filter. Finally, the quality of the model has been evaluated also by exploiting field data and conclusions have been drawn.

3.1 Gas turbine general description

The first operating gas turbine was proposed in the beginning of twentieth century and it had a very low thermal efficiency. In a few decades the gas turbines technology has been deeply enhanced and they have been introduced in a wide range of practical and industrial applications, such as:

- *electric power generation*: a gas turbine is directly connected to an

electric generator running at constant speed. The speed depends on the number of magnetic poles of the generator and the standard electric grid frequency, that can be 50 or 60 Hz. Sometimes a gearbox is required to scale the GT speed to the generator speed;

- *compressor drive application*: in this case GT can be designed in order to have the same rotational speed of the compressor, thus gearbox is not always strictly required. Compressor rotating speed is usually asked to vary within a certain operating range, thus the GT that drives the compressor has to be designed in order to be able to adapt its own rotational speed;

- *aircraft propulsion*: the basic development in this field took place for high-speed military aircrafts. In this case the engine is asked only to produce enough power to drive the compressor, then the gas leaving the turbine at high pressure and temperature is expanded to atmospheric pressure in a propelling nozzle to produce a high velocity jet. Only in the early 1950s GTs started to be used in civil aircraft applications;

- *marine and land transportation*: GTs have been used as prime mover for ships, trains and trucks[1]. Usually GTs for these applications are derived from aircraft engines and for this reason they are often referred to as aero-derivative GTs. Aero-derivative GTs are generally lighter weight, physically smaller and have a better partial load performance with respect to industrial GTs (which are usually referred to as heavy-duty GTs), but they are characterised by more frequent maintenance intervals.

When GTs are required to operate at a fixed speed and fixed load the single-shaft configuration is the most suitable (figure 3.1), indeed the engine has not to be flexible and ready to changes of rotational speed.

[1]Due to several technical reasons, GTs did not provide a significant contribution to land transportation; current proposals would use GTs to generate electricity with separate electric motors on the driving wheels.

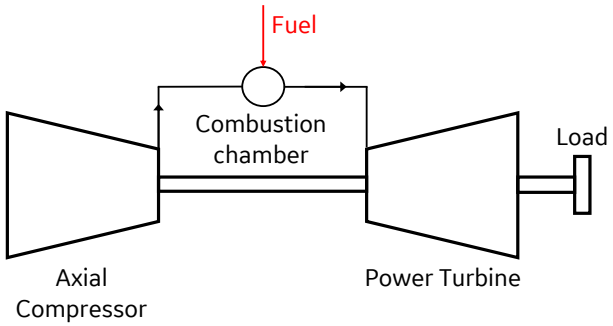

Figure 3.1: Single-shaft GT schematic.

On the contrary, when flexibility in operation is of great importance, e.g. when driving a variable speed load such as a centrifugal compressor, the use of a mechanically free power turbine is appreciable. In this two-shaft configuration (figure 3.2) the *High-Pressure Turbine* (HPT) drives the compressor and the combination acts as a *Gas Generator* (GG) for the *Low-Pressure Turbine* (LPT). LPT is the free power turbine which is aerodynamically but not mechanically coupled to HPT. Aircraft engine may be used as gas generator for driving an electric generator or a mechanical load, indeed it is just enough to make exhaust gas expand through a power turbine such as LPT rather than the original exhaust nozzle.

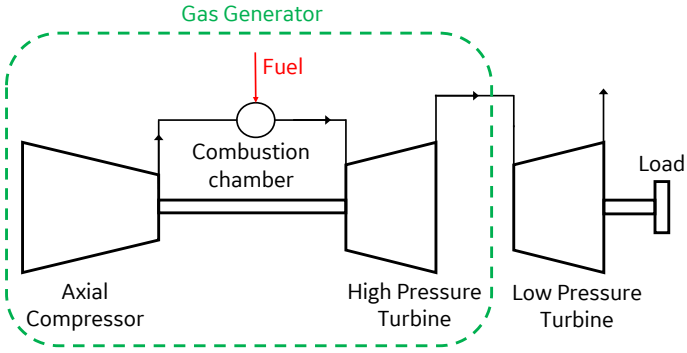

Figure 3.2: Two-shaft GT with separated power turbine schematic.

Figures 3.3 shows an example of two-shaft GT that has been heavily installed worldwide both in mechanical drive and power generation applications.

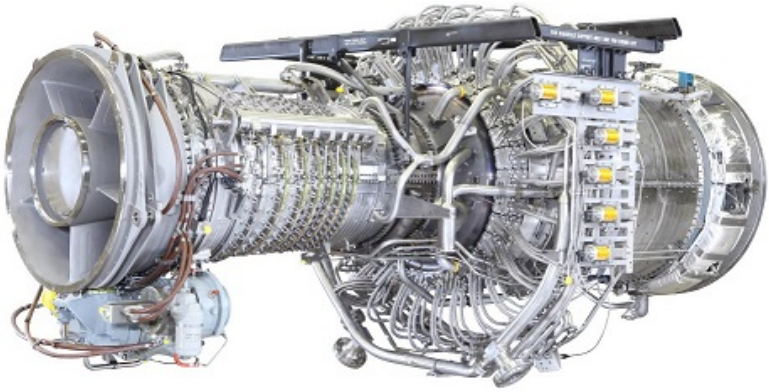

Figure 3.3: GE LM2500+G4, a two-shaft aero-derivative GT. This GT belongs to GE LM series, where LM states for *Land* & *Marine*. Courtesy of BHGE (source `www.bhge.com`).

On the other hand, figure 3.4 shows an example of single-shaft GT, mainly used in power generation plants.

(a) *Single-shaft gas tubine, first view.*

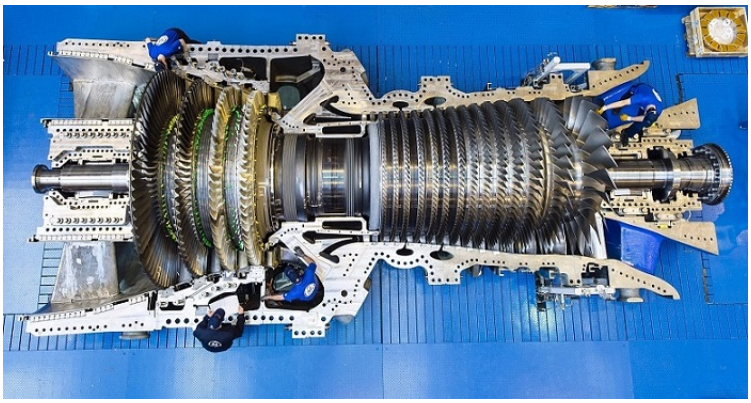

(b) *Single-shaft gas tubine, second view.*

Figure 3.4: Two different views of a single-shaft GT. Courtesy of BHGE (source `www.ge.com`).

3.1.1 GE LM2500 overview

The LM2500 gas turbines are simple cycle, two-shaft, high-performance engines. They derived from GE $TF39$ and $CF6-6$ aircraft engines, and they consist of a gas generator and a power turbine. These gas turbines are single rotor GTs which are aerodynamically coupled with a power turbine. Power turbine operates at a nominal speed of $3600\,rpm$, making it ideal for $60\,Hz$ electric generation service. Alternatively, it can also operate efficiently over a cubic load curve for mechanical drive applications.

Depending on the model, AC is composed of 16 or 17 stages, while the power turbine can have 2 or 6 stages. AC does not have *Inlet Guide Vane* (IGV), but it has the *Variable Stator Vane* (VSV), i.e. a particular system that modifies the geometry of the first AC stages in order to allow it to properly work at any load and speed. LM2500 GTs are usually suitable for two types of power turbines:

1. a six-stage low speed power turbine, with a nominal speed of $3600\,rpm$;
2. a two-stage high speed power turbine, with a nominal speed of $6100\,rpm$ (this power turbine is usually preferred in mechanical drive applications).

Typical power of these GTs is between $25\,MW$ and $33\,MW$.

There are three GTs that belongs to LM2500 family, whose peculiarities are summarised in table 3.1:

i. LM2500 (see [29]);
ii. LM2500+ (see [30]);
iii. LM2500+G4 (see [31]).

	LM2500	**LM2500+**	**LM2500+G4**
Max power $[kW]$	25060	30200	35320
Fuel cons. $\left[\frac{g}{kW \cdot h}\right]$	227	215	214
Heat rate $\left[\frac{kJ}{kW \cdot h}\right]$	9705	9227	9150
Exhaust gas flow $[kg/s]$	70.5	85.9	93
Exhaust gas temp. $[K]$	839	791	822
Turbine speed $[rpm]$	3600	3600	3600
Thermal efficiency [ ]	36 %	38 %	39 %
Weight $[kg]$	4700	5250	5250

Table 3.1: LM2500 GT family characteristics.

Moreover, depending on combustion chamber type, LM2500 GTs can be classified as *Singular Annular Chamber* (SAC), where there are not limitations on NOx emissions, or *Dry Low Emission* (DLE), where NOx emissions are limited to 25 ppm.

This thesis work will focus on a particular two-shaft aero-derivative GT which belongs to LM2500 family, i.e. LM2500+G4 DLE.

3.2 GE LM2500+G4 DLE detailed modelling based on NPSS

Figure 3.5 depicts in a qualitative temperature-entropy diagram the difference between the ideal and the real thermodynamic cycle of a single-shaft GT. This thermodynamic cycle is the well-known Brayton cycle. The real cycle tends to move away from the ideal one because of many non-idealities such as dissipations, frictions, not ideal combustion, engine ageing or degradation, mechanical losses and so on.

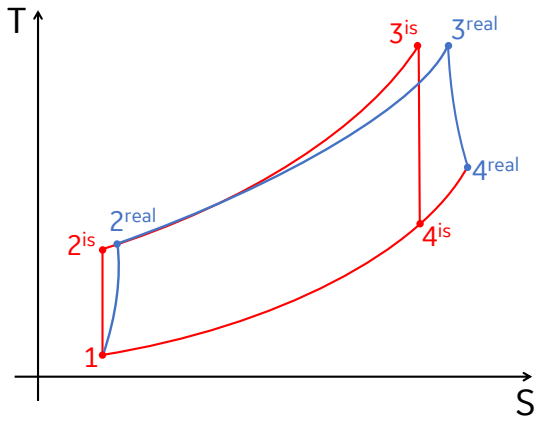

Figure 3.5: Schematic representation of ideal/real Brayton cycle of a single-shaft GT.

Since every GT model has its own peculiarities, in the past decades many efforts have been made to develop computational methods for the definition and the resolution of the very complex non-linear differential equations that aerodynamically, mechanically and thermodynamically describe the GT engine. *National Aeronautics and Space Administration* (NASA) has introduced the so-called *Numerical Propulsion System Simulation* (NPSS), i.e. an object-oriented, multi-physics, engineering design and simulation environment. There are many detailed technical reports about NPSS, see e.g.

[62], [49] and [20]. NPSS is a full engine multidisciplinary simulation tool developed for aerospace industry but also used in oil and gas power industry, indeed it provides an environment for the analysis and the design of aircraft propulsion systems, rocket cycles and many other thermodynamic processes. Actually, NPSS implements and solves all the differential equations that describe in a detailed and rigorous way the system; for this reason, in this work NPSS model will be considered as reference.

NPSS is currently managed by a consortium including research institutes and industrial members. Different licensing scheme are available both for academic and commercial use. The NPSS software exploited in this work has been made available by *Nuovo Pignone - Baker Hughes, a GE Company* and it provides expected values about the GE LM2500+G4 DLE main physical quantities.

In order to adapt the average engine model to real conditions it contains six corrective parameters (CPs) useful to modify the thermodynamic and flow efficiency respectively of AC, HPT and LPT. Four CPs are relative to thermodynamic and flow efficiency of AC and HPT, while the other two CPs are relative to thermodynamic and flow efficiency of LPT. In the next sections some mathematical models regarding each section of GE LM2500+G4 DLE (presented in paragraph 3.1.1) will be introduced: these models have been both tuned and validated using NPSS model as a reference. In particular, the datasets used to tune/validate mathematical models are listed below:

i. *nominal NPSS dataset*: this dataset has been obtained using NPSS by exploring all the feasible operating conditions (different fuel compositions, delivered power and inlet conditions), always maintaining the six CPs equal to 1. This dataset has been used during validation phase in order to figure out the nominal behaviour of the machine;

ii. *GG extended NPSS dataset*: this dataset has been obtained using NPSS by exploring all the GG feasible operating conditions; each single CP relative to GG has been moved from 0.98 to 1.02 with step

of 0.01 (i.e., each operating condition has been simulated in $5^4 = 625$ different configurations of CPs). On the contrary the two CPs relative to LPT have always been kept equal to 1, in turn this dataset ranges within all the possible configurations of the gas generator maintaining the nominal model concerning the LPT. This dataset has been used to validate the proposed models in all the possible configurations of the GG. The reason why this dataset is significant is that the GG of this gas turbine can be coupled with different type of LPT, thus it would be very useful to validate the proposed model with respect to GG variations and then introduce the LPT as an additive model.

iii. *full extended NPSS dataset*: this dataset has been obtained using NPSS by exploring all the feasible operating conditions, and moving each single CP from 0.98 to 1.02 with step of 0.01. This means that each operating condition has been simulated in $5^6 = 15625$ different configurations of CPs. This massive dataset has been used to validate the proposed models in all the possible configurations. Figures 3.6 and 3.7, referring to the nomenclature reported in table 3.2, show the percentage variations introduced by CPs changes on each quantity with respect to *nominal NPSS dataset*. It is worth noticing that *GG extended NPSS dataset* is a subset of *full extended NPSS dataset*, indeed the former is completely included within the latter;

iv. *real trend dataset*: some datasets taken from existing LM2500+G4 DLE running sites have been used to validate the proposed models. Obviously these datasets are very important because they allow the validation with respect to real data; however these trends contains only quantity that can be measured by available sensors, thus it is not trivial to use these datasets to validate the model.

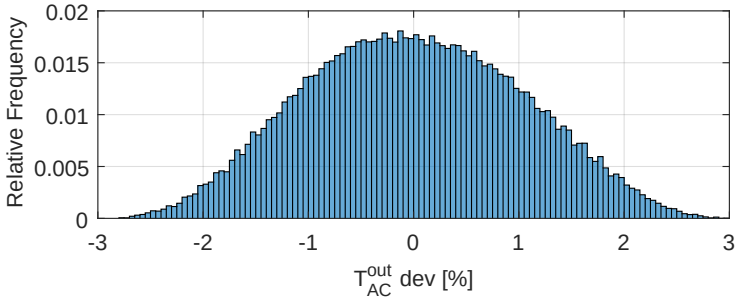

(a) T^{out}_{AC} *percentage deviation.*

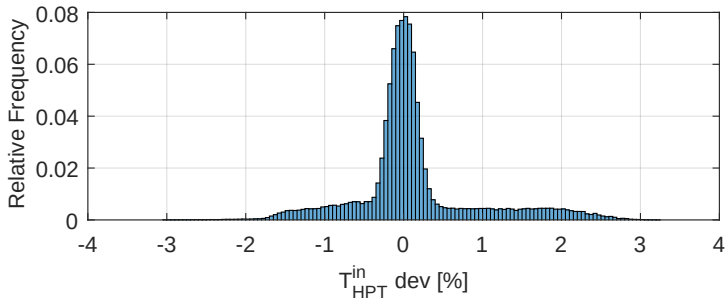

(b) T^{in}_{HPT} *percentage deviation.*

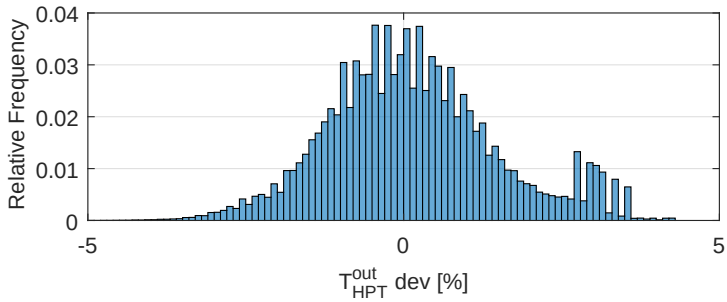

(c) T^{out}_{HPT} *percentage deviation.*

Figure 3.6: NPSS temperatures percentage deviation: *full extended NPSS dataset* versus *nominal NPSS dataset.*

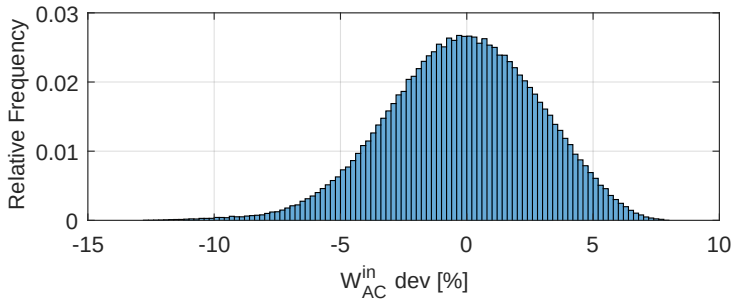

(a) W^{in}_{AC} *percentage deviation.*

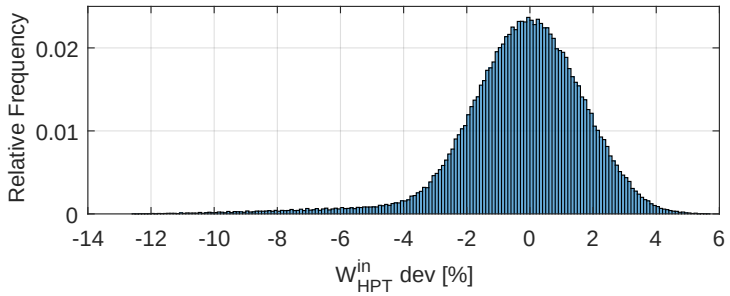

(b) W^{in}_{HPT} *percentage deviation.*

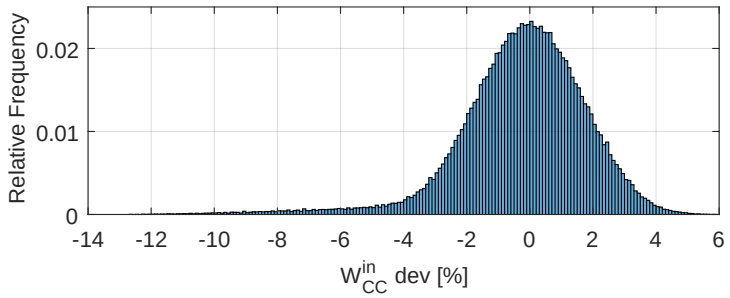

(c) W^{in}_{CC} *percentage deviation.*

Figure 3.7: NPSS flows percentage deviation: *full extended NPSS dataset* versus *nominal NPSS dataset.*

3.3 A-priori static model of GE LM2500+G4 DLE

In parallel with the technical improvement of GTs, many researchers have understood the importance of developing a mathematical model able to describe how the system acts in each operating point. Such a model could be very useful to estimate quantities that can not be directly measured by transducers, to provide validation and redundancy of quantities measured by physical sensors, or to enhance control law that could be based not only on the direct measurements but also on the knowledge of the plant internal model that describes from a mathematical point of view the physical laws on which the system is based on. GTs operating principles and theory has been widely studied and many handbooks and technical manuals about this topic have been written (see e.g. [24], [19], [72], [16], [73], [87] and [32]). Besides, in literature there are many examples of GTs models based on thermodynamic relationships, both for aero-derivative and heavy duty GTs (see e.g. [40], [106], [53] and [23]). A common issue in GTs modelling, as shown in [108], is that the system is very complex and highly non-linear, thus it is difficult to develop a general method with validity extended to all the possible operating conditions. For instance, in [55] at first a GT model is implemented in MATLAB®and Simulink®, then the model is tested and validated in many different operating and environmental conditions. In the last years GT control and identification through neural networks has been proposed (e.g. [107] and [54]). Also GT MPC (*Model Predictive Control*), although it is not widely used in industrial applications, has been addressed by many researchers (see e.g. [80], [17] and [50]).

In this chapter an a-priori static model of the GE LM2500+G4 DLE will be introduced. Details of this particular aero-derivative GT are described in paragraph 3.1.1, while figure 3.3 is a picture of this GT. Referring to the nomenclature reported in table 3.2, and considering the usually available measurements in typical oil and gas applications, the inputs and outputs lists for the overall static model are:

- **Inputs**: T_{AC}^{in}, p_{AC}^{in}, T_{AC}^{out}, p_{AC}^{out}, LHV, T_{fuel}, $c_{p,fuel}$, T_{HPT}^{out}, p_{HPT}^{out};
- **Outputs**: W_{AC}^{in}, T_{AC}^{out}, W_{CC}^{in}, p_{HPT}^{in}, T_{HPT}^{in}, W_{HPT}^{in}.

Note that, concerning the static model, T_{AC}^{in} can be considered both as input and output at the same time. This is due to the fact that in correspondence of the last AC section thermocouples are always inserted to directly measure the AC discharge temperature, but this quantity can also be estimated regardless its measurement by the static model that will be introduced in paragraph 3.3.1. Furthermore, as will be explained in the next paragraphs, flows can be estimated in two different ways. This features about T_{AC}^{in} and the flows through the GT will be exploited to improve the estimation accuracy and to enhance the model performance.

Symbol	Unit	Definition
p_{AC}^{in}	$[kPa]$	AC inlet pressure
T_{AC}^{in}	$[K]$	AC inlet temperature
p_{AC}^{out}	$[kPa]$	AC outlet pressure
T_{AC}^{out}	$[K]$	AC outlet temperature
W_{AC}^{in}	$[kg \cdot s^{-1}]$	AC inlet airflow
W_{bleed}	$[kg \cdot s^{-1}]$	Bleed airflow
W_{CC}^{in}	$[kg \cdot s^{-1}]$	Combustion chamber inlet airflow
W_{fuel}	$[kg \cdot s^{-1}]$	Total fuel flow
W_{HPT}^{in}	$[kg \cdot s^{-1}]$	HPT inlet airflow
W_{HPT}^{out}	$[kg \cdot s^{-1}]$	HPT outlet airflow
c_p, c_v	$[J \cdot (K \cdot kg)^{-1}]$	Isobaric/Isochor heat capacity
γ	[ ]	Isobaric/Isochor heat capacity ratio
T_{HPT}^{in}	$[K]$	First HPT section temperature
p_{HPT}^{in}	$[kPa]$	First HPT section pressure

T_{HPT}^{out}	$[K]$	Last HPT section temperature
p_{HPT}^{out}	$[kPa]$	Last HPT section pressure
LHV	$[kJ \cdot kg^{-1}]$	Fuel lower heating value
N_{HPT}	$[rpm]$	HPT rotational speed
N_{LPT}	$[rpm]$	LPT rotational speed
η_{AC}^{is}	[ ]	Isentropic AC efficiency
η_{HPT}^{is}	[ ]	Isentropic HPT efficiency
η_{CC}	[ ]	Combustion efficiency
T_{fuel}	$[K]$	Fuel temperature
J_{GG}	$[kg \cdot m^2]$	GG inertia

Table 3.2: GE LM2500+G4 DLE main quantities nomenclature

3.3.1 Axial compressor model

The first mathematical model able to describe the behaviour of an axial compressor was introduced by Moore and Greitzer (see [66] and [67]). In the past decades many researchers have enhanced this model (see e.g. [13], [95], [63] [34]); this is a very complete model and it allows the simulation of AC behaviour even when it operates near instability regions (i.e. stall, surge or choking). However, *Moore-Greitzer* model requires an accurate identification of many machine-dependent parameters, thus it is particularly linked to the specific compressor under analysis. In this work an alternative model is used, indeed AC modelling is split in two separated modules: the first one provides a calculation of the flow through the inlet stage of the AC, while the second addresses the AC discharge temperature calculation.

Table 3.3 shows the inputs and the outputs of the proposed AC a-priori static model.

Inputs	Outputs
T_{AC}^{in}	W_{AC}^{in}
p_{AC}^{in}	T_{AC}^{out}
p_{AC}^{out}	

Table 3.3: Inputs and outputs of the proposed AC model.

Axial compressor inlet airflow

The *Law of the Ellipse*, which is usually referred to as *Stodola's Law*, provides a simple method for calculating the airflow through a multi-stage AC (more details can be retrieved in [39] and [37]). Obviously this is a highly non-linear phenomenon and it can describe the AC behaviour only within nominal operating range, thus it is not suitable to model the AC flow when stall, surge or choking occur. Equation (3.1) is an approximation of the *Law of the Ellipse* which can be exploited to compute AC inlet flow

$$W_{AC}^{in} = c_{AC} \cdot \frac{p_{AC}^{in}}{\sqrt{T_{AC}^{in}}} \cdot \sqrt{1 - \left(\frac{p_{AC}^{in}}{p_{AC}^{out}}\right)^2}, \tag{3.1}$$

where c_{AC} is a variable coefficient that assumes different values in different operating conditions. Several NPSS simulations have been performed to find out a map that describes how it changes when the inlet AC conditions and the GG speed change. In particular *nominal NPSS dataset* has been exploited, and it has underlined that inlet pressure p_{AC}^{in} does not affect too much this coefficient, thus the map showed in figure 3.8 is a family of curves that describes how c_{AC} changes in function of T_{AC}^{in} and N_{HPT}.

Note that one of the reason why coefficient C_{AC} is not constant is that the AC under analysis can change its geometry thanks to VSV (*Variable Stator Vanes*), whose angle is scheduled in function of N_{HPT}, p_{AC}^{in} and T_{AC}^{in}. Since VSV are controlled in open-loop mode and their position depends only on N_{HPT}, p_{AC}^{in} and T_{AC}^{in}, it is possible to include their effects on the global system inside the static model; in this way, VSV modelling is not required,

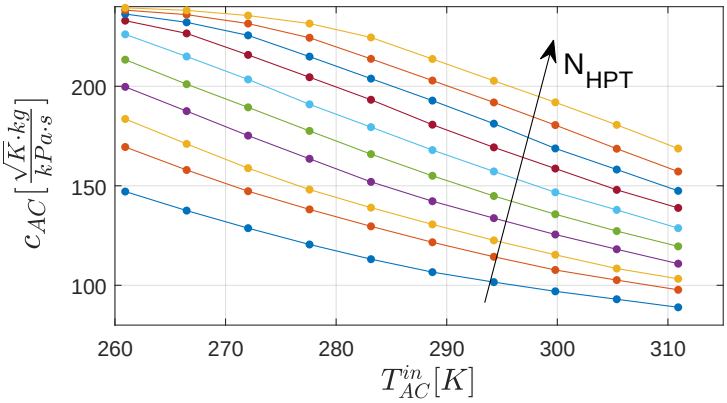

Figure 3.8: AC flow coefficient map.

indeed it is automatically considered by C_{AC} map.

Axial compressor discharge temperature

Air temperature obviously increases between AC suction and discharge. Considering an ideal isentropic compression, the relation between suction and discharge thermodynamic properties is given by equation (3.2).

$$\frac{T^{out}_{AC,is}}{T^{in}_{AC,is}} = \left(\frac{p^{out}_{AC}}{p^{in}_{AC}}\right)^{\frac{\gamma_{air}-1}{\gamma_{air}}} \tag{3.2}$$

where γ_{air} is defined as the isobaric and isochor heat capacity ratio relative to air (thus it is known and almost constant) and the subscript "is" states that the quantity is referred to an ideal isentropic transformation. The previous equation can be generalised introducing the isentropic efficiency $\eta_{AC,is}$. As shown in figure 3.5, the temperature at the end of AC in real cycle is greater than the temperature at the same section in the ideal cycle. In turn, it is possible to define the isentropic AC efficiency $\eta_{AC,is}$ as

$$\eta_{AC,is} = \frac{T^{out}_{AC,is} - T^{in}_{AC}}{T^{out}_{AC} - T^{in}_{AC}}. \tag{3.3}$$

By merging and manipulating equations (3.2) and (3.3), it is immediate to obtain

$$\frac{T_{AC}^{out}}{T_{AC}^{in}} = 1 + \frac{1}{\eta_{AC,is}} \left[\left(\frac{p_{AC}^{out}}{p_{AC}^{in}} \right)^{\frac{\gamma_{air}-1}{\gamma_{air}}} - 1 \right]. \tag{3.4}$$

Starting from known inlet conditions, equation (3.4) describes the relationship between temperature and pressure at AC discharge. This means that p_{AC}^{out} and T_{AC}^{out} are strictly connected, thus it is sufficient to measure only one of them to compute the other one.

Isentropic efficiency $\eta_{AC,is}$ is not constant. Even without considering efficiency degradation due to ageing, it is necessary to know how it changes in different operating conditions. Once again, *nominal NPSS dataset* has been exploited in order to find out a map that describes how it varies with T_{AC}^{in} and N_{HPT}. As seen for c_{AC}, inlet pressure does not affect this coefficient, thus the map can be simplified (figure 3.9).

Note that this map takes as input the corrected axial compressor airflow $W_{AC,c}^{in}$, defined as

$$W_{AC,c}^{in} = W_{AC}^{in} \cdot \sqrt{\frac{T_{AC,nom}^{in}}{T_{AC}^{in}}} \cdot \frac{p_{AC}^{in}}{p_{AC,nom}^{in}},$$

where $T_{AC,nom}^{in}$ and $p_{AC,nom}^{in}$ are the ambient nominal value of temperature and pressure, respectively equal to $288.15\,K$ and $1013\,kPa$. Corrected airflow is a very useful normalisation that allows to consider all the possible combinations of flow, temperature and pressure in a single quantity.

3.3.2 Combustion chamber model

In literature there are many examples of combustion models that were introduced to describe the gas-dynamics and the combustion process of particular GTs (see e.g. [7], [101] and [82]). Other models, such as the ones proposed in [64], [18], [100] and [8], are aimed to control combustion instabilities (e.g. acoustic pressure oscillations) and harmful emissions (mainly NO_x and CO emissions). These models are very specific and they have been introduced

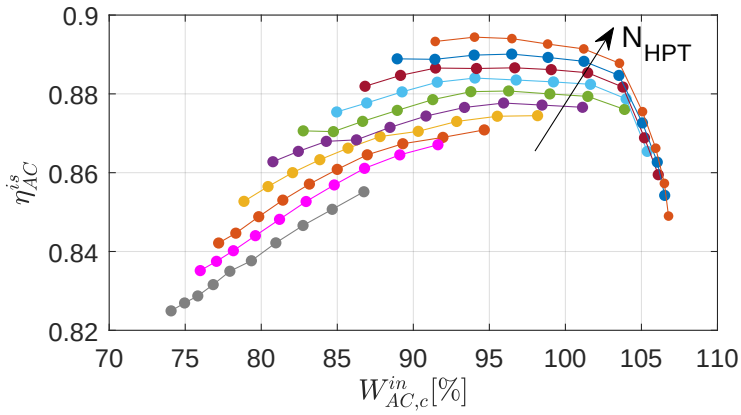

Figure 3.9: AC isentropic efficiency map.

to face certain well defined issues connected to combustion; the objective of this work is to achieve a global energetic characterisation of the combustion chamber, thus it is not required a detailed model able to describe the thermodynamic and aerodynamic behaviour of the whole system.

Table 3.4 shows the inputs and the outputs of the combustion chamber model considered in this work. Fuel isobaric heat capacity needs to be known in order to produce an energy balance based on real fuel chemical properties. Unlike what happens in AC, the flow through the combustion chamber is not composed only by air, indeed it is a mixture; as shown in [14], isobaric heat capacity of a mixture is equal to a linear combination of the single isobaric heat capacities, weighted by the mole fractions of each gas.

Combustion chamber airflow

In the particular aero-derivative gas turbine under analysis, before entering the combustion chamber there is a bleed valve that is used as actuator to control the GT. Thanks to this valve it is possible to avoid GT unstable behaviour, indeed it can move the AC operating point away from surge region of the characteristic compressor map (see e.g. figure 1.4). Clearly

Inputs	Outputs
W_{AC}^{in}	W_{CC}^{in}
p_{AC}^{out}	p_{HPT}^{in}
T_{AC}^{out}	T_{HPT}^{in}
LHV	
T_{fuel}	
$c_{p,fuel}$	

Table 3.4: Inputs and outputs of the proposed combustion chamber model.

this kind of control safeguards integrity of the equipment, but it wastes energy, indeed a part of high temperature and pressure compressed air is blown out. In practice, combustion chamber inlet airflow W_{CC}^{in} can be easily computed by subtracting the total bled air from the AC inlet airflow.

Combustion chamber pressure drop

Because of non-idealities, there is a pressure drop between the first and the last stage of combustion chamber. This is due to frictions, dissipations and turbulent flows. In first approximation the combustion chamber can be considered as an orifice, thus this pressure drop can be evaluated taking into account theory presented in section 1.1. The mass flow through an orifice can be described by equation (1.1). Considering the perfect gas law $\rho = p/RT$, it is easy to develop equation (1.1) and obtain the relationship

$$\Delta p_{CC} = p_{AC}^{out} - p_{HPT}^{in} \simeq k_{p,drop} \cdot \frac{{W_{CC}^{in}}^2 \cdot T_{AC}^{out}}{p_{AC}^{out}}. \tag{3.5}$$

Once again, the coefficient $k_{p,drop}$ is computed thanks to a map shown in figure 3.10.

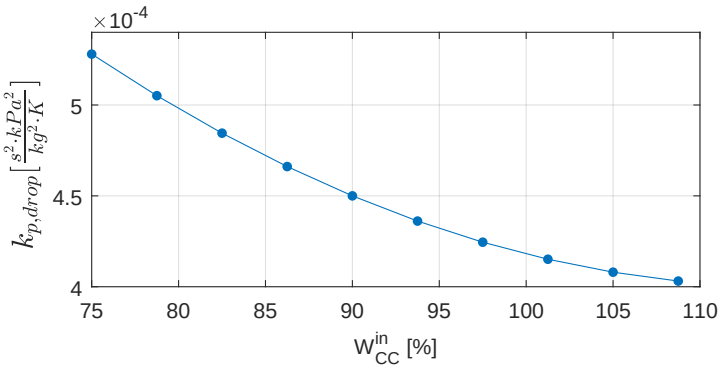

Figure 3.10: $k_{p,drop}$ map.

Combustion efficiency

From a thermodynamic point of view what happens during the combustion can be seen as an energy exchange between the fuel and the total flow through the combustion chamber. The chemical energy stored in the fuel is totally described by LHV (*Lower Heating Value*), which expresses the energy released by the unit mass of fuel after a complete combustion. In turn, ideal power introduced in the system thanks to the fuel is equal to

$$P_{ideal} = LHV \cdot W_{fuel}. \tag{3.6}$$

The previous equation holds the true only in the ideal case. Real power transferred from fuel to the system is lower than P_{ideal}, and this is mainly due to turbulence, frictions and mixing. This phenomenon can be described introducing the combustion efficiency η_{CC}

$$P_{real} = \eta_{CC} \cdot LHV \cdot W_{fuel}. \tag{3.7}$$

This efficiency is characterised by a map similar to the one showed in figure 3.9. Considering the air and fuel isobaric specific heat capacity (respectively $c_{p,air}$ and $c_{p,fuel}$), the power balance can be expressed as follows

$$\eta_{CC} \cdot LHV \cdot W_{fuel} = W_{CC}^{in} \cdot (T_{HPT}^{in} - T_{AC}^{out}) \cdot c_{p,air} + \\ + W_{fuel} \cdot (T_{HPT}^{in} - T_{fuel}) \cdot c_{p,fuel} \tag{3.8}$$

Equation (3.8) considers air and fuel as two separated systems that gain energy. By manipulating equation (3.8) it is immediate to find out a relationship to calculate the temperature T_{HPT}^{in}

$$T_{HPT}^{in} = \frac{LHV \cdot \eta_{CC} + T_{fuel} \cdot c_{p,fuel} + T_{AC}^{out} \cdot AFR \cdot c_{p,air}}{c_{p,air} \cdot AFR + c_{p,fuel}}, \tag{3.9}$$

where AFR (*Air-to-Fuel Ratio*) is defined as

$$AFR = \frac{W_{CC}^{in}}{W_{fuel}}.$$

Note that introducing the assumption $T_{AC}^{out} = T_{fuel}$ equation (3.9) can be drastically simplified

$$T_{HPT}^{in} = T_{AC}^{out} + \frac{LHV \cdot \eta_{CC}}{c_{p,gas} \cdot [1 + AFR]}. \tag{3.10}$$

Where $c_{p,gas}$, as showed in [14], is the weighted sum of $c_{p,air}$ and $c_{p,fuel}$

$$c_{p,gas} = \frac{W_{fuel} \cdot c_{p,fuel} + W_{CC}^{in} \cdot c_{p,air}}{W_{fuel} + W_{CC}^{in}}.$$

The assumption $T_{AC}^{out} = T_{fuel}$ is unrealistic, however equations (3.9) and (3.10) usually return very similar values: this is due to the fact that $W_{CC}^{in} \gg W_{fuel}$, thus the relative weight of T_{fuel} is negligible with respect to the relative weight of T_{AC}^{out}.

3.3.3 High Pressure Turbine model

From a thermodynamic point of view AC and HPT are very similar: the former compresses air, the latter expands combusted gases. Thus, it is reasonable to compute HPT inlet airflow by introducing an equation very similar to (3.1)

$$W_{HPT}^{in} = c_{HPT} \cdot \frac{p_{HPT}^{in}}{\sqrt{T_{HPT}^{in}}} \cdot \sqrt{1 - \left(\frac{p_{HPT}^{out}}{p_{HPT}^{in}}\right)^2}. \tag{3.11}$$

As done for AC, even concerning HPT it is possible to define an isentropic efficiency

$$\eta_{HPT,is} = \frac{T^{in}_{HPT} - T^{out}_{HPT}}{T^{in}_{HPT} - T^{out}_{HPT,is}}. \tag{3.12}$$

Equation (3.2) can be written also regarding HPT

$$\frac{T^{out}_{HPT,is}}{T^{in}_{HPT,is}} = \left(\frac{p^{out}_{HPT}}{p^{in}_{HPT}}\right)^{\frac{\gamma_{gas}-1}{\gamma_{gas}}}. \tag{3.13}$$

Merging equations (3.12) and (3.13) it comes out

$$\frac{T^{out}_{HPT}}{T^{in}_{HPT}} = 1 - \eta_{HPT,is}\left[1 - \left(\frac{p^{out}_{HPT}}{p^{in}_{HPT}}\right)^{\frac{\gamma_{gas}-1}{\gamma_{gas}}}\right]. \tag{3.14}$$

Inputs and outputs of a-priori static HPT model are summarised in table 3.5.

Inputs	**Outputs**
T^{out}_{HPT}	W^{in}_{HPT}
p^{in}_{HPT}	T^{in}_{HPT}
p^{out}_{HPT}	
γ_{gas}	

Table 3.5: Inputs and outputs of the proposed HPT model.

It is important notice that equations (3.14) and (3.9) are two independent methods to calculate T^{in}_{HPT}: in order to discern between these two calculations, T^{in}_{HPT} computed exploiting equation (3.14) will be referred to as *backward*, while the one derived from equation (3.9) as *forward*.

3.4 GE LM2500+G4 DLE: Kalman Filter-based model

Simulations have shown that the a-priori static model introduced in section 3.3 is able to match and reproduce the *nominal NPSS dataset* (i.e. NPSS dataset relative to CPs equal to 1). This is not a surprising result, indeed this model has been tuned exploiting *nominal NPSS dataset*. On the other hand, for the same reason, a-priori static model leads to significant errors with *GG extended NPSS dataset* and *full extended NPSS dataset*, and above all with *real trend dataset*, where non-idealities of real plants prevent it from providing correct estimations of GT quantities. By definition, a-priori static model can not adapt itself to match a dataset that does not fit nominal NPSS expected calculations. By way of example, figure 3.11 shows the percentage error of the a-priori static estimation of T^{in}_{HPT} with respect to *full extended NPSS dataset*.

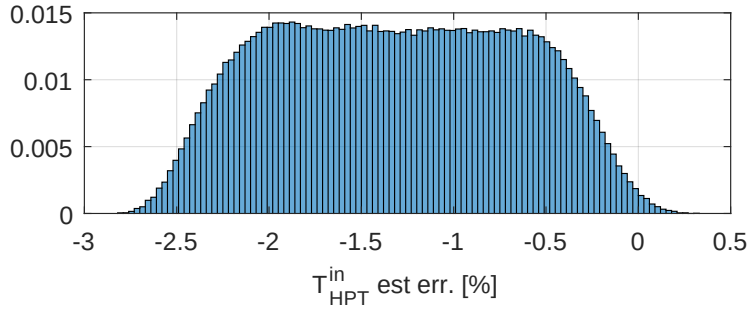

Figure 3.11: A-priori static T^{in}_{HPT} percentage estimation error with respect to *full extended NPSS dataset*.

Comparing figure 3.11 and 3.6b it is clear that the error of the a-priori static estimation is much greater than the variability introduced by the CPs, thus the a-priori static model is not suitable to estimate the quantity of a system that is different from the nominal one.

Even if this first a-priori static model is not suitable as online GT estima-

tion system, it is a good starting point to develop a more general GT model, capable of catching potential deviation of the real system with respect to the nominal one. A-priori static GT model is strongly based on physical relationships, thus it is just necessary to correct the first estimations provided by this model trying to move the mathematical model towards real data.

Kalman Filter (KF), introduced in 1960 by Rudolf Kalman [51], is a powerful mathematical approach to target this purpose. A complete introduction to KF theory is available in appendix C. KF weights measurements equations with dynamic model equations and it continuously provides updated state variables estimations. The performance of KF strongly depends on the quality of the model, and optimality is achieved when the actual measurement process (calibration error aside) behaves as a linear system subject to white Gaussian noise. In practice, estimations optimality is guaranteed under very restrictive conditions. These assumptions, which are reasonable in many applications, may turn out naive when dealing with very complex system as GTs actually are.

In literature, many other works apply KF to similar turbomachinery applications, even if they do not address exactly the same problem. For the time being, KFs have been widely used in the turbine engine community for health monitoring purpose, i.e. for fault detection and identification, false alarms and isolation (see e.g. [47], [77], [26], [15]). In this framework, KF is implemented to solve a different issue, i.e. the estimate of all the GT quantities, even the ones that usually can not be directly measured.

Since GTs are highly non-linear systems, in order to turn around this limitation it is necessary to use an *Extended Kalman Filter* (EKF), i.e. an extension of classical KF oriented to non-linear systems. Non-linearities can be located in the process model or in the measurement equations, EKF in practice applies a classic KF to an approximated model obtained by local linearisation of non-linear global model.

Obviously the final results are strictly dependent on the numerical choices relative to covariance matrices $\boldsymbol{P}_0$, $\boldsymbol{Q}$ and $\boldsymbol{R}$, defined as follows (deeper explanations about these matrices and their mathematical and physical mean-

ing can be found in appendix C):

- $\boldsymbol{P}_0$ is the covariance matrix of initial state variables estimation;
- $\boldsymbol{Q}$ is the covariance matrix relative to process equations;
- $\boldsymbol{R}$ is the covariance matrix relative to measurement equations.

Figure 3.12 represents a high level scheme of the KF based GT model that will be analysed in-depth in the next paragraphs.

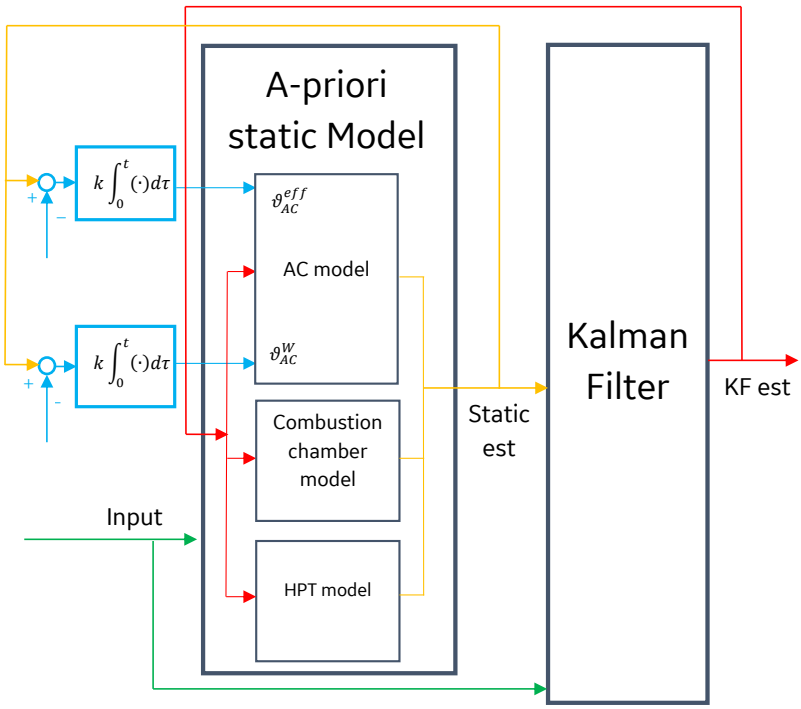

Figure 3.12: Schematic of GT estimation based on Kalman Filter.

Note that the proposed model is a discrete-time model with scan time T_s, where KF is fed both with measurements inputs and static estimations provided by a-priori static model, while KF final estimations are used together with measurements inputs to feed the subsequent static estimation

step. Clearly the lower is T_s the more accurate will be the final KF estimations; however, considering the very high mechanical and thermal inertias of the studied GT, it is not strictly required to have a T_s as small as possible. This configuration creates a closed-loop arrangement, where the outputs of each block are inputs of the other one and vice versa.

Moreover, a-priori static model represented in figure 3.12 is slightly different from the one described in section 3.3, indeed AC model takes as input two additional inputs ϑ_{AC}^{W} and ϑ_{AC}^{eff}. These variables are used to make the AC static model adaptive; as a matter of fact they modify and generalise equations (3.1) and (3.4) in this way

$$W_{AC}^{in} = c_{AC} \cdot \vartheta_{AC}^{W} \cdot \frac{p_{AC}^{in}}{\sqrt{T_{AC}^{in}}} \cdot \sqrt{1 - \left(\frac{p_{AC}^{in}}{p_{AC}^{out}}\right)^2}; \tag{3.15}$$

$$\frac{T_{AC}^{out}}{T_{AC}^{in}} = 1 + \frac{1}{\eta_{AC,is} \cdot \vartheta_{AC}^{eff}} \left[\left(\frac{p_{AC}^{out}}{p_{AC}^{in}}\right)^{\frac{\gamma_{air}-1}{\gamma_{air}}} - 1 \right]. \tag{3.16}$$

These variables allow the static model to adapt itself to observed real system. These additional coefficients can be computed since T_{AC}^{out} and W_{AC}^{in} can be calculated in two independent ways.

- T_{AC}^{out} is estimated by a-priori static model and it is also directly measured by thermocouples;
- W_{AC}^{in} is estimated by a-priori static model exploiting *Stodola's Law*, but it is also involved in the flow conservation law (air is bled in many different sections, these airflows are computed thanks to dedicated maps).

The errors between the two values respectively of T_{AC}^{out} and W_{AC}^{in} are the inputs of two integrators that are used to compute the numerical value of ϑ_{AC}^{W} and ϑ_{AC}^{eff}. These are very simple PID controllers (*Proportional-Integral-Derivative* controllers), where the proportional and the derivative gains are set equal to 0. Thanks to these two loops it is possible to adjust the values of ϑ_{AC}^{W} and ϑ_{AC}^{eff} until the outputs of equations (3.15) and (3.16) are equal respectively to the value of flow computed with the flow balance and the value of temperature measured by dedicated sensors.

Note that in figure 3.12 the two integrators are represented as continuous-time integrators; actually this is only a qualitative diagram of the proposed method, in practice discrete-time integrators have been implemented.

3.4.1 Kalman filter definition

Kalman filter can be implemented in many different ways. In particular to define the whole KF structure it is necessary to choose suitable state variables and to specify a proper dynamic model and a complete measurement equations set.

Although several KF structures have been tested and evaluated during this thesis work, in this chapter only the most effective and accurate version will be presented.

Kalman filter state variables

KF state variables vector $\boldsymbol{x}_k$ is composed of the variables that have to be estimated step after step by exploiting both the knowledge of the process equations that describe how the system evolves and the measurement equations.

In this particular case KF state is composed of 8 variables:

i. $N_{HPT,k}$ - HPT rotational speed;

ii. $\alpha_{HPT,k}$ - HPT rotational acceleration;

iii. $T^{in}_{AC,k}$ - AC inlet temperature;

iv. $T^{out}_{AC,k}$ - AC outlet temperature;

v. $T^{in}_{HPT,k}$ - HPT inlet temperature;

vi. $T^{out}_{HPT,k}$ - HPT outlet temperature;

vii. $\vartheta^{W}_{HPT,k}$ - HPT flow efficiency;

viii. $\vartheta^{eff}_{HPT,k}$ - HPT thermodynamic efficiency.

Where the subscript "k" states that the quantity is relative to k-th discrete step. The exact meaning of the last two variables will be explained in detail in the next paragraphs.

Many of these variables are not really unknown quantities (N_{HPT}, α_{HPT}, T^{in}_{AC} and T^{out}_{HPT} are measured by dedicated sensors)[2], but they have been included within KF state for mathematical convenience; however, by a proper definition of matrices $\boldsymbol{Q}$ and $\boldsymbol{R}$, it is possible to force KF just to smooth these variables in order to avoid high-frequency noise without introducing great deviations from the measured or calculated values.

It is fair to say that from a practical point of view the main interest is focused on T^{in}_{HPT}. Many sensitive mechanical parts, such as stator and rotor HPT blades of AC, HPT and LPT, are exposed to very high temperature, and the most restrictive situation is relative to first stage HPT blades. GT governor[3] has to meet many requirements, such as reference speed tracking, limitation of harmful emissions and AC stall and surge avoidance: in addition there are other control logics that prevent GT from operating in unsafe or unhealthy conditions. T^{in}_{HPT} is the real limitation to GT operative range, indeed this temperature has to be lower than a specific threshold in order to avoid GT residual life drastic reduction or even serious mechanical damages. Since T^{in}_{HPT} can not be directly measured by sensors, it is clear that an accurate estimation of this quantity would be very appreciated to achieve good control performances and reduce safety margins.

[2] HPT rotational acceleration is not directly measured, indeed it is calculated as numerical derivative of N_{HPT}. Starting from a discrete signal u_k (sample time T) the derivative calculated as $d_k = \frac{u_k - u_{k-1}}{T}$ leads to a very noisy signal because of the amplification of high frequencies. To avoid this issue there are many numerical approach to achieve a smoother derivative. In this work the numerical derivative is low-passed by applying the following method

$$d_k = \frac{1}{2}\left(\frac{u_k - u_{k-2}}{2T} + \frac{u_{k-1} - u_{k-3}}{2T}\right) = \frac{u_k + u_{k-1} - u_{k-2} + u_{k-3}}{4T}. \tag{3.17}$$

[3] GT governor means the set of control laws and procedures, both digital and analogic, that are implemented in order to regulate and control the GT steady-state behaviour and dynamical response.

State equations

Always referring to notation of appendix C, the dynamical evolution of the state variables is described by matrix $\boldsymbol{A}_k$, indeed the proposed process dynamical model is very simple and linear.

$$\underbrace{\begin{bmatrix} N_{HPT,k+1} \\ \alpha_{HPT,k+1} \\ T^{in}_{AC,k+1} \\ T^{out}_{AC,k+1} \\ T^{in}_{HPT,k+1} \\ T^{out}_{HPT,k+1} \\ \vartheta^{W}_{HPT,k+1} \\ \vartheta^{eff}_{HPT,k+1} \end{bmatrix}}_{\mathbf{x}_{k+1}} = \underbrace{\begin{bmatrix} 1 & T_s & 0 & 0 & 0 & 0 & 0 & 0 \\ 0 & 1 & 0 & 0 & 0 & 0 & 0 & 0 \\ 0 & 0 & 1 & 0 & 0 & 0 & 0 & 0 \\ 0 & 0 & 0 & 1 & 0 & 0 & 0 & 0 \\ 0 & 0 & 0 & 0 & 1 & 0 & 0 & 0 \\ 0 & 0 & 0 & 0 & 0 & 1 & 0 & 0 \\ 0 & 0 & 0 & 0 & 0 & 0 & 1 & 0 \\ 0 & 0 & 0 & 0 & 0 & 0 & 0 & 1 \end{bmatrix}}_{\boldsymbol{A}_k} \underbrace{\begin{bmatrix} N_{HPT,k} \\ \alpha_{HPT,k} \\ T^{in}_{AC,k} \\ T^{out}_{AC,k} \\ T^{in}_{HPT,k} \\ T^{out}_{HPT,k} \\ \vartheta^{W}_{HPT,k} \\ \vartheta^{eff}_{HPT,k} \end{bmatrix}}_{\mathbf{x}_k} + \underbrace{\begin{bmatrix} w_k^{N_{HPT}} \\ w_k^{\alpha_{HPT}} \\ w_k^{T^{in}_{AC}} \\ w_k^{T^{out}_{AC}} \\ w_k^{T^{in}_{HPT}} \\ w_k^{T^{out}_{HPT}} \\ w_k^{\vartheta^{W}_{HPT}} \\ w_k^{\vartheta^{eff}_{HPT}} \end{bmatrix}}_{\boldsymbol{w}_k}$$

where $\boldsymbol{w}_k$ is an AWGN vector with covariance matrix $\boldsymbol{Q}$ that describes the uncertainties on the process model. For the sake of simplicity it has been preferred to use a trivial process model, in which the only "physical relationship" is the connection between HPT rotational speed and accelerations (first row in matrix $\boldsymbol{A}_k$). In all the other equations each state variable remains equal to itself, except for the uncertainty introduced by the additive noise: this leads to a very flexible model in which the dynamical evolution of the estimations is guaranteed by measurement equations.

Measurement equations

Before defining measurement equations it is necessary to describe in detail the last two state variables, i.e. ϑ^{W}_{HPT} and ϑ^{eff}_{HPT} defined in bullets (vii) and (viii). These quantities are very similar to ϑ^{W}_{AC} and ϑ^{eff}_{AC}, indeed equations (3.11) and (3.14) can be updated and generalised as follows

$$W_{HPT}^{in} = c_{HPT} \cdot \vartheta_{HPT}^{W} \cdot \frac{p_{HPT}^{in}}{\sqrt{T_{HPT}^{in}}} \cdot \sqrt{1 - \left(\frac{p_{HPT}^{out}}{p_{HPT}^{in}}\right)^{2}};$$
$$\frac{T_{HPT}^{out}}{T_{HPT}^{in}} = 1 - \eta_{HPT,is} \cdot \vartheta_{HPT}^{eff} \left[1 - \left(\frac{p_{HPT}^{out}}{p_{HPT}^{in}}\right)^{\frac{\gamma_{gas}-1}{\gamma_{gas}}}\right].$$

By consequence, it is possible to define two virtual measurement equations, i.e. measurements that are not actually provided by sensors but are computed as combination of other quantities which are related to ϑ_{HPT}^{W} and ϑ_{HPT}^{eff}.

$$\begin{aligned} \bar{Y}_{HPT,k}^{W} = h_{HPT}^{W}(\boldsymbol{x}_k) = \frac{\sqrt{T_{HPT,k}^{in}}}{\vartheta_{HPT,k}^{W}} = \\ = c_{HPT} \cdot \frac{\bar{p}_{HPT,k}^{in}}{W_{HPT,k}^{in}} \cdot \sqrt{1 - \left(\frac{\bar{p}_{HPT,k}^{out}}{\bar{p}_{HPT,k}^{in}}\right)^{2}} \end{aligned} \tag{3.18}$$

$$\begin{aligned} \bar{Y}_{HPT,k}^{eff} = h_{HPT}^{eff}(\boldsymbol{x}_k) = \frac{T_{HPT,k}^{in} - T_{HPT,k}^{out}}{T_{HPT,k}^{in} \cdot \vartheta_{HPT,k}^{eff}} = \\ = \eta_{HPT,is} \cdot \left[1 - \left(\frac{\bar{p}_{HPT,k}^{out}}{\bar{p}_{HPT,k}^{in}}\right)^{\frac{\gamma_{gas}-1}{\gamma_{gas}}}\right] \end{aligned} \tag{3.19}$$

where the bar over the variable denotes that the value is directly measured by sensors or obtained by combination of direct measurements.

Furthermore, the global power balance concerning the whole GG can be addressed by introducing a third virtual measurement equation. This is a fundamental equation in the proposed KF, indeed it describes from a dynamical point of view how the thermodynamic quantities influence the power balance of the GG. In practice, this additional virtual measurement equation defines a link between thermodynamic and mechanical quantities, thus it is essential to keep a global view on the system. This means that this equation allows the KF to find out the optimal estimations of the involved variables, taking into account both direct measurements with their

own uncertainties and virtual measurement that describe the global shaft power balance. Therefore, the third virtual measurement equation is

$$\begin{aligned}\bar{Y}_k^{GG} = h_{GG}(\boldsymbol{x}_k) = \overbrace{\left(\frac{\pi}{30}\right)^2}^{\frac{rpm^2}{s}\, to\, \frac{rad^2}{s}} \bar{N}_{HPT,k} \cdot \bar{\alpha}_{HPT,k} = \\ = \frac{W_{HPT,k}^{in} \cdot c_{p,gas} \cdot (T_{HPT,k}^{in} - T_{HPT,k}^{out})}{J_{GG}} + \\ - \frac{W_{AC,k}^{in} \cdot c_{p,air} \cdot (T_{AC,k}^{out} - T_{AC,k}^{in})}{\eta_m \cdot J_{GG}}\end{aligned} \tag{3.20}$$

where J_{GG} is the value of the whole GG inertia, while η_m is the AC mechanical efficiency. As described in [102], delivered/absorbed power is proportional to flow and temperature jump. AC and HPT are on the same shaft mechanically connected, thus equation (3.20) in practice states that the GG whole acceleration/deceleration is proportional to the difference between the HPT delivered power and the AC absorbed power. Reasonably, if the HPT delivered power is greater than AC absorbed power then N_{HPT} will increase, on the contrary if the HPT delivered power is lower than AC absorbed power then N_{HPT} will decrease.

Finally, measurement equations can be written as

$$\begin{bmatrix} \bar{N}_{HPT,k} \\ \bar{Y}_k^{GG} \\ \bar{T}_{AC,k}^{out} \\ \bar{T}_{HPT,k}^{in} \\ \bar{T}_{HPT,k}^{out} \\ \bar{T}_{AC,k}^{in} \\ \bar{Y}_{HPT,k}^{W} \\ \bar{Y}_{HPT,k}^{eff} \end{bmatrix} = \underbrace{\begin{bmatrix} N_{HPT,k} \\ h_{GG}(\boldsymbol{x}_k) \\ T_{AC,k}^{out} \\ T_{HPT,k}^{in} \\ T_{HPT,k}^{out} \\ T_{AC,k}^{in} \\ h_{HPT}^{W}(\boldsymbol{x}_k) \\ h_{HPT}^{eff}(\boldsymbol{x}_k) \end{bmatrix}}_{\boldsymbol{h}(\boldsymbol{x}_k)} + \underbrace{\begin{bmatrix} \eta_k^{\bar{N}_{HPT}} \\ \eta_k^{\bar{Y}^{GG}} \\ \eta_k^{\bar{T}_{AC}^{out}} \\ \eta_k^{\bar{T}_{HPT}^{in}} \\ \eta_k^{\bar{T}_{HPT}^{out}} \\ \eta_k^{\bar{T}_{AC}^{in}} \\ \eta_k^{\bar{Y}_{HPT}^{W}} \\ \eta_k^{\bar{Y}_{HPT}^{eff}} \end{bmatrix}}_{\boldsymbol{\eta}_k} \tag{3.21}$$

where $\bar{T}_{HPT,k}^{in}$ is the backward value of inlet HPT temperature provided by equation (3.14) , thus it is considered to be retrieved from a virtual sensor.

The uncertainties on measurement equations are described by $\boldsymbol{\eta}_k$, which is an AWGN vector with covariance matrix $\boldsymbol{R}$. Note that $\boldsymbol{h}(\boldsymbol{x}_k)$ is a vector composed of 8 measurement equations, some of which are non-linear with respect to state variables $\boldsymbol{x}_k$.

Since equations (3.21) are not linear, as explained in appendix C, it is necessary to linearise $\boldsymbol{h}(\boldsymbol{x}_k)$ in order to use EKF.

$$\boldsymbol{C}_k = \frac{\partial \boldsymbol{h}(\boldsymbol{x}_k)}{\partial \boldsymbol{x}_k} = \begin{bmatrix} 1 & 0 & 0 & 0 & 0 & 0 & 0 & 0 \\ 0 & 0 & c_k^{2,3} & c_k^{2,4} & c_k^{2,5} & c_k^{2,6} & 0 & 0 \\ 0 & 0 & 0 & 1 & 0 & 0 & 0 & 0 \\ 0 & 0 & 0 & 0 & 1 & 0 & 0 & 0 \\ 0 & 0 & 0 & 0 & 0 & 1 & 0 & 0 \\ 0 & 0 & 1 & 0 & 0 & 0 & 0 & 0 \\ 0 & 0 & 0 & 0 & c_k^{7,5} & 0 & c_k^{7,7} & 0 \\ 0 & 0 & 0 & 0 & c_k^{8,5} & c_k^{8,6} & 0 & c_k^{8,8} \end{bmatrix} \tag{3.22}$$

where the matrix elements are analytically calculated by evaluating in correspondence of the last KF estimations these quantities:

- $c_k^{2,3} = \frac{W_{AC,k}^{in} \cdot c_{p,air}}{\eta_m \cdot J_{GG}}$;
- $c_k^{2,4} = -\frac{W_{AC,k}^{in} \cdot c_{p,air}}{\eta_m \cdot J_{GG}}$;
- $c_k^{2,5} = \frac{W_{HPT,k}^{in} \cdot c_{p,gas}}{J_{GG}}$;
- $c_k^{2,6} = -\frac{W_{HPT,k}^{in} \cdot c_{p,gas}}{J_{GG}}$;
- $c_k^{7,5} = \frac{1}{2\sqrt{T_{HPT,k}^{in} \cdot \vartheta_{HPT,k}^{W}}}$;
- $c_k^{7,7} = \frac{-\sqrt{T_{HPT,k}^{in}}}{\vartheta_{HPT,k}^{W}}$;
- $c_k^{8,5} = \frac{T_{HPT,k}^{out}}{\vartheta_{HPT,k}^{eff} \cdot (T_{HPT,k}^{in})^2}$;
- $c_k^{8,6} = \frac{-1}{T_{HPT,k}^{in} \cdot \vartheta_{HPT,k}^{eff}}$;
- $c_k^{8,8} = \frac{T_{HPT,k}^{out} - T_{HPT,k}^{in}}{T_{HPT,k}^{in} \cdot (\vartheta_{HPT,k}^{eff})^2}$.

In this way, even if the model is linearised, step by step it is approximated around the last estimation, thus it is reasonable to suppose that in a certain neighbourhood of the last estimation this approximation is acceptable.

3.4.2 Kalman Filter results

In this section the results relative to the Kalman filter proposed in 3.4.1 are reported and commented. The proposed Kalman filter has been validated both with respect to *GG extended NPSS dataset* and with respect to *full extended NPSS dataset*.

Kalman Filter results with respect to GG extended NPSS dataset

Figures 3.13, 3.14 and 3.15 represent respectively the percentage estimation error relative to T_{AC}^{out}, T_{HPT}^{out} and T_{HPT}^{in} with respect to *GG extended NPSS dataset*. Figure 3.13 clearly shows that the error on T_{AC}^{out} is negligible, and this is due to the fact that T_{AC}^{out} is either measured and estimated. The error relative to T_{HPT}^{out} of 3.14 is slightly greater, but is still acceptable.

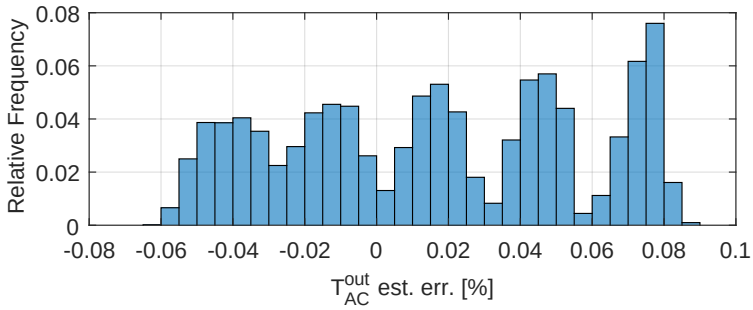

Figure 3.13: KF T_{AC}^{out} percentage estimation error with respect to *GG extended NPSS dataset*.

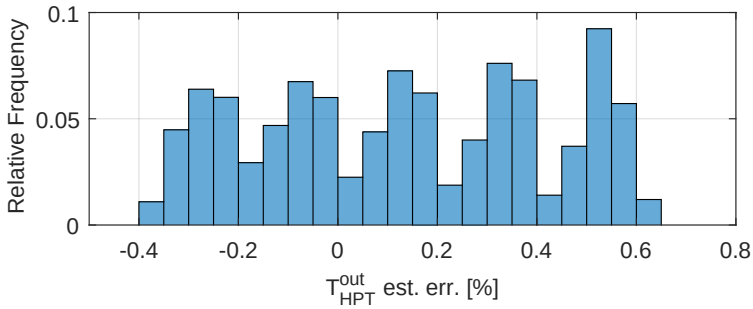

Figure 3.14: KF T^{out}_{HPT} percentage estimation error with respect to *GG extended NPSS dataset*.

Figure 3.15 is the most important, indeed it represents the estimation error of T^{in}_{HPT}, that is the temperature that can not be measured in real plants. The error distribution is nearly Gaussian with a mean value $\mu \simeq -0.3\%$ and a standard deviation $\sigma \simeq 0.15\%$.

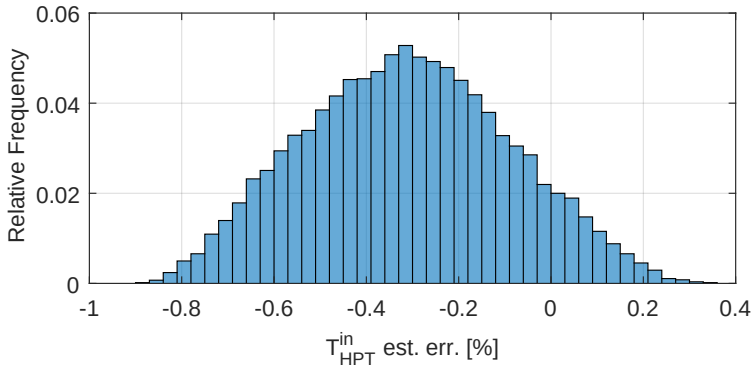

Figure 3.15: KF T^{in}_{HPT} percentage estimation error with respect to *GG extended NPSS dataset*.

Figures 3.16, 3.17 and 3.18 represent the percentage error of the flows estimations, always with respect to *GG extended NPSS dataset*. The three

distributions are quite similar and they are very close to Gaussian distributions. It is worth noticing that the *GG extended NPSS dataset* takes into account only the gas generator. Nevertheless, before introducing the LPT variability, it is important to be sure that the KF guarantees good results even in this simplified case.

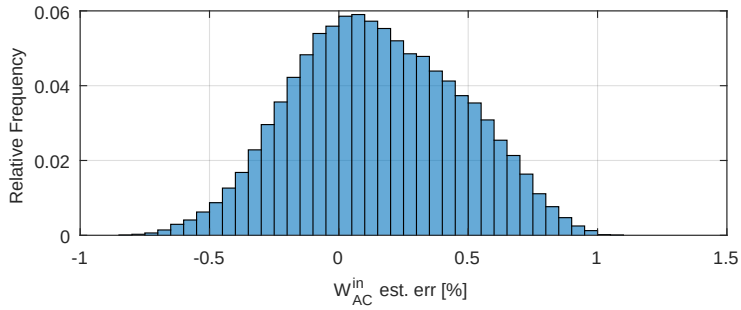

Figure 3.16: KF W_{AC}^{in} percentage estimation error with respect to *GG extended NPSS dataset*.

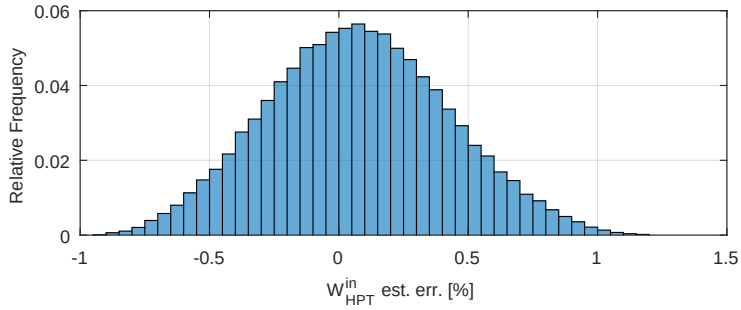

Figure 3.17: KF W_{HPT}^{in} percentage estimation error with respect to *GG extended NPSS dataset*.

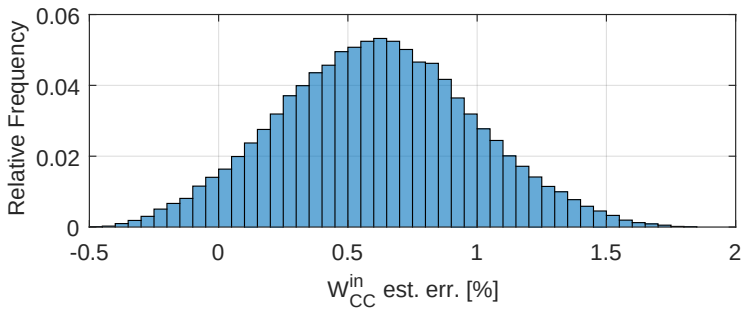

Figure 3.18: KF W_{CC}^{in} percentage estimation error with respect to *GG extended NPSS dataset*.

Kalman Filter results with respect to full extended NPSS dataset

In this paragraph the percentage errors relative to temperatures and flows of the Kalman filter with respect to the *full extended NPSS dataset* are reported. These results are more significant, indeed they show how the proposed estimation algorithm works considering a dataset in which all the six CPs change. In particular it can be noticed that the percentage errors are quite lower with respect to the ones depicted in figures 3.6 and 3.7. This means that the KF is able to compensate the variation introduced by the changing of CPs, thus it is able to adapt itself to the particular model under analysis.

In figures 3.19, 3.20, 3.22, 3.23 and 3.24 the error distribution is clearly composed of the sum of five Gaussian distributions: this is due to the fact that the algorithm tries to evaluate the modification introduced by the LPT CP of the relative quantities, but it is not able to totally compensate it. Only figure 3.21 is characterised by a single Gaussian distribution with a mean value $\mu \simeq -0.3\%$ and a standard deviation $\sigma \simeq 0.2\%$, and this is due to the fact that there is not a CP that directly affects T_{HPT}^{in}, thus the global effect on this quantity is the sum of the single effect that results in a single Gaussian distribution. Note that the error distributions in figures 3.15 and

3.21 are comparable; considering that T_{HPT}^{in} is the most critical quantity this is a very appreciable feature, indeed it states that the proposed KF behaves similarly with respect to *GG extended NPSS dataset* and *full extended NPSS dataset*.

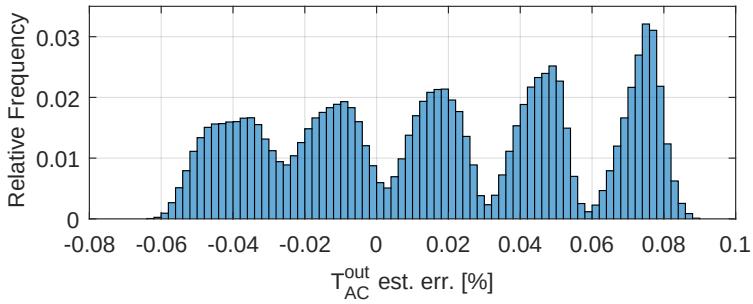

Figure 3.19: KF T_{AC}^{out} percentage estimation error with respect to *full extended NPSS dataset*.

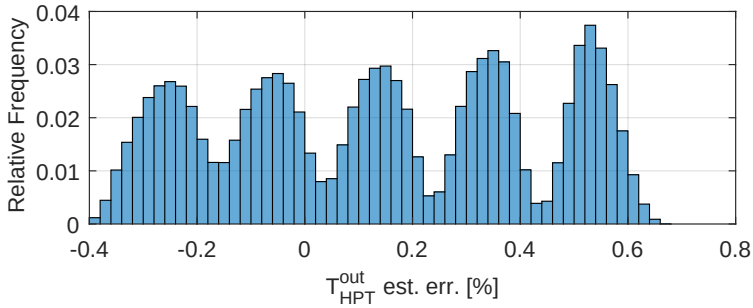

Figure 3.20: KF T_{HPT}^{out} percentage estimation error with respect to *full extended NPSS dataset*.

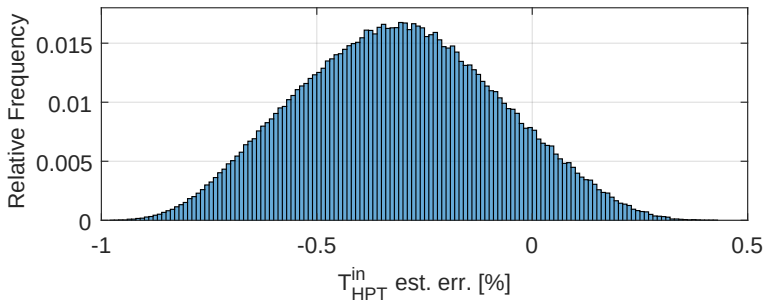

Figure 3.21: KF T^{in}_{HPT} percentage estimation error with respect to *full extended NPSS dataset.*

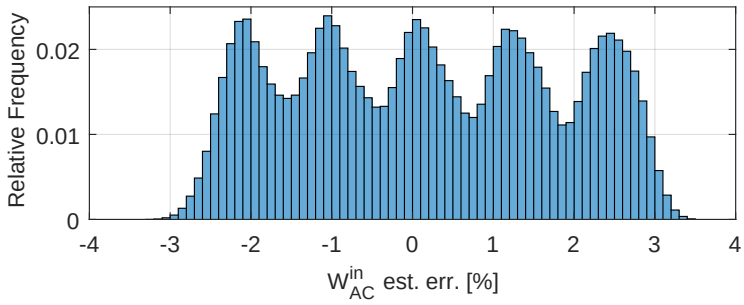

Figure 3.22: KF W^{in}_{AC} percentage estimation error with respect to *full extended NPSS dataset.*

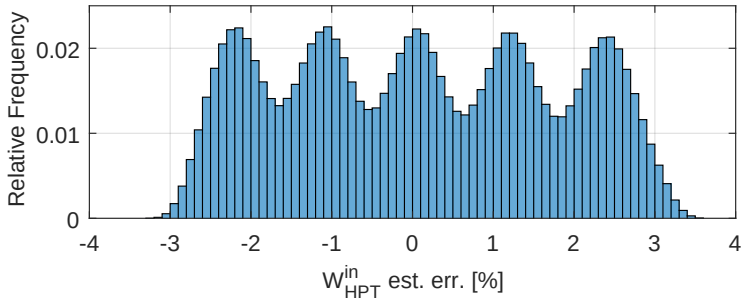

Figure 3.23: KF W^{in}_{HPT} percentage estimation error with respect to *full extended NPSS dataset*.

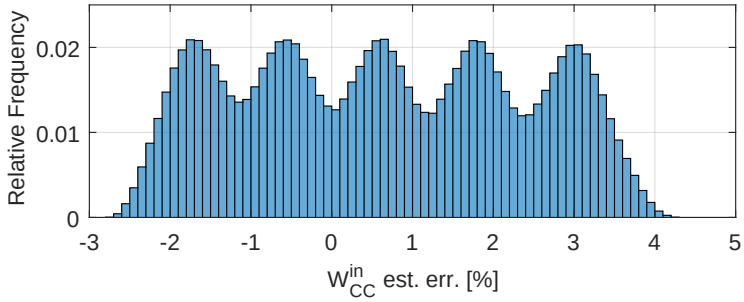

Figure 3.24: KF W^{in}_{CC} percentage estimation error with respect to *full extended NPSS dataset*.

Finally, it is immediate to notice that errors on flows estimations are definitely greater with respect to the errors on temperatures estimations; this is due to the fact that there are not suitable measurements that make the proposed model directly aware about flows deviations from nominal values, thus it is very complex to reduce these errors.

3.5 Kalman Filter LHV estimation

KF model estimation introduced in section 3.4 does not rely on equation (3.9), indeed it exploits only the "backward" estimation of T^{in}_{HPT} provided by equation (3.14). This feature of the KF can be exploited to allow the estimation of an additional fundamental quantity, i.e. LHV.

LHV is a property of a fuel, and it is defined as the amount of heat released by combusting a unit mass of fuel; thus, this quantity is needed to characterised the fuel from an energetic point of view. LHV is very important to control the GT, indeed its knowledge is required in order to compute the exact quantity of fuel to be injected in combustion chamber. In fact GT governor at first considers the nominal value LHV^{nom} to compute the normalised fuel request, then the actual fuel request is calculated multiplying by the ratio LHV^{nom}/LHV^{meas}; if $LHV^{meas} > LHV^{nom}$ it means that the unit mass of fuel "contains" more energy, thus it is sufficient to inject a lower fuel flow, on the contrary if $LHV^{meas} < LHV^{nom}$ a greater quantity of fuel is required.

By inverting equation (3.9) it is easy to achieve an estimation of LHV based on the estimation of T^{in}_{HPT} provided by KF.

$$\begin{aligned} \hat{LHV} = \frac{1}{\eta_{CC}} \Big[& T^{in}_{HPT,KF} \cdot \left(c_{p,air} AFR + c_{p,fuel}\right) + \\ & - \bar{T}_{fuel} \cdot c_{p,fuel} - T^{out}_{AC,KF} \cdot AFR \cdot c_{p,air} \Big] \end{aligned} \tag{3.23}$$

Where the bar over the variable states again that the quantity is directly measured, while the additional subscript "KF" states that the quantity is the estimation provided by KF.

The introduction of LHV estimation is very useful from two points of view:

i. As explained in the previous sections an accurate knowledge of T_{HPT}^{in} and LHV is fundamental to control the GT. T_{HPT}^{in} can not be measured and it needs to be estimated, while LHV is usually measured by a gas chromatograph, that is a very complex and expensive transducer. This estimation method of LHV can be seen as a virtual sensor able to work in parallel with the physical sensor (or even substitute it). This *soft sensor* would bring many benefits, indeed it would increase the operability and the reliability of the system, reducing at the same time the total cost and instrumentation complexity;

ii. Concerning *GG extended NPSS dataset* and *full extended NPSS dataset* both LHV and T_{HPT}^{in} numerical values are available, thus it is possible to define an estimation error for both of them. In *real trend datasets* the measured value of T_{HPT}^{in} is not available, thus it is necessary to find out another index to evaluate the goodness of the method. LHV is a perfect quantity to do this, indeed it is almost always available on aero-derivative GTs and it is directly connected to T_{HPT}^{in}, thus it is reasonable to suppose that if LHV estimation is accurate then also the T_{HPT}^{in} estimation will be acceptable (even if it is not possible to directly evaluate it).

3.5.1 Kalman Filter LHV estimation: results

Kalman Filter LHV estimation results with respect to GG extended NPSS dataset

Figure 3.25 represents the LHV percentage estimation error relative to *GG extended NPSS dataset*. The error distribution is almost Gaussian and it is not biased ($\mu \simeq 0\%$, $\sigma \simeq 0.5\%$). Standing from equation (3.23) it is clear that the estimation of LHV is strictly connected with the estimation of T_{HPT}^{in}: the reason why the standard deviation of the distribution in figure

3.25 is significantly greater than the standard deviation of the distribution in figure 3.15 is that equation (3.23) depends also on η_{CC}, thus it is much more affected by the GG CPs.

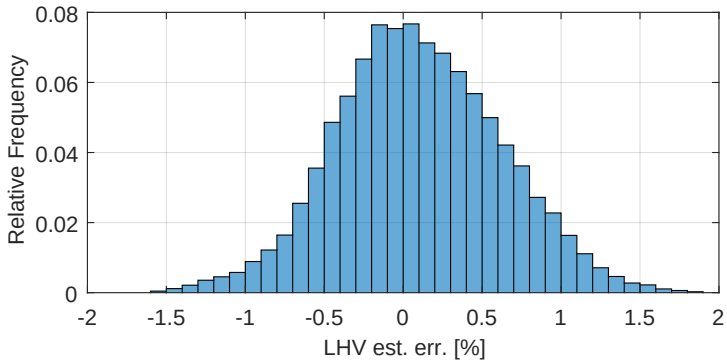

Figure 3.25: KF percentage error on LHV estimation with respect to *GG extended NPSS dataset*.

Kalman Filter LHV estimation results with respect to full extended NPSS dataset

Figure 3.26 represents the LHV percentage estimation error relative to *full extended NPSS dataset*. Once again, the distribution of figure 3.26 seems to be the sum of several nearly-Gaussian distributions. The motivation, as mentioned in paragraph 3.4.2, is that the proposed model-based on KF is not able to follow the variations introduced by the CPs relative to LPT: this means that KF is almost blind with respect to variations of LPT model, thus the more it varies the more the error will grow.

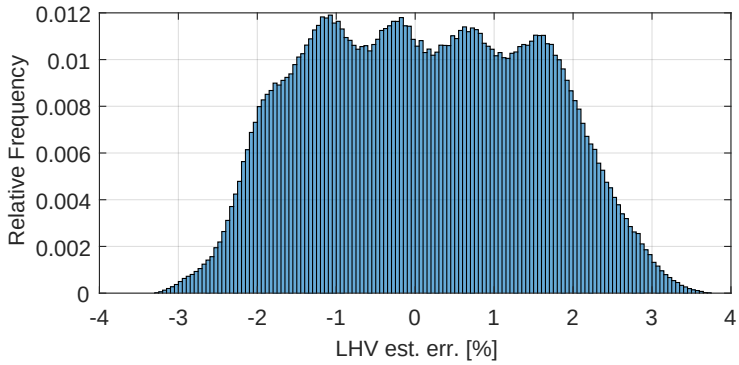

Figure 3.26: KF percentage error on LHV estimation with respect to *full extended NPSS dataset*.

Kalman Filter LHV estimation results with respect to real trend dataset

Figure 3.27 and 3.28 represent the LHV percentage estimation error relative to six *real trend datasets*. In these six different examples the errors have different mean values, and this is due to the fact that each single plant has its own characteristics that should be taken into account to compensate the particular mean error. Nevertheless, all the tests on real data have underlined a periodic component on the percentage error with period $T_e \simeq$ 1440 minutes, which is surprisingly near to 1 day. Actually, this can be easily explained considering that all the atmospheric phenomena and weather quantities have a periodicity equal to 1 day. For example air humidity has this periodic component and it is not considered in the proposed algorithm even if it affects the GT response: this is the reason why the error has always this specific harmonic component.

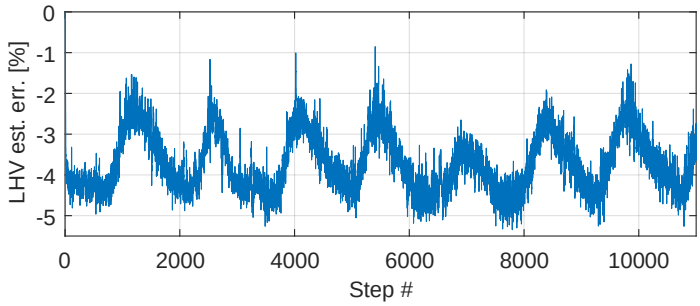

(a) *LHV estimation error with respect to gas chromatograph measurements (real trend dataset 1).*

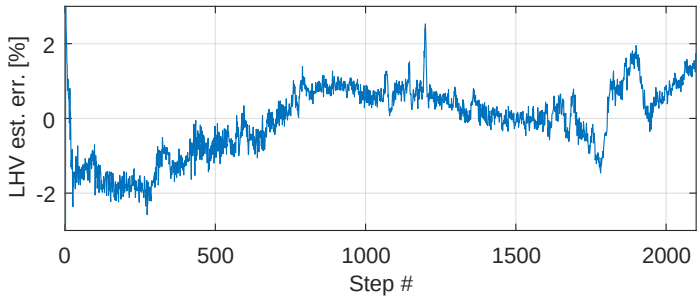

(b) *LHV estimation error with respect to gas chromatograph measurements (real trend dataset 2).*

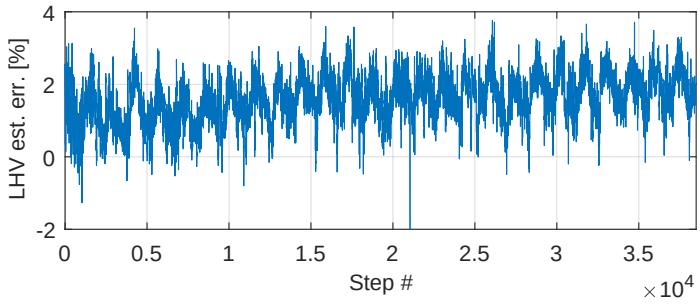

(c) *LHV estimation error with respect to gas chromatograph measurements (real trend dataset 3).*

Figure 3.27: LHV estimation percentage errors (*real trend datasets*, 1 *Step* corresponds to 1 *minute*).

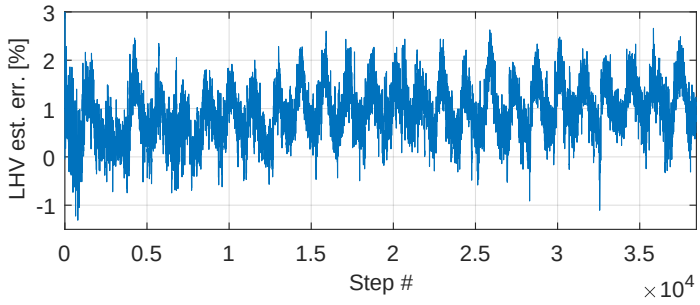

(a) *LHV estimation error with respect to gas chromatograph measurements (real trend dataset 4).*

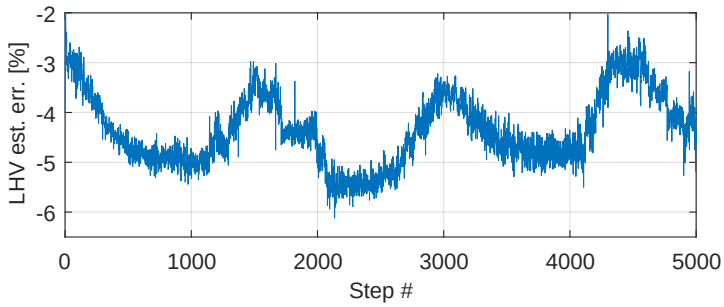

(b) *LHV estimation error with respect to gas chromatograph measurements (real trend dataset 5).*

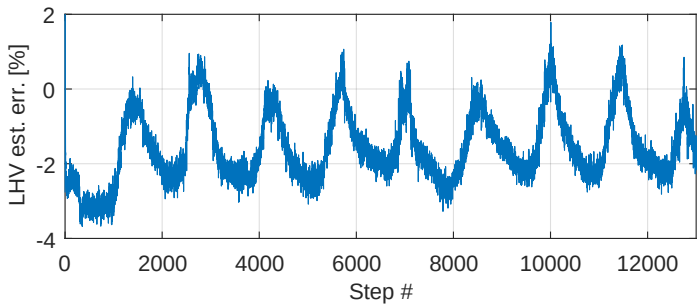

(c) *LHV estimation error with respect to gas chromatograph measurements (real trend dataset 6).*

Figure 3.28: LHV estimation percentage errors (*real trend datasets*, 1 *Step* corresponds to 1 *minute*).

3.6 Results analysis and conclusions

In this chapter a suitable mathematical model of the aero-derivative twin-shaft gas turbine GE LM2500+G4 DLE has been proposed. In particular, the gas generator of this GT has been modelled introducing an iterative double-step method:

1. the first step is based on generalised maps and thermodynamic laws that allow an a-priori static estimation of flows, temperatures and pressures of each GG section;

2. the second step provides dynamic estimations based on a Kalman Filter that corrects the a-priori estimations exploiting all available measurements and the thermodynamic/mechanical equilibrium of the system.

The model has been trained and validated with respect to several datasets obtained exploiting NPSS. Moreover, concerning the estimation of LHV, also real trend datasets have been used to validate the GT mathematical model.

The main results can be summarised as follows:

i. a-priori static model is able to reproduce the *nominal NPSS dataset*, but it is characterised by large inaccuracies when the system moves far away from the nominal one;

ii. the introduction of the second step based on KF allows the compensation of many non-idealities of the system, above all regarding the estimation of T_{HPT}^{in}. Figure 3.21 shows that the error with respect to *full extended NPSS datased* has a Gaussian distribution with maximum percentage value lower the 1%;

iii. in order to reduce installation costs, flow transducers are not available in the GT under analysis. In turn, there are not direct measurements that allow the reduction of the error on flows estimation, and this is the reason why flows estimations are characterised by greater errors.

In view of the foregoing, the proposed model represents a comprehensive method to describe the behaviour of the GT under analysis in all the reasonable operating conditions, both in steady state and transient conditions.

This mathematical model can be used as *soft sensor* able to provide indirect measurement of LHV. This *soft sensor* has been validated also with respect to *real trend datasets*, and results have shown that the estimation error is composed of a systematic and a periodic component of 24 hours. The former is due to modelling inaccuracies, while the second is linked to the oscillation of meteorological quantities such as atmospheric humidity. The goodness of the results paves the way for a wider field of application of this approach. As mentioned previously, the immediate use of such a model is as *soft sensor* to achieve indirect measurement of all the relevant quantities that characterise the GT operating point. Concerning the usually unavailable measurements, this would lead to an increased awareness about the whole system; among many unmeasured quantities, an accurate estimation of T_{HPT}^{in} allows a more effective control of the machine, reducing at the same time the amplitude of the margin needed to assure the physical integrity of the system. Moreover, this *soft sensor* could also be used to reduce the installation cost by estimating other quantities (such as LHV) that are normally measured by expensive, bulk and invasive sensors that generally need to be physically redounded. A second field of application of this estimation method is the offline prediction of the GT performances: this would guarantee a realistic evaluation of the GT response under specific conditions without relying on a real running machine.

Finally, a deep knowledge about the system can help in estimating the ageing and the physical decay of each engine component. Indeed, the augmented knowledge about all the GT quantities can be exploited also to feed proper algorithms to estimate the residual life of the system. An estimation of the residual life closer to reality can be used to avoid premature and needless maintenance operations that on the contrary would be performed only when strictly required.

Chapter 4

Conclusions and Final Remarks

The analysis and the techniques proposed in this work have highlighted the potential of the model-based approach in oil and gas applications. A mathematical model based on a deep knowledge of the system physics leads to the improvement of existing oil and gas plants without requiring the modification of already installed equipment.

As shown in Chapters 1 and 3, a reliable modelling of the particular subsystem under analysis unlocks the full capabilities of the available equipment. By introducing proper models focused on specific behaviour of the system it is possible to develop suitable methods which are aimed to the enhancement of the system reliability, operability and robustness. Thanks to these models it is possible to compensate and overcome system lacks or limitations without introducing expensive or overkill solution. A common issue of many algorithms is that they are time consuming and high resources demanding methods, thus they are scarcely applicable in a real plant. On the contrary one of the main purposes of this work has been to keep each algorithm "as simple as possible". Indeed, each procedure has been conceived to be able to work on a potentially available CPU, thus the run-time complexity of each method should be as small as possible.

Furthermore, concerning the topic introduced in Chapter 2, the mathematical modelization both of the mechanical and the electric part of a power

generation plant has drawn the attention to the real features of the plant that are at the basis of torsional instability. The awareness of the root causes of this unstable phenomenon has allowed the implementation of an effective mitigation technique able to force to system to maintain stability.

Nowadays, in order to keep pace with the scientific and technological practices, it is clear that it is necessary to lean forward to embrace, develop and rapidly adopt these new solutions. Model-based techniques indeed represent a unique opportunity to unleash the whole potential of the available equipment without requiring additional and expensive installations.

Appendix A

Thermodynamics of Real Gases

Almost all of the gases handled by process practical applications (such as compressors) are characterised by a pronounced real gas behaviour. This is the reason why it is required to modify the well-known equation of perfect gas introducing the parameter Z, i.e. the *compressibility* of the real gas. Therefore, the real gas equation becomes

$$Z = \frac{pv}{RT}, \tag{A.1}$$

where:

- Z is the gas compressibility;
- $R \simeq 8.31 \frac{J}{mol \cdot K}$ is the universal gas constant;
- p is the gas pressure;
- T is the gas temperature;
- v is the gas specific volume.

Note that $Z \in [0; 1]$ is a pure number, and the perfect gas equation can be achieved by imposing $Z = 1$.

In 1873 Van der Waals proposed the first technique to compute Z

$$Z = \frac{v}{v - b} - aRTv, \tag{A.2}$$

with a and b coefficients to be determined connected to real gas peculiarities and intermolecular dynamics.

In the second half of twentieth century many effective approaches to calculate a generalised real gas equation of state have been introduced by several scientists. Four real gas equations are described below.

A.1 BWRS equation of state

Benedict, Webb, Rubin and Starling published a new procedure to calculate Z in 1973.

$$Z = 1 + \frac{B}{v} + \frac{C}{v^2} + \frac{D}{v^5} + \frac{E}{v^2}\left(1 + \frac{\gamma}{v^2}\right)e^{-\gamma/v^2}, \tag{A.3}$$

where

$$\begin{aligned} B &= \left(\frac{1}{RT}\right)\left(B_0 RT - A_0 - \frac{C_0}{T^2} + \frac{D_0}{T^3} - \frac{E_0}{T^4}\right); \\ C &= \left(\frac{1}{RT}\right)\left(bRT - a - \frac{d}{T}\right); \\ D &= \left(\frac{1}{RT}\right)\alpha\left(\alpha + \frac{d}{T}\right); \\ D &= \left(\frac{1}{RT}\right)\left(\frac{c}{T^2}\right). \end{aligned} \tag{A.4}$$

The unknown coefficients of equation (A.4) can be retrieved in [56].

A.2 RKS equation of state

Redlich, Kwong and Soave in 1949 suggested a modification to Van Der Waals equation (A.2).

$$Z = \frac{v}{v-b} - \frac{a}{\left[RT(v+b)\right]}. \tag{A.5}$$

Even in this case, unknown coefficients of equation (A.5) can be retrieved in [56].

A.3 LKP equation of state

Lee, Kesler and Prausnitz proposed a new method to calculate Z in 1976.

$$Z = Z^0 + \frac{\omega}{\omega^r}(Z^r - Z^0). \tag{A.6}$$

The compressibility factors of the "simple fluid" Z^0 and the "reference fluid" Z^r are calculated separately by a modified BWRS equation. ω^r represents the *non-sphericity* of a molecule, expressing how a molecule is complex (geometry and polarity). ω^r ranges from zero for simple monatomic gases to approximately 0.9 for complex molecule structures.

In order to find out the numerical value of Z^0 and Z^r there are some coefficients that can be retrieved in [56].

A.4 PR Equation of State

Peng and Robinson published their modification of the Van Der Waals equation (1976), known as the PR equation of state.

$$Z = \frac{v}{v-b} - \frac{v}{RT}\frac{a}{\big[v(v+b)+b(v-b)\big]}. \tag{A.7}$$

Once again, unknown coefficients of equation (A.7) can be retrieved in [56].

Appendix B

Least Squares Theory

Let's consider the parametric linear model

$$\Sigma(\boldsymbol{\vartheta})\text{: } y_k = \boldsymbol{\varphi}_k^T\, \boldsymbol{\vartheta} = \varphi_k^1 \vartheta^1 + \varphi_k^2 \vartheta^2 + \cdots + \varphi_k^n \vartheta^n, \tag{B.1}$$

where:

- subscript k states that the quantity is referred to the k-th step;
- $\boldsymbol{\vartheta} \in \mathbb{R}^n$ is the coefficient vector that needs to be identified;
- $\boldsymbol{\varphi} \in \mathbb{R}^n$ is the input vector;
- $y \in \mathbb{R}$ is the output value.

In practice, model (B.1) states that output y can be seen as a linear combination of inputs. Identification of parameters vector $\boldsymbol{\vartheta}$ is based on the minimization of a cost function J_N. If data are acquired in N steps, the cost function is defined as

$$J_N(\boldsymbol{\vartheta}) = \frac{1}{N} \sum_{k=1}^{N} (y_k - \boldsymbol{\varphi}_k^T\, \boldsymbol{\vartheta})^2, \tag{B.2}$$

and the coefficient vector $\boldsymbol{\vartheta}$ is equal to

$$\boldsymbol{\vartheta} \in arg \min_{\boldsymbol{\vartheta}} J_N(\boldsymbol{\vartheta}). \tag{B.3}$$

There are two analytic methods to solve this minimization:

1. *Classic least squares*: once all the data have been acquired from step 1 to step N, it computes vector $\hat{\boldsymbol{\vartheta}}$ (a complete analysis of *classic least squares* can be found in many manuals such as [58], [27] or [25]);

2. *Recursive least squares (RLS)*: step by step it updates the coefficient vector $\hat{\boldsymbol{\vartheta}}_k$, and it is possible to prove that $\hat{\boldsymbol{\vartheta}}_N$ is exactly equal to the value $\hat{\boldsymbol{\vartheta}}$ that classic least squares method would return with the same inputs (further details about RLS can be found e.g. in [42]).

B.1 Classic least squares

It is possible to demonstrate that the vector $\hat{\boldsymbol{\vartheta}}$ that minimises the cost function J_N is equal to

$$\hat{\boldsymbol{\vartheta}} = S(N)^{-1} \sum_{k=1}^{N} \boldsymbol{\varphi}_k \, y_k, \tag{B.4}$$

where

$$S(N) = \sum_{k=1}^{N} \boldsymbol{\varphi}_k \, \boldsymbol{\varphi}_k^T. \tag{B.5}$$

B.2 Recursive least squares (RLS)

This method updates the estimation after each step by repeating the following recursive equations (the algorithm can be initialised with the first step data):

i. $\boldsymbol{S}_k = \boldsymbol{S}_{k-1} + \boldsymbol{\varphi}_k \, \boldsymbol{\varphi}_k^T$;

ii. $\boldsymbol{K}_k = \boldsymbol{S}_k^{-1} \boldsymbol{\varphi}_k$;

iii. $\varepsilon_k = y_k - \boldsymbol{\varphi}_k^T \hat{\boldsymbol{\vartheta}}_{k-1}$;

iv. $\hat{\boldsymbol{\vartheta}}_k = \hat{\boldsymbol{\vartheta}}_{k-1} + \boldsymbol{K}_k \varepsilon_k$.

In practice, these equations are not used due to computational problems. Indeed it is possible to define other equations mathematically equivalent to these ones that avoid the calculation of inverse matrix. Theory ensures that these new equations lead to the same result, but they are more robust from a numerical and computational point of view:

i. $\beta_{k-1} = 1 + \boldsymbol{\varphi}_k^T \boldsymbol{V}_{k-1} \boldsymbol{\varphi}_k$;

ii. $\boldsymbol{V}_k = \boldsymbol{V}_{k-1} - \beta_{k-1}^{-1} \boldsymbol{V}_{k-1} \boldsymbol{\varphi}_k \boldsymbol{\varphi}_k^T \boldsymbol{V}_{k-1}$;

iii. $\varepsilon_k = y_k - \boldsymbol{\varphi}_k^T \hat{\boldsymbol{\vartheta}}_{k-1}$;

iv. $\boldsymbol{K}_k = \boldsymbol{V}_k \boldsymbol{\varphi}_k$;

v. $\hat{\boldsymbol{\vartheta}}_k = \hat{\boldsymbol{\vartheta}}_{k-1} + \boldsymbol{K}_k \varepsilon_k$.

Where the matrix V and the vector $\hat{\boldsymbol{\vartheta}}$ can be initialised with

$$\begin{aligned} \boldsymbol{V}_0 &= \alpha \boldsymbol{I}, \quad \alpha > 0 \\ \hat{\boldsymbol{\vartheta}}_0 &= \boldsymbol{0}. \end{aligned}$$

In some special cases, it is useful to introduce a *forgetting factor* $\mu \in (0; 1]$ (FF), that is a coefficient that allows the recursive least squares method to be less influenced by the older data. Additional information about forgetting factor RLS can be found in many handbooks or manuals, e.g. see [57] or [10]. The forgetting factor makes the estimation more "nervous", indeed it is more influenced by the recent acquisitions and it forces the algorithm to "forget" the older data. Defining the cost function in correspondence of the k-th step as

$$J_k(\boldsymbol{\vartheta}) = \frac{1}{N} \sum_{i=1}^{k} \mu^{k-i} (y_i - \boldsymbol{\varphi}_i^T \boldsymbol{\vartheta})^2, \quad \mu \in (0; 1]. \tag{B.6}$$

The weighting factor μ^{k-i} reduces the influence of older errors on the estimation.

The coefficient that minimises the cost function J_k can be achieved with these recursive equations:

i. $\beta_{k-1} = \mu + \boldsymbol{\varphi}_k^T \boldsymbol{V}_{k-1} \boldsymbol{\varphi}_k$;

ii. $\boldsymbol{V}_k = \mu^{-1}(\boldsymbol{V}_{k-1} - \beta_{k-1}^{-1} \boldsymbol{V}_{k-1} \boldsymbol{\varphi}_k \boldsymbol{\varphi}_k^T \boldsymbol{V}_{k-1})$;

iii. $\varepsilon_k = y_k - \boldsymbol{\varphi}_k^T \hat{\boldsymbol{\vartheta}}_{k-1}$;

iv. $\boldsymbol{K}_k = \boldsymbol{V}_k \boldsymbol{\varphi}_k$;

v. $\hat{\boldsymbol{\vartheta}}_k = \hat{\boldsymbol{\vartheta}}_{k-1} + \boldsymbol{K}_k \varepsilon_k$.

On the contrary, if it is necessary to smooth the coefficient estimation, a low-pass solution can be adopted. In practice, the coefficient vector $\hat{\boldsymbol{\vartheta}}_k$ is estimated in the same way, but the final estimation is

$$\tilde{\boldsymbol{\vartheta}}_k = (1 - \lambda)\hat{\boldsymbol{\vartheta}}_{k-1} + \lambda \hat{\boldsymbol{\vartheta}}_k, \tag{B.7}$$

where $\lambda \in [0; 1]$. The lower λ the higher the low pass effect.

Appendix C

Kalman Filter

This appendix provides a panoramic on Kalman Filter (KF), however further details can be retrieved in many academic handbooks or articles, e.g. see [51], [88], [35] and [22].

C.1 Kalman filtering: linear quadratic estimation (LQE)

A discrete-time stochastic process Σ can be described by the system shown in (C.1)

$$\Sigma : \begin{cases} \boldsymbol{x}_{k+1} = \boldsymbol{f}_k(\boldsymbol{x}_k, \boldsymbol{u}_k, \boldsymbol{w}_k) \\ \boldsymbol{y}_k = \boldsymbol{h}_k(\boldsymbol{x}_k, \boldsymbol{\eta}_k) \end{cases} \tag{C.1}$$

where $\boldsymbol{x}_k$ and $\boldsymbol{u}_k$ are respectively the state and the input at time T_k, $\boldsymbol{f}(\cdot)$ is the function that describes the evolution of the state, $\boldsymbol{h}(\cdot)$ is the observation function and $\boldsymbol{w}_k$ and $\boldsymbol{\eta}_k$ are the process and the observation noises.

If the process and the observation equations are linear equations both with respect to the state $\boldsymbol{x}_k$, the input $\boldsymbol{u}_k$ and the noises, then the process

Σ becomes:

$$\Sigma : \begin{cases} \boldsymbol{x}_{k+1} = \boldsymbol{A}_k \boldsymbol{x}_k + \boldsymbol{B}_k \boldsymbol{u}_k + \boldsymbol{D}_k \boldsymbol{w}_k \\ \boldsymbol{y}_k = \boldsymbol{C}_k \boldsymbol{x}_k + \boldsymbol{\eta}_k \end{cases} \tag{C.2}$$

In the Kalman Filter theory, in addition to the linearity of the process, there are also other fundamental assumptions:

- $\boldsymbol{w}_k$ and $\boldsymbol{\eta}_k$ have to be white noises with covariance matrices equal to $\boldsymbol{Q}_k$ and $\boldsymbol{R}_k$ and expected value $\mathbf{0}$. This means that

  $$\begin{cases} E\{\boldsymbol{w}_k] = \mathbf{0} \\ E[\boldsymbol{w}_k \boldsymbol{w}_i^T] = \boldsymbol{Q}_k \delta_{k-i} \end{cases}, \begin{cases} E[\boldsymbol{\eta}_k] = \mathbf{0} \\ E[\boldsymbol{\eta}_k \boldsymbol{\eta}_i^T] = \boldsymbol{R}_k \delta_{k-i} \end{cases} \quad \forall k, i \in \mathbb{Z}$$

  where δ_{k-i} is equal to 1 if $k = i$ and equal to 0 in all the other cases. These conditions are usually abbreviated as

  $$\boldsymbol{w}_k \sim wn(\mathbf{0}, \boldsymbol{Q}_k) \qquad \boldsymbol{\eta}_k \sim wn(\mathbf{0}, \boldsymbol{R}_k)$$

- $\boldsymbol{w}_k \perp \boldsymbol{\eta}_k$, so $\boldsymbol{w}_k$ and $\boldsymbol{\eta}_k$ have to be uncorrelated between each other;

  $$E[\boldsymbol{w}_k \boldsymbol{\eta}_i^T] = \mathbf{0} \quad \forall k, i \in \mathbb{Z}$$

- the initial state $\boldsymbol{x}_0$ has to be a stochastic variable with expected value $\hat{\boldsymbol{x}}_0$ and covariance matrix $\boldsymbol{P}_0$;

  $$E[\boldsymbol{x}_0] = \hat{\boldsymbol{x}}_0 \qquad E[\boldsymbol{x}_0 \boldsymbol{x}_0^T] = \boldsymbol{P}_0$$

- $\boldsymbol{x}_0 \perp \boldsymbol{w}_k$ and $\boldsymbol{x}_0 \perp \boldsymbol{\eta}_k$, so the initial state $\boldsymbol{x}_0$ has to be uncorrelated with $\boldsymbol{w}_k$ and $\boldsymbol{\eta}_k$

  $$E[\boldsymbol{x}_0 \boldsymbol{\eta}_k^T] = \mathbf{0}, \quad E[\boldsymbol{x}_0 \boldsymbol{w}_k^T] = \mathbf{0} \quad \forall k \in \mathbb{Z}.$$

These last assumptions can be summarised in this way:

$$\begin{cases} E\begin{bmatrix} \boldsymbol{x}_0 \\ \boldsymbol{w}_k \\ \boldsymbol{\eta}_k \end{bmatrix} = \begin{bmatrix} \hat{\boldsymbol{x}}_0 \\ \boldsymbol{0} \\ \boldsymbol{0} \end{bmatrix}, \quad \forall k \in \mathbb{Z} \\ E\begin{bmatrix} \boldsymbol{x}_0 \\ \boldsymbol{w}_k \\ \boldsymbol{\eta}_k \end{bmatrix} \begin{bmatrix} \boldsymbol{x}_0^T & \boldsymbol{w}_i^T & \boldsymbol{\eta}_i^T \end{bmatrix} = \begin{bmatrix} \boldsymbol{P}_0 & \boldsymbol{0} & \boldsymbol{0} \\ \boldsymbol{0} & \boldsymbol{Q}_k\delta_{k-i} & \boldsymbol{0} \\ \boldsymbol{0} & \boldsymbol{0} & \boldsymbol{R}_k\delta_{k-i} \end{bmatrix}, \quad \forall k, i \in \mathbb{Z} \end{cases} \tag{C.3}$$

Defining $\hat{\boldsymbol{x}}_k$ as the estimation of the state at k-th step, the estimation error can be written as

$$\tilde{\boldsymbol{x}}_k = \boldsymbol{x}_k - \hat{\boldsymbol{x}}_k. \tag{C.4}$$

The idea of the Kalman Filter is to look for the estimation of the state that in correspondence of each step minimises the *Mean Square Error* (MSE)

$$E[(\boldsymbol{x}_k - \hat{\boldsymbol{x}}_k)(\boldsymbol{x}_k - \hat{\boldsymbol{x}}_k)^T] = E[\tilde{\boldsymbol{x}}_k\tilde{\boldsymbol{x}}_k^T].$$

The previous mean square error is equal to the covariance matrix of the state in the k-th step, that is $\boldsymbol{P}_k = E[\tilde{\boldsymbol{x}}_k\tilde{\boldsymbol{x}}_k^T]$. Considering the state observer

$$\hat{\boldsymbol{x}}_{k+1} = \boldsymbol{A}_k\hat{\boldsymbol{x}}_k + \boldsymbol{B}_k\boldsymbol{u}_k + \boldsymbol{K}_k(\boldsymbol{y}_k - \boldsymbol{C}_k\hat{\boldsymbol{x}}_k)$$

and using the definition given in (C.4) it is possible to find out the value of $\boldsymbol{K}_k$ that minimises $\boldsymbol{P}_k\,\forall k$. Indeed it is correct to write

$$\begin{aligned} \tilde{\boldsymbol{x}}_{k+1} = \boldsymbol{x}_{k+1} - \hat{\boldsymbol{x}}_{k+1} = \boldsymbol{A}_k\boldsymbol{x}_k + \boldsymbol{B}_k\boldsymbol{u}_k + \boldsymbol{D}_k\boldsymbol{w}_k - \boldsymbol{A}_k\hat{\boldsymbol{x}}_k + \\ - \boldsymbol{B}_k\boldsymbol{u}_k - \boldsymbol{K}_k(\boldsymbol{y}_k - \boldsymbol{C}_k\hat{\boldsymbol{x}}_k) \end{aligned}$$

and since $\boldsymbol{y}_k = \boldsymbol{C}_k\boldsymbol{x}_k + \boldsymbol{\eta}_k$, it yields

$$\tilde{\boldsymbol{x}}_{k+1} = \big(\boldsymbol{A}_k - \boldsymbol{K}_k\boldsymbol{C}_k\big)\tilde{\boldsymbol{x}}_k + \boldsymbol{D}_k\boldsymbol{w}_k - \boldsymbol{K}_k\boldsymbol{\eta}_k.$$

Therefore, the mean square error $\boldsymbol{P}_{k+1}$ can be computed as

$$\begin{aligned} \boldsymbol{P}_{k+1} = E[\tilde{\boldsymbol{x}}_{k+1}\tilde{\boldsymbol{x}}_{k+1}^T] = E[\big(\boldsymbol{A}_k - \boldsymbol{K}_k\boldsymbol{C}_k\big)\tilde{\boldsymbol{x}}_k\tilde{\boldsymbol{x}}_k^T\big(\boldsymbol{A}_k - \boldsymbol{K}_k\boldsymbol{C}_k\big)^T] + \\ + E[\boldsymbol{D}_k\boldsymbol{w}_k\boldsymbol{w}_k^T\boldsymbol{D}_k^T] + E[\boldsymbol{K}_k\boldsymbol{\eta}_k\boldsymbol{\eta}_k^T\boldsymbol{K}_k^T] \end{aligned}$$

where the last equality is due to the fact that the variables are uncorrelated, so the covariance of the sum is equal to the sum of the single covariances. Therefore $\boldsymbol{P}_{k+1}$ is given by

$$\boldsymbol{P}_{k+1} = \big(\boldsymbol{A}_k - \boldsymbol{K}_k\boldsymbol{C}_k\big)\boldsymbol{P}_k\big(\boldsymbol{A}_k - \boldsymbol{K}_k\boldsymbol{C}_k\big)^T + \boldsymbol{D}_k\boldsymbol{Q}_k\boldsymbol{D}_k^T + \boldsymbol{K}_k\boldsymbol{R}_k\boldsymbol{K}_k^T.$$

As mentioned before $\boldsymbol{K}_k$ has to be computed as

$$\begin{aligned}\boldsymbol{K}_k &= \arg\min_{\boldsymbol{K}}\Big\{\big(\boldsymbol{A}_k - \boldsymbol{K}\boldsymbol{C}_k\big)\boldsymbol{P}_k\big(\boldsymbol{A}_k - \boldsymbol{K}\boldsymbol{C}_k\big)^T + \boldsymbol{D}_k\boldsymbol{Q}_k\boldsymbol{D}_k^T + \boldsymbol{K}\boldsymbol{R}_k\boldsymbol{K}^T\Big\}\\ &= \arg\min_{\boldsymbol{K}}\Big\{\boldsymbol{K}\big(\boldsymbol{R}_k + \boldsymbol{C}_k\boldsymbol{P}_k\boldsymbol{C}_k^T\big)\boldsymbol{K}^T - \boldsymbol{K}\boldsymbol{C}_k\boldsymbol{P}_k\boldsymbol{A}_k^T - \boldsymbol{A}_k\boldsymbol{P}_k\boldsymbol{C}_k^T\boldsymbol{K}^T + \\ &\boldsymbol{A}_k\boldsymbol{P}_k\boldsymbol{A}_k^T + \boldsymbol{D}_k\boldsymbol{Q}_k\boldsymbol{D}_k^T\Big\}.\end{aligned}$$

Defining $\boldsymbol{S}_k \hat{=} \boldsymbol{R}_k + \boldsymbol{C}_k\boldsymbol{P}_k\boldsymbol{C}_k^T$ the previous equation becomes

$$\boldsymbol{K}_k = \arg\min_{\boldsymbol{K}}\Big\{\big(\boldsymbol{K} - \boldsymbol{A}_k\boldsymbol{P}_k\boldsymbol{C}_k^T\boldsymbol{S}_k^{-1}\big)\boldsymbol{S}_k\big(\boldsymbol{K} - \boldsymbol{A}_k\boldsymbol{P}_k\boldsymbol{C}_k^T\boldsymbol{S}_k^{-1}\big)^T + \boldsymbol{M}\Big\}.$$

Where $\boldsymbol{M} = \boldsymbol{A}_k\boldsymbol{P}_k\boldsymbol{A}_k^T + \boldsymbol{D}_k\boldsymbol{Q}_k\boldsymbol{D}_k^T - \boldsymbol{A}_k\boldsymbol{P}_k\boldsymbol{C}_k^T\boldsymbol{S}_k^{-1}\boldsymbol{C}_k\boldsymbol{P}_k\boldsymbol{A}_k^T$ does not depend on $\boldsymbol{K}$, so

$$\boldsymbol{K}_k = \arg\min_{\boldsymbol{K}}\Big\{\big(\boldsymbol{K} - \boldsymbol{A}_k\boldsymbol{P}_k\boldsymbol{C}_k^T\boldsymbol{S}_k^{-1}\big)\boldsymbol{S}_k\big(\boldsymbol{K} - \boldsymbol{A}_k\boldsymbol{P}_k\boldsymbol{C}_k^T\boldsymbol{S}_k^{-1}\big)^T\Big\}.$$

This equation finally leads to

$$\boldsymbol{K}_k = \boldsymbol{A}_k\boldsymbol{P}_k\boldsymbol{C}_k^T\boldsymbol{S}_k^{-1} = \boldsymbol{A}_k\boldsymbol{P}_k\boldsymbol{C}_k^T\big(\boldsymbol{R}_k + \boldsymbol{C}_k\boldsymbol{P}_k\boldsymbol{C}_k^T\big)^{-1}. \tag{C.5}$$

If $\boldsymbol{K}_k$ assumes the value described in (C.5), then $\boldsymbol{P}_{k+1}$ is equal to

$$\begin{aligned}\boldsymbol{P}_{k+1} &= \boldsymbol{A}_k\boldsymbol{P}_k\boldsymbol{A}_k^T + \boldsymbol{D}_k\boldsymbol{Q}_k\boldsymbol{D}_k^T - \boldsymbol{A}_k\boldsymbol{P}_k\boldsymbol{C}_k^T\boldsymbol{S}_k^{-1}\boldsymbol{C}_k\boldsymbol{P}_k\boldsymbol{A}_k^T =\\ &= \boldsymbol{A}_k\boldsymbol{P}_k\boldsymbol{A}_k^T + \boldsymbol{D}_k\boldsymbol{Q}_k\boldsymbol{D}_k^T + \\ &- \boldsymbol{A}_k\boldsymbol{P}_k\boldsymbol{C}_k^T\big(\boldsymbol{R}_k + \boldsymbol{C}_k\boldsymbol{P}_k\boldsymbol{C}_k^T\big)\boldsymbol{C}_k\boldsymbol{P}_k\boldsymbol{A}_k^T.\end{aligned} \tag{C.6}$$

Therefore, the best estimation for $\boldsymbol{x}_{k+1}$ corresponding to $\boldsymbol{P}_{k+1}$ is

$$\begin{aligned}\hat{\boldsymbol{x}}_{k+1} &= \big(\boldsymbol{A}_k - \boldsymbol{K}_k\boldsymbol{C}_k\big)\tilde{\boldsymbol{x}}_k + \boldsymbol{B}_k\boldsymbol{u}_k - \boldsymbol{K}_k\boldsymbol{y}_k =\\ &= \boldsymbol{A}_k\hat{\boldsymbol{x}}_k + \boldsymbol{B}_k\boldsymbol{u}_k + \boldsymbol{K}_k\big(\boldsymbol{y}_k - \boldsymbol{C}_k\hat{\boldsymbol{x}}_k\big).\end{aligned} \tag{C.7}$$

Variable	Meaning
$\hat{\boldsymbol{x}}_{k\|k}$	The updated state estimation at time k given observations up to and including time k
$\boldsymbol{P}_{k\|k}$	The updated error covariance matrix (a measure of the accuracy of the state estimation)
$\hat{\boldsymbol{x}}_{k+1\|k}$	The predicted state estimation at time $k+1$ given observations up to and including time k
$\boldsymbol{P}_{k+1\|k}$	The predicted error covariance matrix

Table C.1: A new notation for the estimated state and its covariance matrix.

It should be noted that $\boldsymbol{K}_k$ can be also expressed as $\boldsymbol{A}_k\boldsymbol{L}_k$ with $\boldsymbol{L}_k = \boldsymbol{P}_k\boldsymbol{C}_k^T\boldsymbol{S}_k^{-1}$. In this way it is possible to divide the whole algorithm in two separated steps: *prediction* and *updating*.

Indeed, introducing the notation reported in table C.1, the (C.7) can be written as

$$\begin{aligned}\hat{\boldsymbol{x}}_{k+1|k} &= \boldsymbol{A}_k\hat{\boldsymbol{x}}_k + \boldsymbol{B}_k\boldsymbol{u}_k + \boldsymbol{K}_k\big(\boldsymbol{y}_k - \boldsymbol{C}_k\hat{\boldsymbol{x}}_k\big) = \\ &= \boldsymbol{A}_k \underbrace{\big(\hat{\boldsymbol{x}}_{k|k-1} + \boldsymbol{L}_k(\boldsymbol{y}_k - \boldsymbol{C}_k\hat{\boldsymbol{x}}_{k|k-1})\big)}_{\hat{\boldsymbol{x}}_{k|k}} + \boldsymbol{B}_k\boldsymbol{u}_k. \end{aligned} \tag{C.8}$$

Similarly, it is possible to separate the calculus of the covariance matrix $\boldsymbol{P}_{k+1}$ in a step of prediction and one step of updating.

$$\begin{aligned}\boldsymbol{P}_{k+1|k} &= \boldsymbol{A}_k\boldsymbol{P}_k\boldsymbol{A}_k^T - \underbrace{\boldsymbol{A}_k\boldsymbol{L}_k}_{\boldsymbol{K}_k}\boldsymbol{S}_k\boldsymbol{L}_k^T\boldsymbol{A}_k^T + \boldsymbol{D}_k\boldsymbol{Q}_k\boldsymbol{D}_k = \\ &= \boldsymbol{A}_k \underbrace{\big[\boldsymbol{P}_{k|k-1} - \boldsymbol{L}_k\boldsymbol{S}_k\boldsymbol{L}_k^T\big]}_{\boldsymbol{P}_{k|k}}\boldsymbol{A}_k^T + \boldsymbol{D}_k\boldsymbol{Q}_k\boldsymbol{D}_k^T. \end{aligned} \tag{C.9}$$

Using (C.8) and (C.9) it is possible to completely define the two steps of prediction and updating as shown in C.2

Updating	**Prediction**
$\hat{\boldsymbol{x}}_{k\|k} = \hat{\boldsymbol{x}}_{k\|k-1} + \boldsymbol{L}_k(\boldsymbol{y}_k - \boldsymbol{C}_k\hat{\boldsymbol{x}}_{k\|k-1})$	$\hat{\boldsymbol{x}}_{k+1\|k} = \boldsymbol{A}_k\hat{\boldsymbol{x}}_{k\|k} + \boldsymbol{B}_k\boldsymbol{u}_k$
$\boldsymbol{P}_{k\|k} = \boldsymbol{P}_{k\|k-1} - \boldsymbol{L}_k\boldsymbol{S}_k\boldsymbol{L}_k$	$\boldsymbol{P}_{k+1\|k} = \boldsymbol{A}_k\boldsymbol{P}_{k\|k}\boldsymbol{A}_k^T + \boldsymbol{D}_k\boldsymbol{Q}_k\boldsymbol{D}_k^T$

Table C.2: Updating and prediction step for the state estimation and its covariance matrix.

Kalman filter algorithm

Therefore, the Kalman filter can be applied to reach the best estimation of the state of the stochastic process Σ following these recursive steps:

1. the first step is necessary to define the initial condition of the state estimation $\hat{\boldsymbol{x}}_{1|0}$ and its covariance matrix $\boldsymbol{P}_{1|0}$;

2. updating steps (for $k = 1, 2, \dots$)

$$\begin{aligned}
\boldsymbol{S}_k &= \boldsymbol{R}_k + \boldsymbol{C}_k\boldsymbol{P}_{k|k-1}\boldsymbol{C}_k^T;\\
\boldsymbol{L}_k &= \boldsymbol{P}_{k|k-1}\boldsymbol{C}_k^T\boldsymbol{S}_k^{-1};\\
\boldsymbol{e}_k &= \boldsymbol{y}_k - \boldsymbol{C}_k\hat{\boldsymbol{x}}_{k|k-1};\\
\hat{\boldsymbol{x}}_{k|k} &= \hat{\boldsymbol{x}}_{k|k-1} + \boldsymbol{L}_k\boldsymbol{e}_k;\\
\boldsymbol{P}_{k|k} &= \big(\boldsymbol{I} - \boldsymbol{L}_k\boldsymbol{C}_k\big)\boldsymbol{P}_{k|k-1}\big(\boldsymbol{I} - \boldsymbol{L}_k\boldsymbol{C}_k\big)^T + \boldsymbol{L}_k\boldsymbol{R}_k\boldsymbol{L}_k^T.
\end{aligned}$$

   Where the last equation for $\boldsymbol{P}_{k|k}$ is equivalent to the previous one, even if this formulation is more robust for practical implementation;

3. prediction steps (for $k = 1, 2, \dots$)

$$\begin{aligned}
\hat{\boldsymbol{x}}_{k+1|k} &= \boldsymbol{A}_k\hat{\boldsymbol{x}}_{k|k} + \boldsymbol{B}_k\boldsymbol{u}_k;\\
\boldsymbol{P}_{k+1|k} &= \boldsymbol{A}_k\boldsymbol{P}_{k|k}\boldsymbol{A}_k^T + \boldsymbol{D}_k\boldsymbol{Q}_k\boldsymbol{D}_k^T.
\end{aligned}$$

Even in the case where the process Σ is stationary ($\boldsymbol{A}_k = \boldsymbol{A}$, $\boldsymbol{B}_k = \boldsymbol{B}$, $\boldsymbol{C}_k = \boldsymbol{C}$, $\boldsymbol{D}_k = \boldsymbol{D}$, $\boldsymbol{Q}_k = \boldsymbol{Q}$, $\boldsymbol{R}_k = \boldsymbol{R}$), the Kalman gain $\boldsymbol{K}_k$ is not constant, indeed it would be equal to

$$\boldsymbol{K}_k = \boldsymbol{A}\boldsymbol{P}_k\boldsymbol{C}^T\big(\boldsymbol{R} + \boldsymbol{C}\boldsymbol{P}_k\boldsymbol{C}^T\big)^{-1}. \tag{C.10}$$

To reach the optimal constant value for the Kalman gain $\boldsymbol{K}$ it is necessary to introduce without demonstration that, under suitable hypothesis, a solution to the *Algebraic Riccati Equation* is

$$\boldsymbol{P} = \boldsymbol{A}^T\boldsymbol{P}\boldsymbol{A} - \boldsymbol{A}^T\boldsymbol{P}\boldsymbol{B}(\boldsymbol{R} + \boldsymbol{B}^T\boldsymbol{P}\boldsymbol{B})^{-1}\boldsymbol{B}^T\boldsymbol{P}\boldsymbol{A} + \boldsymbol{Q}$$

such that

$$\lim_{t\to\infty} \boldsymbol{P}_k = \boldsymbol{P} \quad \forall\, \boldsymbol{P}_0.$$

It is possible to demonstrate that the observer with Kalman gain equal to

$$\boldsymbol{K} = \boldsymbol{A}\boldsymbol{P}\boldsymbol{C}^T\left(\boldsymbol{R} + \boldsymbol{C}\boldsymbol{P}\boldsymbol{C}^T\right)^{-1} \tag{C.11}$$

is the optimal observer with constant gain.

C.2 Approximated Kalman filter algorithm for non-linear process

The classic Kalman filter algorithm has many assumptions. Some of these assumptions, such as that the noises have to be zero-mean white noise mutually uncorrelated, can be relaxed changing the system. However the strongest assumption is that the process Σ has to be linear. If Σ is not linear there are many approximated methods that attempt to find the best estimation of the state $\boldsymbol{x}_k$ $\forall k \in \mathbb{Z}$. Some of the most important methods are:

- Extended Kalman filter (EKF);
- Unscented Kalman filter (UKF);
- Particle filter (PF).

In the next paragraph the Extended Kalman filter (EKF) will be presented.

C.2.1 Extended Kalman filter (EKF)

This method considers a linear approximation of the process Σ around the estimations of the state in order to transform the complete process Σ in a

linear process $\overline{\Sigma}$ which can be used in a classic Kalman filter. Let's consider a non-linear process Σ with additive noises such as

$$\Sigma : \begin{cases} \boldsymbol{x}_{k+1} = \boldsymbol{f}_k(\boldsymbol{x}_k, \boldsymbol{u}_k) + \boldsymbol{w}_k \\ \boldsymbol{y}_k = \boldsymbol{h}_k(\boldsymbol{x}_k) + \boldsymbol{\eta}_k \end{cases}$$

Moreover, concerning the updating steps, let consider the Taylor series of the function $\boldsymbol{h}_k(\cdot)$ around the state estimation $\hat{\boldsymbol{x}}_{k|k-1}$

$$\begin{aligned} \boldsymbol{h}_k(\boldsymbol{x}_k) &= \boldsymbol{h}_k(\hat{\boldsymbol{x}}_{k|k-1}) + \frac{\partial \boldsymbol{h}_k}{\partial \boldsymbol{x}_k}(\hat{\boldsymbol{x}}_{k|k-1})(\boldsymbol{x}_k - \hat{\boldsymbol{x}}_{k|k-1}) + \cdots \simeq \\ &\simeq \boldsymbol{h}_k(\hat{\boldsymbol{x}}_{k|k-1}) + \boldsymbol{C}_k(\boldsymbol{x}_k - \hat{\boldsymbol{x}}_{k|k-1}) \end{aligned}$$

where

$$\boldsymbol{C}_k = \frac{\partial \boldsymbol{h}_k}{\partial \boldsymbol{x}_k}(\hat{\boldsymbol{x}}_{k|k-1}). \tag{C.12}$$

In addition to this, concerning the prediction steps, let's consider the Taylor series of the function $\boldsymbol{f}_k(\cdot)$ in the neighbourhood of the state estimation $\hat{\boldsymbol{x}}_{k|k}$

$$\begin{aligned} \boldsymbol{f}_k(\boldsymbol{x}_k) &= \boldsymbol{f}_k(\hat{\boldsymbol{x}}_{k|k}) + \frac{\partial \boldsymbol{f}_k}{\partial \boldsymbol{x}_k}(\hat{\boldsymbol{x}}_{k|k})(\boldsymbol{x}_k - \hat{\boldsymbol{x}}_{k|k}) + \cdots \simeq \\ &\simeq \boldsymbol{f}_k(\hat{\boldsymbol{x}}_{k|k}) + \boldsymbol{A}_k(\boldsymbol{x}_k - \hat{\boldsymbol{x}}_{k|k}) \end{aligned}$$

where

$$\boldsymbol{A}_k = \frac{\partial \boldsymbol{f}_k}{\partial \boldsymbol{x}_k}(\hat{\boldsymbol{x}}_{k|k}). \tag{C.13}$$

Once introduced these approximations, it is possible to define the EKF algorithm suitable for all the non-linear process:

1. The first step is necessary to define the initial condition of the state estimation $\hat{\boldsymbol{x}}_{1|0}$ and his covariance matrix $\boldsymbol{P}_{1|0}$. This algorithm does not provide any guarantee of convergence, the only way to be quite sure of reaching the convergence to the real state is to choose an initial estimation as close as possible to the real one;

2. updating steps (for $k = 1, 2, \dots$)

$$\begin{aligned}
\boldsymbol{S}_k &= \boldsymbol{R}_k + \boldsymbol{C}_k \boldsymbol{P}_{k|k-1} \boldsymbol{C}_k^T; \\
\boldsymbol{L}_k &= \boldsymbol{P}_{k|k-1} \boldsymbol{C}_k^T \boldsymbol{S}_k^{-1}; \\
\boldsymbol{e}_k &= \boldsymbol{y}_k - \boldsymbol{h}_k(\hat{\boldsymbol{x}}_{k|k-1}); \\
\hat{\boldsymbol{x}}_{k|k} &= \hat{\boldsymbol{x}}_{k|k-1} + \boldsymbol{L}_k \boldsymbol{e}_k; \\
\boldsymbol{P}_{k|k} &= \big(\boldsymbol{I} - \boldsymbol{L}_k \boldsymbol{C}_k\big) \boldsymbol{P}_{k|k-1} \big(\boldsymbol{I} - \boldsymbol{L}_k \boldsymbol{C}_k\big)^T + \boldsymbol{L}_k \boldsymbol{R}_k \boldsymbol{L}_k^T .
\end{aligned}$$

3. prediction steps (for $k = 1, 2, \dots$)

$$\begin{aligned}
\hat{\boldsymbol{x}}_{k+1|k} &= \boldsymbol{f}_k(\hat{\boldsymbol{x}}_{k|k}); \\
\boldsymbol{P}_{k+1|k} &= \boldsymbol{A}_k \boldsymbol{P}_{k|k} \boldsymbol{A}_k^T + \boldsymbol{Q}_k^T .
\end{aligned}$$

where the last equation is due to the fact that $\boldsymbol{D}_k = 1$.

Appendix D

Publications

International Journals

1. M. Basso, **M. Galanti**, G. Innocenti and D. Miceli, *Pedestrian Dead Reckoning Based on Frequency Self-Synchronization and Body Kinematics*, *IEEE Sensors Journal*, vol. 17 , no. 2, pp. 534–545, Jan 2017.

   URL: `http://ieeexplore.ieee.org/stamp/stamp.jsp?tp=&arnumber=7752792&isnumber=7792229`

   [DOI:10.1109/JSEN.2016.2631629]

Submitted

1. M. Basso, **Matteo Galanti**, G. Innocenti and D. Miceli.

   Provisional paper title: *Triggered INS/GNSS data fusion algorithms for enhanced pedestrian navigation system*, *IEEE Sensors Journal*, 2018.

To be submitted

1. L. Alessandrini, M. Basso, **Matteo Galanti**, G. Innocenti, L. Giovanardi and L. Pretini.

   Provisional paper title: *Maximum likelihood virtual firing temperature from a thermodynamic internal model of a twin-shaft aeroderivative gas turbine*, *Control System Technology*, 2018.

Domestic Conferences

1. **M. Galanti**, M. Basso, G. Innocenti. "*Pedestrian dead-reckoning based on frequency self-synchronization and body kinematics*", in *SIDRA, Automatica.it 2018*, Firenze (Italy), 12-14 Settembre 2018.

List of Figures

List of Tables

Bibliography

[1] T. Addabbo, R. Biondi, S. Cioncolini, A. Fort, F. Rossetti, and V. Vignoli, "A zero-crossing detection system based on FPGA to measure the angular vibrations of rotating shafts," *IEEE Transactions on Instrumentation and Measurement*, vol. 63, no. 12, pp. 3002–3010, Dec 2014.

[2] T. Addabbo, A. Fort, R. Biondi, S. Cioncolini, M. Mugnaini, S. Rocchi, and V. Vignoli, "Measurement of angular vibrations in rotating shafts: Effects of the measurement setup nonidealities," *IEEE Transactions on Instrumentation and Measurement*, vol. 62, no. 3, pp. 532–543, March 2013.

[3] R. Adhami, P. Meenen, and D. Hite, *Fundamental Concepts in Electrical and Computer Engineering with Practical Design Problems*. Universal Publishers, 2007. [Online]. Available: https://books.google.it/books?id=9nqkVbFPutYC

[4] K. H. Ang, G. Chong, and Y. Li, "Pid control system analysis, design, and technology," *IEEE Transactions on Control Systems Technology*, vol. 13, no. 4, pp. 559–576, July 2005.

[5] J. Angeles, *Dynamic Response of Linear Mechanical Systems: Modeling, Analysis and Simulation*, ser. Mechanical Engineering Series. Springer US, 2011. [Online]. Available: https://books.google.ch/books?id=kn7p65y3uwUC

[6] M. Antonova, E. Vasilieva, and I. Zhezhera, "The antisurge protection of a centrifugal compressor," in *2017 International Conference on Modern Electrical and Energy Systems (MEES)*, Nov 2017, pp. 80–83.

[7] G. Baldini, S. Bittanti, A. D. Marco, F. Longhi, G. Poncia, W. Prandoni, and D. Vettorello, "A dynamic model of moving flames for the analysis and

control of combustion instabilities," in *1999 European Control Conference (ECC)*, Aug 1999, pp. 2795–2800.

[8] A. Banaszuk, Y. Zhang, and C. A. Jacobson, "Adaptive control of combustion instability using extremum-seeking," in *Proceedings of the 2000 American Control Conference. ACC (IEEE Cat. No.00CH36334)*, vol. 1, no. 6, June 2000, pp. 416–422 vol.1.

[9] M. Bandyopadhyay, *Electrical power system: Theory and Practice*, ser. Eastern Economy Edition. PHI Learning, 2006. [Online]. Available: https://books.google.it/books?id=lrQJ_kzGapUC

[10] C. Banyasz, *Adaptive Systems in Control and Signal Processing 1995*, ser. IFAC Postprint Volume. Elsevier Science, 2014. [Online]. Available: https://books.google.ch/books?id=g9HSBQAAQBAJ

[11] R. Bazyar, M. R. Javadi, A. Ghasemi, and A. Yusefi, "Analysis and study subsynchronous resonance (SSR) in tabriz thermal power plant using thyristor controlled series compensator," in *The 3rd Conference on Thermal Power Plants*, Oct 2011, pp. 1–5.

[12] K. Belmokhtar, H. Ibrahim, and A. Merabet, "Online parameter identification for a dfig driven wind turbine generator based on recursive least squares algorithm," in *2015 IEEE 28th Canadian Conference on Electrical and Computer Engineering (CCECE)*, May 2015, pp. 965–969.

[13] C. Bitikofer, M. P. Schoen, J. Li, and F. Lin, "Characteristic moore-greitzer model parameter identification for a one stage axial compressor system," in *2017 American Control Conference (ACC)*, May 2017, pp. 164–169.

[14] M. Boles and D. Yunus A. Cengel, *Thermodynamics: An Engineering Approach*. McGraw-Hill Education, 2014. [Online]. Available: https://books.google.it/books?id=Ao95ngEACAAJ

[15] S. Borguet and O. Léonard, "Comparison of adaptive filters for gas turbine performance monitoring," *Journal of Computational and Applied Mathematics*, vol. 234, no. 7, pp. 2202 – 2212, 2010, fourth International Conference on Advanced COmputational Methods in ENgineering (ACOMEN 2008). [Online]. Available: http://www.sciencedirect.com/science/article/pii/S0377042709005561

[16] M. Boyce, *Gas Turbine Engineering Handbook*. Elsevier Science, 2017. [Online]. Available: https://books.google.it/books?id=zPAFHyHctRUC

[17] B. J. Brunell, R. R. Bitmead, and A. J. Connolly, "Nonlinear model predictive control of an aircraft gas turbine engine," in *Proceedings of the 41st IEEE Conference on Decision and Control, 2002.*, vol. 4, Dec 2002, pp. 4649–4651 vol.4.

[18] F. Caifen, T. Wen, and L. Jizhen, "Imc control of combustion instability," in *2008 27th Chinese Control Conference*, July 2008, pp. 39–43.

[19] D. Childs and D. Childs, *Turbomachinery Rotordynamics: Phenomena, Modeling, and Analysis*, ser. Wiley-Interscience publication. Wiley, 1993. [Online]. Available: https://books.google.it/books?id=vKPfBxgQQPoC

[20] J. Chin and J. Csank, "Tool for the Integrated Dynamic Numerical Propulsion System Simulation (NPSS)/Turbine Engine Closed-Loop Transient Analysis (TTECTrA)," National Aeronautics and Space Administration (NASA), Glenn Research Center, Tech. Rep., 2016.

[21] F. Chu, B. Dai, W. Dai, R. Jia, X. Ma, and F. Wang, "Rapid modeling method for performance prediction of centrifugal compressor based on model migration and SVM," *IEEE Access*, vol. 5, pp. 21 488–21 496, 2017.

[22] C. K. Chui and G. Chen, *Kalman Filtering with Real-time Applications*. Berlin, Heidelberg: Springer Verlag, 1987.

[23] T. A. Clifford, S. Cruz-Manzo, Y. Zhang, V. Panov, and A. Latimer, "Development of a steady-state thermodynamic model in microsoft excel for performance analysis of industrial gas turbines," in *IECON 2017 - 43rd Annual Conference of the IEEE Industrial Electronics Society*, Oct 2017, pp. 4717–4723.

[24] H. Cohen, G. Rogers, P. Straznicky, H. Saravanamuttoo, and A. Nix, *Gas Turbine Theory*. Pearson Education Limited, 2017. [Online]. Available: https://books.google.it/books?id=hvEmDwAAQBAJ

[25] M. Dapor and M. Ropele, *Elaborazione dei dati sperimentali*, ser. UNITEXT. Springer Milan, 2006. [Online]. Available: https://books.google.ch/books?id=8RpLiEzqxRIC

[26] N. Daroogheh, N. Meskin, and K. Khorasani, "Ensemble kalman filters for state estimation and prediction of two-time scale nonlinear systems with

application to gas turbine engines," *IEEE Transactions on Control Systems Technology*, pp. 1–9, 2018.

[27] A. Ferrero, *Esposizione del Metodo dei Minimi Quadrati (Classic Reprint)*. Fb&c Limited, 2018. [Online]. Available: https://books.google.ch/books?id=FmFRswEACAAJ

[28] D. Fontaine, S. Liao, J. Paduano, and P. V. Kokotovic, "Nonlinear control experiments on an axial flow compressor," *IEEE Transactions on Control Systems Technology*, vol. 12, no. 5, pp. 683–693, Sept 2004.

[29] *LM2500 - Marine Gas Turbine*, GE Aviation, 2 2017. [Online]. Available: https://www.geaviation.com/sites/default/files/datasheet-lm2500.pdf

[30] *LM2500+ - Marine Gas Turbine*, GE Aviation, 2 2017. [Online]. Available: https://www.geaviation.com/sites/default/files/datasheet-lm2500plus.pdf

[31] *LM2500+G4 - Marine Gas Turbine*, GE Aviation, 2 2017. [Online]. Available: https://www.geaviation.com/sites/default/files/datasheet-lm2500plusg4.pdf

[32] T. Giampaolo, *Gas Turbine Handbook: Principles and Practice*. Fairmont Press, 2009. [Online]. Available: https://books.google.it/books?id=WbzGUYJEmdUC

[33] T. Goodman, "A least-squares method for computing balance corrections," *Journal of Engineering for Industry*, vol. 86, pp. 273–277, 1964.

[34] J. T. Gravdahl and O. Egeland, "A moore-greitzer axial compressor model with spool dynamics," in *Proceedings of the 36th IEEE Conference on Decision and Control*, vol. 5, Dec 1997, pp. 4714–4719 vol.5.

[35] M. S. Grewal and A. P. Andrews, *Kalman Filtering: Theory and Practice with MATLAB*, 4th ed. Wiley IEEE Press, 2014.

[36] G. Gu, S. Banda, and A. Sparks, "An overview of rotating stall and surge control for axial flow compressors," in *Proceedings of 35th IEEE Conference on Decision and Control*, vol. 3, Dec 1996, pp. 2786–2791 vol.3.

[37] D. H. Cooke, "On Prediction of Off Design Multistage Turbine Pressures by Stodola's Ellipse," vol. 107, 07 1985.

[38] W. M. Haddad, A. Leonessa, V. S. Chellaboina, and J. L. Fausz, "Nonlinear robust disturbance rejection controllers for rotating stall and surge in

axial flow compressors," *IEEE Transactions on Control Systems Technology*, vol. 7, no. 3, pp. 391–398, May 1999.

[39] C. Hall and S. Dixon, *Fluid Mechanics and Thermodynamics of Turbomachinery*. Elsevier Science, 2013. [Online]. Available: https://books.google.it/books?id=wZoTAAAAQBAJ

[40] H. Hanachi, J. Liu, A. Banerjee, Y. Chen, and A. Koul, "A physics-based modeling approach for performance monitoring in gas turbine engines," *IEEE Transactions on Reliability*, vol. 64, no. 1, pp. 197–205, March 2015.

[41] L. Harnefors, "Analysis of subsynchronous torsional interaction with power electronic converters," *IEEE Transactions on Power Systems*, vol. 22, no. 1, pp. 305–313, Feb 2007.

[42] M. Hayes, *Statistical Digital Signal Processing and Modeling*. Wiley India Pvt. Limited, 2009. [Online]. Available: https://books.google.ch/books?id=z0GqhOe9GNQC

[43] J. V. Helvoirt, "Centrifugal compressor surge: Modeling and identification for control," Ph.D. dissertation, Technische Universiteit Eindhoven, 2007.

[44] F. Iliceto, *Impianti elettrici*, ser. Impianti elettrici. Pàtron, 1984, no. Bd. 1. [Online]. Available: https://books.google.it/books?id=Uf2YPQAACAAJ

[45] M. R. Iravani, B. L. Agrawal, D. H. Baker, C. E. J. Bowler, R. G. Farmer, R. A. Hedin, E. H. V. Larsen, and J. F. Tang, "Fourth supplement to a bibliography for the study of subsynchronous resonance between rotating machines and power systems," *IEEE Transactions on Power Systems*, vol. 12, no. 3, pp. 1276–1282, Aug 1997.

[46] G. D. Jennings, R. Harley, and B. S. Rigby, "Modal parameters and turbogenerator torsional behavior," in *3D Africon Conference. Africon '92 Proceedings (Cat. No.92CH3215)*, Sept 1992, pp. 517–520.

[47] Z. Jian, H. K. Mathews, P. G. Bonanni, and S. Ruijie, "Model-based sensor fault detection and isolation in gas turbine," in *Proceedings of the 31st Chinese Control Conference*, July 2012, pp. 5215–5218.

[48] M. Johnson and M. Moradi, *PID Control: New Identification and Design Methods*, ser. Probability and its applications. Springer London, 2006. [Online]. Available: https://books.google.ch/books?id=hY6oLlqLCv8C

[49] S. Jones, "An Introduction to Thermodynamic Performance Analysis of Aircraft Gas Turbine Engine Cycles Using the Numerical Propulsion System Simulation Code," National Aeronautics and Space Administration (NASA), Glenn Research Center, Tech. Rep., 2007.

[50] F. Jurado, N. Acero, and A. Echarri, "Enhancing the electric system stability using predictive control of gas turbines," in *2006 Canadian Conference on Electrical and Computer Engineering*, May 2006, pp. 438–441.

[51] R. E. Kalman, "A New Approach to Linear Filtering and Prediction Problems," *Transactions of the ASME, Journal of Basic Engineering*, no. 82 (Series D), pp. 35–45, 1960. [Online]. Available: http://www.cs.unc.edu/~welch/kalman/media/pdf/Kalman1960.pdf

[52] C. Kasemann, L. van Lieshout, M. Huart, and M. Rott, "10MVA thyristor converters for the active damping of generator shaft oscillations at ASDEX upgrade," *Fusion Engineering and Design*, vol. 84, no. 2, pp. 998 – 1001, 2009, proceeding of the 25th Symposium on Fusion Technology. [Online]. Available: http://www.sciencedirect.com/science/article/pii/S0920379608004924

[53] A. G. Kaviri and M. N. M. Jaafar, "Thermodynamic modeling and exergy optimization of a gas turbine power plant," in *2011 IEEE 3rd International Conference on Communication Software and Networks*, May 2011, pp. 366–370.

[54] R. Khalili and M. Karrari, "Modeling and identification of an industrial gas turbine using classical and non-classical approaches," in *2017 Iranian Conference on Electrical Engineering (ICEE)*, May 2017, pp. 667–672.

[55] D. Klein and C. Abeykoon, "Modelling of a turbojet gas turbine engine," in *2015 Internet Technologies and Applications (ITA)*, Sept 2015, pp. 200–206.

[56] H. Knapp, R. Döring, L. Oellrich, U. Plöcker, J. Prausnitz, R. Langhorst, and Z. R., *Vapor-Liquid Equilibria for Mixtures of Low Boiling Substances*. Chemistry Data Series, 1982.

[57] B. Kovačević, Z. Banjac, and M. Milosavljević, *Adaptive Digital Filters*, ser. SpringerLink : Bücher. Springer Berlin Heidelberg, 2013. [Online]. Available: https://books.google.ch/books?id=LY7PQQGWr1kC

[58] J. Leader, *Numerical Analysis and Scientific Computation*, ser. Featured Titles for Numerical Analysis. Pearson Addison Wesley, 2004. [Online]. Available: https://books.google.ch/books?id=Q7tsNwAACAAJ

[59] G. Li, Z. Lin, C. Untaroiu, and P. E. Allaire, "Balancing of high-speed rotating machinery using convex optimization," in *42nd IEEE International Conference on Decision and Control (IEEE Cat. No.03CH37475)*, vol. 4, Dec 2003, pp. 4351–4356 vol.4.

[60] G. Lin, "Flow meter system error treatment based on iterative learning control," in *2011 Chinese Control and Decision Conference (CCDC)*, May 2011, pp. 3777–3780.

[61] K. H. Ludtke, *Process Centrifugal Compressors*. Springer, 2004.

[62] J. Lytle, "The Numerical Propulsion System Simulation: A Multidisciplinary Design System for Aerospace Vehicles," National Aeronautics and Space Administration (NASA), Glenn Research Center, Tech. Rep., 1999.

[63] C. A. Mansoux, D. L. Gysling, J. D. Setiawan, and J. D. Paduano, "Distributed nonlinear modeling and stability analysis of axial compressor stall and surge," in *Proceedings of 1994 American Control Conference - ACC '94*, vol. 2, June 1994, pp. 2305–2316 vol.2.

[64] K. R. McManus, J. C. Magill, and M. F. Miller, "Control of unstable combustion oscillations in liquid-fueled gas turbines," in *Proceedings of the 1998 IEEE International Conference on Control Applications (Cat. No.98CH36104)*, vol. 2, Sept 1998, pp. 1170–1174 vol.2.

[65] A. Mehta, H. Kaufman, and R. Ravi, "Turbine system identification: experimental results," in *Proceedings of 1994 33rd IEEE Conference on Decision and Control*, vol. 4, Dec 1994, pp. 3593–3595 vol.4.

[66] F. Moore and E. Greitzer, "A theory of post-stall transients in axial compressors: Part I - development of the equations," in *J. Eng.Gas Turbines and Power*, vol. 108, 1986, pp. 68–76 vol.108.

[67] F. Moore and M. Greitzer, "A theory of post-stall transients in axial compressors: Part 2 - application," in *J. Eng.Gas Turbines and Power*, vol. 108, 1986, pp. 231–239 vol.108.

[68] D. Mudroncik, P. Tanuska, and M. Galik, "Surge control of natural gas centrifugal compressor," in *2009 Second International Conference on Computer and Electrical Engineering*, vol. 1, Dec 2009, pp. 110–113.

[69] D. Newland, *Mechanical Vibration Analysis and Computation*, ser. Dover books on engineering. Dover Publications, 2013. [Online]. Available: https://books.google.ch/books?id=LSrEAgAAQBAJ

[70] M. Nieuwenhuizen, J. van Helvoirt, and M. Steinbuch, "An analogy between the Van der Pol equation and the Greitzer model," in *2009 European Control Conference (ECC)*, Aug 2009, pp. 490–495.

[71] D. Niu, A. Shi, Y. Chang, and F. Wang, "Modelling of multistage centrifugal compressor," in *Proceedings of 2011 International Conference on Computer Science and Network Technology*, vol. 2, Dec 2011, pp. 1144–1147.

[72] C. Osnaghi, *Teoria delle turbomacchine*. Esculapio, 2013. [Online]. Available: https://books.google.it/books?id=3cMEAQAAQBAJ

[73] W. Peng, *Fundamentals of Turbomachinery*. Wiley, 2008. [Online]. Available: https://books.google.it/books?id=PEV3570XWR0C

[74] N. Petchers, *Combined Heating, Cooling & Power Handbook: Technologies & Applications : an Integrated Approach to Energy Resource Optimization*. Fairmont Press, 2003. [Online]. Available: https://books.google.it/books?id=hA129h8dc1AC

[75] *PLECS - The simulation platform for power electronic systems*, PLEXIM Electrical Engineering Software, 4 2018, rev. 4.1. [Online]. Available: https://www.plexim.com/download/documentation

[76] M. Plis and H. Rusinowski, "Mathematical modeling of an axial compressor in a gas turbine cycle," *Journal of Power Technologies*, vol. 96, no. 3, pp. 194 – 199, 2016.

[77] B. Pourbabaee, N. Meskin, and K. Khorasani, "Sensor fault detection, isolation, and identification using multiple-model-based hybrid kalman filter for gas turbine engines," *IEEE Transactions on Control Systems Technology*, vol. 24, no. 4, pp. 1184–1200, July 2016.

[78] J. M. Protz and J. D. Paduano, "Rotating stall and surge: alternate modeling and control concepts," in *Proceedings of the 1997 IEEE International Conference on Control Applications*, Oct 1997, pp. 866–873.

[79] S. Purushothaman and F. de Leon, "Eliminating subsynchronous oscillations with an induction machine damping unit (imdu)," *IEEE Transactions on Power Systems*, vol. 26, no. 1, pp. 225–232, Feb 2011.

[80] A. Pytel and Å. Kozḱ, "Modelling and effective predictive control of gas turbine process," in *Proceedings of the 2014 15th International Carpathian Control Conference (ICCC)*, May 2014, pp. 469–474.

[81] W. Qu and J. Jiang, "SSTI and its mitigation in wind farms connected with an HVDC line," *Procedia Computer Science*, vol. 111, pp. 399 – 405, 2017, the 8th International Conference on Advances in Information Technology. [Online]. Available: http://www.sciencedirect.com/science/article/pii/S1877050917312139

[82] W. M. Salim and S. A. Ahmed, "Numerical analysis of free vortex flow in a combustor model," in *2017 7th International Conference on Modeling, Simulation, and Applied Optimization (ICMSAO)*, April 2017, pp. 1–5.

[83] G. C. Sărbu, "Modern water flowmeters: Differential pressure flowmeters," in *2016 International Conference and Exposition on Electrical and Power Engineering (EPE)*, Oct 2016, pp. 609–616.

[84] A. S. Shiriaev, L. B. Freidovich, A. Robertsson, A. Andersson, and R. Johansson, "Sufficient conditions for dynamic stabilization of 3-state Moore-Greitzer compressor model," in *2015 54th IEEE Conference on Decision and Control (CDC)*, Dec 2015, pp. 4394–4399.

[85] C. Sihler and T. Zoller, "Active damping of torsional modes in turbine-generator shafts," 08 2018.

[86] A. Sinha, *Vibration of Mechanical Systems*. Cambridge University Press, 2010. [Online]. Available: https://books.google.ch/books?id=hMPHTFfBt5oC

[87] C. Soares, *Gas Turbines: A Handbook of Air, Land and Sea Applications*. Elsevier Science, 2014. [Online]. Available: https://books.google.it/books?id=ubJZAwAAQBAJ

[88] H. Sorenson, *Kalman Filtering: Theory and Application*, ser. IEEE Press selected reprint series. IEEE Press, 1985. [Online]. Available: https://books.google.it/books?id=2pgeAQAAIAAJ

[89] S. Strogatz, *Nonlinear Dynamics And Chaos*, ser. Studies in nonlinearity. Sarat Book House, 2007. [Online]. Available: https://books.google.ch/books?id=PHmED2xxrE8C

[90] F. Svetti, P. Rotondo, D. Sgró, and F. Meucci, "Practical guidelines for Oil & Gas plant design against sub-synchronous torsional interaction phenomena," *Turbomachinery Laboratories, Texas A&M Engineering Experiment Station*, 2015.

[91] A. Tabesh and R. Iravani, "Frequency-response analysis of torsional dynamics," *IEEE Transactions on Power Systems*, vol. 19, no. 3, pp. 1430–1437, Aug 2004.

[92] N. Thomopoulos, *Statistical Distributions: Applications and Parameter Estimates*. Springer International Publishing, 2017. [Online]. Available: https://books.google.ch/books?id=lng5DwAAQBAJ

[93] Torquemeters Limited, "Continuous duty torque measurement," https://www.torquemeters.com/wp-content/uploads/2013/03/Continuous_Duty_Brochure.pdf, [Online; accessed 06-August-2018].

[94] G. Torrisi, S. Grammatico, A. Cortinovis, M. Mercangoz, M. Morari, and R. S. Smith, "Model predictive approaches for active surge control in centrifugal compressors," *IEEE Transactions on Control Systems Technology*, vol. 25, no. 6, pp. 1947–1960, Nov 2017.

[95] C. Tournes and D. B. Landrum, "Development of a physically based axial compressor model," in *Proceedings of Thirtieth Southeastern Symposium on System Theory*, March 1998, pp. 120–124.

[96] J. van Helvoirt, B. de Jager, M. Steinbuch, and J. Smeulers, "Modeling and identification of centrifugal compressor dynamics with approximate realizations," in *Proceedings of 2005 IEEE Conference on Control Applications, 2005. CCA 2005.*, Aug 2005, pp. 1441–1447.

[97] J. van Helvoirt and B. de Jager, "Dynamic model including piping acoustics of a centrifugal compression system," *Journal of Sound and Vibration*, vol. 302, no. 1, pp. 361 – 378, 2007. [Online]. Available: http://www.sciencedirect.com/science/article/pii/S0022460X06008820

[98] A. Visioli, *Practical PID Control*, ser. Advances in Industrial Control. Springer London, 2006. [Online]. Available: https://books.google.ch/books?id=ymyAY01bEe0C

[99] A. Von Meier, *Electric Power Systems: A Conceptual Introduction*, ser. Wiley Survival Guides in Engineering and Science. Wiley, 2006. [Online]. Available: https://books.google.it/books?id=bWAi22IB3lkC

[100] T. Walther, G. Tweedale, G. Ray, R. P. R. Lucht, and J. A. Caton, "Fiber amplifier based sensors for combustion control," in *Technical Digest. Summaries of papers presented at the Conference on Lasers and Electro-Optics. Postconference Technical Digest (IEEE Cat. No.01CH37170)*, May 2001, pp. 290–296.

[101] F. Wang, Y. Huang, and T. Deng, "Simulation of turbulent combustion using various turbulent combustion models," in *2009 Asia-Pacific Power and Energy Engineering Conference*, March 2009, pp. 1–4.

[102] T. Ward, *Aerospace Propulsion Systems*. John Wiley & Sons, 2010. [Online]. Available: https://books.google.it/books?id=KEPgEgX2BEEC

[103] F. Willems and B. de Jager, "Modeling and control of compressor flow instabilities," *IEEE Control Systems*, vol. 19, no. 5, pp. 8–18, Oct 1999.

[104] L. Xiang, X. Chen, and G. Tang, "The torsional vibration of turbo-generator groups in mechanically and electrically coupled influences," in *2009 2nd International Congress on Image and Signal Processing*, Oct 2009, pp. 1–4.

[105] W. Xiaogang, B. Xueliang, and J. Bo, "Adaptive genetic algorithm for parameter identification of centrifugal compressor," in *2013 25th Chinese Control and Decision Conference (CCDC)*, May 2013, pp. 2982–2986.

[106] S. K. Yee, J. V. Milanović, and F. M. Hughes, "Validated models for gas turbines based on thermodynamic relationships," *IEEE Transactions on Power Systems*, vol. 26, no. 1, pp. 270–281, Feb 2011.

[107] I. Yousefi, M. Yari, and M. A. Shoorehdeli, "Modeling, identification and control of a heavy duty industrial gas turbine," in *2013 IEEE International Conference on Mechatronics and Automation*, Aug 2013, pp. 611–615.

[108] C. Zaiet, O. Akhrif, and L. Saydy, "Modeling and non linear control of a gas turbine," in *2006 IEEE International Symposium on Industrial Electronics*, vol. 4, July 2006, pp. 2688–2694.

[109] Z. Zhang, C. Li, and L. Wan, "Optimization and realization of a rotor dynamic balance measuring algorithm," in *2010 3rd International Congress on Image and Signal Processing*, vol. 9, Oct 2010, pp. 4109–4112.